Runaway Electrons in Disruptions and Perturbed Magnetic Topologies of Tokamak Plasmas

Inaugural-Dissertation

zur Erlangung des Doktorgrades
der Mathematisch-Naturwissenschaftlichen Fakultät
der Heinrich-Heine-Universität Düsseldorf

vorgelegt von

Michael Forster

aus Bernburg (Saale)

Düsseldorf, Juni 2012

aus dem Institut für Laser- und Plasmaphysik
der Heinrich-Heine-Universität Düsseldorf

Gedruckt mit der Genehmigung der
Mathematisch-Naturwissenschaftlichen Fakultät der
Heinrich-Heine-Universität Düsseldorf

Referent:	Prof. Dr. O. Willi
Koreferenten:	Prof. Dr. U. Samm
	Prof. Dr. T. Klinger

Tag der mündlichen Prüfung: 16.10. 2012

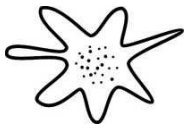

GRK 1203

iGRAD
Interdisciplinary
Graduate and Research Academy
Düsseldorf

Abstract

Nuclear fusion represents a valuable perspective for a safe and reliable energy supply from the middle of the 21st century on. Currently, the tokamak is the most advanced principle of confining a man-made fusion plasma. The operation of future, reactor sized tokamaks like ITER faces a crucial difficulty in the generation of runaway electrons. The runaway of electrons is a free fall acceleration into the relativistic regime which is known in various kinds of plasmas including astrophysical ones, thunderbolts and fusion plasmas. The tokamak disruption instability can include the conversion of a substantial part of the plasma current into a runaway electron current. When the high energetic runaways are lost, they can strike the plasma facing components at localised spots. Due to their high energies up to a few tens of MeV, the runaways carry the potential to reduce the lifetimes of wall components and even to destroy sensitive, i.e. actively cooled parts. The research for effective ways to suppress the generation of runaway electrons is hampered by the lack of a complete understanding of the physics of the runaways in disruptions. As it is practically impossible to use standard electron detectors in the challenging environment of a tokamak, the experimental knowledge about runaways is limited and it relies on rather indirect techniques of measurement.
The main diagnostics used for this PhD work are three reciprocating probes which measure the runaway electrons directly at the plasma edge of the tokamak TEXTOR. A calorimetric probe and a material probe which exploits the signature that a runaway beam impact leaves in the probe were developed in the course of the PhD work.
Novel observations of the burst-like runaway electron losses in tokamak disruptions are reported. The runaway bursts are temporally resolved and first-time measurements of the corresponding runaway energy spectra are presented. A characteristic shape and typical burst to burst variations of the spectra are found. The radial decay of the runaways is studied and approximated by an exponential distribution. Deriving from the measurements, resistive tearing modes or kink modes are suggested to trigger the formation of the bursts. Measurements of the total runaway electron energy are carried out using the calorimeter probe during induced TEXTOR disruptions. The dependencies of the runaway energy on the runaway current, the radial probe position, the toroidal magnetic field and the predisruptive plasma current are studied. The conversion efficiency of the magnetic plasma energy into runaway energy is estimated.
The losses of runaways due to resonant magnetic perturbation fields are measured applying a scintillator probe. The effects of well defined amplitudes of the perturbation on the temporal evolution of the runaway losses and the spectral properties of the runaways are analysed. The runaway transport towards the plasma edge is described by a model which takes magnetic turbulences and the magnetic perturbation field into account. Using an asymptotic theory, the orbits as well as radially and energy dependent transport coefficients for the runaways are calculated. A diffusion equation which utilises the coefficients is

solved delivering the density and the flux of the runaways. The model reproduces the measured enhancement of the runaway losses. Qualitatively different runaway spectra are found inside the plasma and at the edge. The spectra are explained by estimations of the competition between the secondary generation rate of the runaways and their radial diffusion. The runaway transport is found to be determined by the magnetic turbulence, the magnetic topology at the edge as well as inside the plasma and by the runaway energy. The mitigation of the runaways due to the magnetic perturbations can be understood by the enhancement of the losses of the low energy runaways. Eventually, a self consistent understanding of the temporal and spectral properties of the runaway transport due to the resonant magnetic perturbations is achieved.
As the spectra and the energy of the runaways determine the penetration depths, the possible wall damages and the lifetimes of wall components, the results presented in this thesis will have an impact on the design of the plasma facing components of future fusion devices. The insights obtained about the runaway bursts suggest new physics in postdisruptive tokamak plasmas. Moreover, the results will improve the understanding of the physics of the runaways in disruptions and hence help to develop effective runaway mitigation techniques. The runaway transport study presented enables an understanding of the effect of resonant magnetic perturbations which are being tested as a runaway mitigation scheme on many tokamaks.

Zusammenfassung

Die Kernfusion stellt eine wertvolle Perspektive für eine sichere und verlässliche Energieversorgung von der Mitte des 21. Jahrhunderts an dar. Derzeit ist das Tokamakprinzip die erfolgreichste und am weitesten entwickelte Option zum Einschluss eines von Menschenhand erzeugten Fusionsplasmas. Für den Betrieb zukünftiger Tokamaks von Reaktorgröße wie ITER es sein wird kann die Erzeugung von Runawayelektronen ein entscheidendes Problem darstellen. Der Runaway von Elektronen meint die zunehmend ungebremste Beschleunigung auf relativistische Geschwindigkeiten wie sie in den unterschiedlichsten Arten von Plasmen, darunter astrophysikalische Plasmen, Gewitterblitze und Fusionsplasmen, bekannt ist. Die Disruption von Tokamakentladungen kann zur Konversion eines erheblichen Teils des Plasmastroms in einen Runawayelektronenstrom führen. Verlassen die hochenergetischen Runaways den Plasmaeinschluss, treffen sie typischerweise auf Benetzungsflächen der Wandkomponenten, die nur einige $10\,\mathrm{cm}^2$ groß sind. Da sie Energien von einigen 10 MeV erreichen können, haben die Runaways das Potential die Lebensdauern von Wandkomponenten erheblich zu verringern und sogar aktiv gekühlte Teile zu zerstören. Die dringende Suche nach Optionen zur Unterdrückung oder Vermeidung der Runawayerzeugung wird dadurch erschwert, dass die Physik der Runaways in Disruptionen bis heute nicht vollständig verstanden ist. Da Standardetektoren für Elektronen wie sie in der Elementarteilchenphysik eingesetzt werden in der Hochtemperatur- und Hochmagnetfeldumgebung eines Tokamaks nicht einsetzbar sind, stützt sich die experimentelle Runawayforschung auf indirekte Messmethoden. Dies limitiert die messbaren Größen entsprechend.
Für die Messungen zu dieser Dissertation wurden drei verschiedene Typen von Sonden eingesetzt, um die Runaways am Plasmarand des Tokamaks TEXTOR direkt zu messen. Eine kalorimetrische Sonde und eine Materialsonde, die durch die Runaways verursachte Beschädigungen ausnutzt, wurden speziell im Rahmen des Doktorats entwickelt.
Neuartige Ergebnisse über die burst-artigen Runawayverluste in Tokamakdisruptionen werden vorgestellt. Es ist gelungen, die Runawaybursts zeitlich aufzulösen sowie zum ersten mal die zugehörigen Energiespektren der Runaways zu messen. Eine charakteristische Form der Spektren und typische Schwankungen von Burst zu Burst wurden gefunden. Der radiale Abfall des Runawaystrahls wird untersucht und als exponentiell beschrieben. Aus der Analyse der Messdaten ergeben sich zwei Kandidaten als Verursacher der Runawayburstbildung: resistive Tearingmoden und Kinkinstabilitäten. Mit Hilfe der Kalorimetersonde wurde die Gesamtenergie der Runaways in TEXTOR-Disruptionen gemessen. Die Abhängigkeiten der Gesamtenergie vom Runawaystrom, der radialen Sondenposition, dem toroidalen Magnetfeld und dem Plasmastrom vor der Disruption werden untersucht.
Eine Szintillationsdetektorsonde wurde benutzt, um die Runawayverluste unter dem Einfluss von resonanten, magnetischen Störfeldern zu messen. Die Auswirkungen wohldefinierter Amplituden der Störungen auf die zeitliche Entwicklung

der Runawayverluste werden analysiert. Der radiale Runawaytransport zum Plasmarand wird unter Einbeziehung der magntischen Turbulenzen sowie der magnetischen Störfelder modelliert. Mit Hilfe einer asymptotischen Theorie werden die Trajektorien der Runaways sowie deren radius- und energieabhängige Transportkoeffizienten berechnet. Die Koeffizienten werden in einer Diffusionsgleichung verwendet, deren Lösung zu der Dichte und dem Fluss der Runaways führt. Mit dem Modell gelingt es, die gemessene Erhöhung der Runawayverluste durch die Störfelder zu reproduzieren. Die qualitativ unterschiedlichen Runawayspektren im Plasmainneren und am Rand werden durch das Zusammenspiel des sekundären Runawayerzeugungskanals sowie der radialen Diffusion erklärt. Die Unterdrückung der Runaways durch die Anwendung der magnetischen Störfelder kann durch die Erhöhung der Verluste der niederenergetischen Runaways verstanden werden. Der Runawaytransport ist im Wesentlichen durch die magnetische Turbulenz, die Magnetfeldtopologie am Rand sowie im Plasmainneren und durch die Energie der Runaways bestimmt. Ein selbstkonsistentes Bild der zeitlichen sowie der spektralen Eigenschaften des Runawaytransports durch resonante, magnetische Störfelder wird erreicht.
Da die Spektren und die Gesamtenergie der Runawayelektronen ihre Eindringtiefe, die möglichen Schäden an Wandkomponenten und deren Lebensdauern festlegen, werden die Ergebnisse in dieser Dissertation einen Einfluss auf das Design zukünftiger Fusionsmaschinen haben. Die dargestellten Erkenntnisse legen neue physikalische Prozesse im postdisruptiven Tokamakplasma nahe. Darüberhinaus werden die Ergebnisse das Verständnis der Runawayphysik in Disruptionen verbessern und somit die Entwicklung effektiver Runawayunterdrückungsmechanismen fördern. Die Studie über den Runawaytransport ermöglicht bereits ein besseres Verständnis der Wirkungsweise resonanter, magnetischer Störfelder, die derzeit an vielen Tokamaks zur Runawayunterdrückung erforscht werden.

Contents

1 Introduction

Intensely reading this thesis will cost your body about 4 W of power at maximum during the most sophisticated paragraphs. Using a reading lamp will take about 40 W of electric power and reading the thesis on a laptop will take about 75 W additionally. Nevertheless, reading this thesis is a good idea as virtually everything man does consumes energy. This energy consumption is increasing with the degree of the technical development of the human societies and with the world's population which is rapidly growing. In a report by the United Nations [1] three scenarios for the growth of the world's population are discussed. The medium and most realistic scenario assumes an increase from 6.1 billion in the year 2000 to a population maximum of 9.2 billion inhabitants until the year 2075. In analogy, three different scenarios for the primary energy consumption[1] are analysed in [2]. According to the medium scenario, the installation of additional 10 to 15 TW of supplied power is needed within the next 50 years. This equals an increase of 200 to 300 GW per year which means roughly 1 GW more than every second day. The fraction of electricity among the consumed energy is permanently increasing. Today about 22 % of the energy consumed are electric energy and this value will increase by 1 to 1.4 % per year in the near future [3]. At the same time the fossil fuels, which deliver the main part of our energy, are getting rarer by the time. Due to the collisions of many political and economical interests, it is hard to give a certain date for the fossils running out. An example for this uncertainty presents the discussion about the availibility of oil [4, 5]. When burning oil to gain energy, one has to keep in mind that oil is a basic chemical for many industries, e.g. the pharmaceutical industry. Another argument against burning fossil fuels is that it causes the main part of the antropogenic CO_2 emission. Since the beginning of the age of the industrialisation an increase of the atmospheric CO_2 level has been recorded [6]. It is believed that this can have a worrisome impact on the highly nonlinear global ecosystem leading to arguable but probably irreversible longterm consequences for the global temperature and climate.
A second main source of electric energy, nuclear fission, is currently a subject to a lively debate. The drawbacks of nuclear fission are the production of sizable amounts of longlived nuclear waste, operational safety with large radioactive reactor inventories and proliferation. Moreover, using the current types of reactors, the resources of fission will last on a scale comparable to the one of fossils. Breeder concepts could be used much longer but with the addition of further safety and environmental issues. Dealing with the difficulties of fission, one always has to take into account unavoidable political and social complications in finding and applying the optimal solutions regarding safety and waste storage. Ultimately, the common awareness of environmental and technical risk questions is growing.
In consequence, the two main sources of electric energy, fossil fuels and nuclear

[1] Primary energy is the energy in its first form before any conversion. The given numbers include all channels of consumption like electricity, heating and transport etc.

fission, are in doubt and the way of producing electric energy has to be rebuild. The requirements new sources of energy have to match are profitability, security of supply, operational safety, climatic neutrality, abundance of resources and environmentally compatible operation. Renewable energy sources fullfill a wide range of these requirements and have great potentials. In general, their disadvantages are low energy densities, temporal fluctuations of the supply and the need for storage which affects for example the costs. In the next paragraph the most important alternative schemes of generating electricity should be mentioned briefly, mainly following [3], to give an overview of the options available.

Although it is a CO_2 neutral method, the use of biomass as a source of energy is seen more and more critical because the growing of energy crop plants is competing with the production of food for areas of cultivation. The generation of electricity from solar power has the big disadvantage of being dependent on the intensity of the sunshine. This principally limits the availability in northern countries like Germany and it causes large fluctuations due to the weather, the change of the seasons and the alternation of day and night. These limitations also affect the contestability. The concentrated use of solar thermal energy in southern regions of the world comes with the drawback of political dependencies and the problem of the longrange transport of the electricity. The issue of temporal fluctuations is an even bigger one for wind energy. Nevertheless, it is an attractive alternative for regions of low sunshine duration and so in Germany wind energy is the most developed renewable source of energy. The power credit[2] of the existing and planned wind energy power plants in Germany is about 10 % in 2010 and it will decrease to about 3 % until 2030. This makes an additional source of electricity which provides a base load supply mandatory. The generation of hydro-electric power is practically at the maximum in Germany. Worldwide, there is a potential to increase but tapping it often implies substantial intrusions into natural landscapes. The use of geothermal energy is still in an experimental stage and the consequences it brings are not quite clear. In Germany drilling holes of 3000 m and often more than 5000 m in depth is necessary to be able to utilise geothermal energy.
Regarding to conceptual power plant studies [7, 8], nuclear fusion is predicted to be a safe and rather clean source of electricity with a low consumption of abundant resources. The aim of a fusion power plant is it to use the fusion of light atomic nuclei to gain energy for the generation of electricity. The process of fusion in general is just the same as it takes place in the sun which is practically the primary source of all renewable sources of energy, except geothermy. The burning fuel of a nuclear fusion power plant is a plasma [9] which is an ionised gas at temperatures of about a hundred million° C. The gases considered for nuclear fusion in the first place are the two heavy isotopes of hydrogen, deuterium and tritium. Fusing those nuclei results in the production of helium. As tritium is not abundant, it has to be bred inherently in the reactor blanket

[2] The power credit is the value of conventional power which can be substituted by wind energy without loosing the security of supply.

which makes deuterium and lithium the fundamental resources of fusion.
Deuterium is abundant in sea water by 33 g per t. The deuterium content in the oceans is about $4 \cdot 10^{13}$ t. This equals $5 \cdot 10^{11}$ TW $\cdot$ years of energy [10]. The exact numbers for lithium are under discussion, but roughly tens of million t are abundant in ores and brines and hundreds of billion t are dissolved in sea water (0.1 to 0.2 ppm) [10–12]. A fusion reactor is continuously fueled and thus no large amounts of the fuel are stored in the reactor. The limited amount of the fuel which is available at each instant of time guarantees an inherent safety and excludes an uncontrolled burn or even neutron multiplication cascades. According to the conceptual study [7], even a complete loss of the active cooling would not lead to the melting of reactor structures due to the low residual heating. Neither deuterium, lithium nor helium are radioactive. Moreover, the product, helium, is chemically inert and very useful in industry. The reason for tritium not being abundant is its radioactivity with a low half life time of about 12 years. Although the fusion reaction does not directly produce any radioactive waste, the tritium and the produced neutrons activate the structures and so some contaminated material is produced. The induced radioactivity is ten times less than in fission and it decays on the level of decades rather than centuries. Probably, the most important safety issue is the chemical equivalence of tritium and hydrogen. This means tritium can replace hydrogen in water or organic compounds which leads to the potential of hazards. The biological half life of tritium in the body is about 10 days. Following the studies, a major accident in a fusion reactor would release about 200 g of the few kg stored in a power plant. Nuclear fusion power plants are predicted to be able to guarantee the security of supply. They do not produce any CO_2, come without major technical risks like fission plants do as a failure will inherently end the burning process, no permanent repository for large amounts of longlived radioactive waste is needed, no radioactive raw materials are needed and the environmental balance is convenient. Furthermore, the studies [7, 8] conclude that the costs of electricity from fusion power plants will be comparable to other sources.

Nuclear fusion seems to be the ideal safe, secure and clean source of energy, but still a lot of research and developement are needed to be able to use nuclear fusion practically from the middle of the 21st century on. The most developed branch of fusion research is the magnetically confined fusion using the tokamak principle. The latter is characterised by a large current being driven in the toroidal fusion plasma. The heating and the confinement of the fusion plasma are already understood quite well. In 1991 a breakthrough was reached at the european experimental fusion experiment JET. For the first time energy was generated by fusion in a controlled way. For a duration of 1 s a fusion power of 1 to 2 MW was obtained [13]. The maximum power values achieved until today are 16 MW for 1 s and 4 to 5 MW for about 4 s at JET [14].
A new era of fusion research has been entered when the agreement on the construction of the international experimental reactor ITER [15] was signed in 2005. The construction started in 2009 in Cadarache, France. ITER will be the first

fusion experiment on a reactor size scale. It is a tokamak designed for studies of reactor-relevant modes of operation and necessary fusion-specific technologies. One goal of the ITER project is a fusion energy yield of $Q \geq 10$. This means, at least ten times more energy is produced by fusion reactions than is spent e.g. to heat the plasma. Besides some others, one big challenge for the operation of ITER are disruptions [16, 17]. These events of instability cause the sudden loss of the confinement of the fusion plasma due the interruption of the plasma current as the operational parameters leave the stable regions. One main aspect of disruptions is the acceleration of plasma electrons into the relativistic regime which is enabled by the occurrence of high electric fields. The relativistic electrons are called runaway electrons (REs) [18]. When the highly energetic REs are expelled from the plasma, they can strike the plasma facing components (PFCs) at localised spots. Due to their high energy up to a few tens of MeV, the REs can easily traverse several cm of low atomic number material and even melt high atomic number material on the surface [19]. Consequently, REs carry the potential to reduce the lifetimes of tokamak wall components and even to destroy sensitive, i.e. actively cooled parts [20]. For ITER an inherent susceptibility for an efficient conversion of the plasma current into a RE current of up to 70 % is expected. A RE content of 50 MJ in ITER disruptions as well as resulting peak energy depositions enough to melt or ablate the ITER wall materials are predicted [21]. Consequently, the understanding of the physics of REs and finding effective ways to avoid, suppress or mitigate the generation of REs or the harmful consequences of their loss are issues of great importance for the operation of ITER and machines beyond.

RE studies have a long tradition which started in the very beginning of the research of toroidal plasmas. But due to the limitations that the challenging environment of a tokamak puts on the possibilities to diagnose REs, their physics are still not fully understood. The ansatz of developing specialised probes to study the REs by measuring so far unaccessible properties is followed at the Institut für Laser- und Plasmaphysik of the Heinrich-Heine-Universität Düsseldorf. The measurements presented in this thesis were carried out at the tokamak TEXTOR of the Forschungszentrum Jülich GmbH. In this machine REs can be produced very reliably during stationary, ohmic discharges and during disruptions which are routinely induced for such experiments. The new RE probes allow to study many open questions about the physcis of REs. These questions are addressed in this thesis. During the current quench phase of disruptions REs are expelled from the plasma in form of very short events called bursts [22]. The loss mechansim which leads to the formation of those bursts is not understood yet. Moreover, the temporal evolution of the bursts as well as the corresponding energy spectra of the REs are not known. A further open question concerns the total RE energy in disruptions which surprisingly, despite many predictions, has never been measured in present day machines. From this the efficiency of the conversion of the predisruptive, magnetic plasma energy into RE energy could be derived. For the estimation of the size of the strike area of the REs on the

wall elements the question of a RE decay length behind a limiter or a limiting PFC is of interest. In order to find answers to all of these questions, disruption measurements are carried out at the medium sized tokamak TEXTOR.
Three different types of probes are used as the main RE diagnostics. A scintillator probe enables the detection of the REs directly at the plasma edge with a temporal as well as a spectral resolution. A probe which is designed for calorimetric measurements of the RE energy is developed in the course of the PhD work presented. A third probe, also developed for the PhD work, is a material probe designed for single shot RE heat load experiments which deliver information about the energy spectrum and the radial distribution of the REs at the plasma edge. Concluding from the experiments with this probe, the RE spectrum in a TEXTOR disruption is found to be approximately exponential with an also exponential radial decay of the RE beam. The decay length is found to be of the order of the Larmor radius of the REs. These results are refined using measurements of the scintillator probe. Furthermore, the RE bursts are detected directly at the plasma edge. Their temporal properties and the energy spectra of the REs forming the bursts are measured for the first time. Deriving from this, possible loss mechansims are proposed. The first measurements of the total RE energy in tokamak disruptions are carried out using the calorimeter probe. From the results the efficiency of the conversion of the magnetic energy into RE energy is estimated in agreement with predictions in the literature and consistent with estimations concluded from the scintillator probe experiments. In view of the mitigation of REs the influence of resonant magnetic perturbations on the RE transport is studied. Due to their excellent reproducability, these measurements are carried out in TEXTOR low density discharges. During the stationary phase of these discharges REs with energies up to 30 MeV are reliably produced. Magnetic perturbation fields of a well defined amplitudes are applied by means of the Dynamic Ergodic Divertor (DED) of TEXTOR to enhance the RE losses by an ergodisation of the magnetic topology. The REs, which are expelled from the plasma, are detected by the scintillator probe temporally and spectrally resolved. The experimental results are used to develop a model which takes the magnetic turbulence and the external perturbation into account to describe the temporal and spectral features of the radial RE transport by a diffusion process.

The main body of this thesis starts with chapter 2 which has an introductory character as it gives an overview of the basics of nuclear fusion with a focus on the physics of tokamaks. The fusion reaction foreseen for fusion power plants is described and the tokamak principle is introduced before the basic physics of tokamak disruptions are outlined. In chapter 3 the REs are added to the picture. The mechanisms of the generation of REs, some important properties of the REs, common RE diagnostics and currently studied RE mitigation schemes are briefly reviewed to build a background for the work presented later. The main scientific instruments used for the studies reported in this thesis are described in chapter 4. The most important features of the tokamak TEXTOR, the DED, the disrup-

tion mitigation valve (DMV) and also of the GEANT4 simulation code are given before the RE diagnostics, especially the probes, are presented in detail. The scintillator probe presented in section 4.6 was developed by T. Kudyakov and used by the author for several measurements of this thesis. The RE heat load probe (section 4.7) and the RE calorimeter probe (section 4.8) were designed and developed by the author. The novel results which include the answers to the open questions about REs in disruptions mentioned above are discussed in chapter 5. The corresponding probe measurements are described. The RE heat load probe measurements and the evaluation of the data given in section 5.1 were carried out by the author. All the GEANT4 simulations are the work of the author as well. The metallographical preparation and the microscopic examination of the probe material were carried out by J. Linke, C. Thomser and their co-workers at the Institut für Energie- und Klimaforschung, Werkstoffstrukturen und -eigenschaften (IEK-2) of the Forschunsgzentrum Jülich GmbH. The thermogravimetrical measurements were performed by the author at the Institut für organische und makromolekulare Chemie of the Heinrich-Heine-Universität Düsseldorf. The scintillator probe measurements in section 5.2 and their evaluation are the work of the author. The use of the magnetic data obtained by applying Mirnov coils was supported by L. Zeng. The content of section 5.3 including the measurements, the evaluation and all the GEANT4 simulations are the author's work. In chapter 6 the results about the RE transport due to the magnetic turbulence and resonant magnetic perturbations are presented. The author carried out the measurements using the scintillator probe and evaluated the data. Using the experimental results, S.S. Abdullaev developed an asymptotic theory of RE diffusion. The author calculated the corresponding diffusion coefficients and developed the RE transport model. The corresponding diffusion equation was solved by G. Sewell applying his PDE2D code. The concluding analysis of the experimental and theoretical data was conducted by the author. At the end of the thesis a comprehensive summary and a list of the publications that originated from the PhD work are given. The appendices A, B and C provide supplementary data of the RE bursts, additional photographs of the calorimeter probe and a list of the abbreviations used throughout the thesis, respectively.

2 Basics of Thermonuclear Fusion

The greatest motivation for studies in the field of nuclear fusion is utilising fusion reactions to yield energy from a reactor. This chapter deals with the aspects of thermonuclear fusion, i.e. the fusion reactions, the involved species and the requirements for a positive energy balance. A more detailed discussion can be found in [23]. The up to date most successful way of producing and confining a fusion plasma uses the tokamak principle. As all the experiments presented in this thesis were carried out at the tokamak TEXTOR, the principle is introduced and some important properties of its magnetic field are treated. The chapter does not claim to discuss the tokamak physics in detail, rather it is intended to review the basics which are essential for the further reading. A comprehensive compendium about the tokamak is [10]. The basic plasma physics, e.g. derivations of the particle drifts, can be found in [9, 24]. Deriving from the magnetic field configuration of the tokamak, the transport is briefly discussed [25]. Finally, the most dramatic instability of tokamak plasmas - the disruption, which can also include the generation of runaway electrons, is introduced. The physical picture of disruptions is not fully understood, but descriptions based on experimental observations can be found in [10, 21, 23, 26]

2.1 Thermonuclear Fusion

The atomic nucleus denoted by X_Z^A consists of Z protons and $A-Z$ neutrons. The difference between the sum of the masses of the individual nucleons, m_p and m_n, and the mass of the atomic nucleus is called the mass defect.

$$[Zm_p + (A-Z)m_n] - m(X_Z^A) = \Delta m \tag{2.1.1}$$

Interpreting this mass difference, the nucleus is in a negative state of energy. In order to disassemble the nucleus, the energy $E = \Delta mc^2$ has to be supplied externally. This binding energy is different for every nucleus as it depends on the mass number A. The function E/A over A has a maximum for the nucleus of iron which in consequence leads to two different ways to gain energy by setting free the binding energy via nuclear reactions. The first way is to use the fission of nuclei heavier than iron and the second one is the fusion of nuclei lighter than iron. While the first way is utilised in fission reactors, the second way presents the source of the star's energy. Due to the maximum of E/A over A, only fusion reactions resulting in the production of nuclei lighter than iron and iron itself take place by themselves and so the heavier elements are not produced in the stars. According to the slope of E/A over A, the yield from the fusion of two light nuclei is much larger than from the fission of one heavy nucleus.
Due to the repulsive Coulomb force between two positively charged nuclei, the fusion reaction cannot take place spontaneously under terrestrial conditions. Only at very short distances the attractive strong force can overcome the electromagnetic force. In order to come close enough to each other, the nuclei must have enough energy to be able to tunnel through the Coulomb barrier. If an

ensemble of particles contains such a high energy, this is equivalent to a temperature of about a hundred million° C. This equals 10 keV via $E = 3/2 k_B T$. At such temperatures a gas is ionised into a plasma consisting of ions, electrons and neutrals. Regarding to the high temperatures which enable the fusion process, one speaks about thermonuclear fusion.
The fusion reaction easiest to achieve is the one between the two heavy isotopes of hydrogen:

$$D_1^2 + T_1^3 \rightarrow He_2^4 + n_0^1.$$

The fusion of deuterium and tritium has the highest cross section at the lowest temperatures. The fusion products per reaction are a nucleus of helium, which carries 3.5 MeV, and a neutron which carries 14.1 MeV. It is the kinetic energy of the neutron which can be used to generate electricity in a power plant by means of conventional technology involving steam and turbines. The kinetic energy of the helium nucleus can be used as a contribution to the heating of the plasma via collisions. The energy yield of the reaction stems from the binding energy due to a mass defect of $\Delta m = 0.01875 \cdot m_p$.
As already mentioned in the introduction, deuterium is abundant, but tritium is radioactive and due to its half life time of $\tau_{1/2} = 12.3$ years it is not naturally abundant. Thus, the tritium has to be bred from lithium. This can be done inherently in the blanket of a fusion reactor using a fraction of the neutrons which result from the fusion reactions.

$$Li_3^6 + n_0^1 \rightarrow T_1^3 + He_2^4$$

$$Li_3^7 + n_0^1 \rightarrow T_1^3 + He_2^4 + n_0^1$$

The natural abundances of the lithium isotopes are 7.4 % of Li_3^6 and 92.6 % of Li_3^7. While the upper reaction has an energy yield of 4.8 MeV, the lower one needs an external supply of 2.5 MeV. This subtracts only a small amount of the yield from the overall fusion process.
A crucial issue regarding the usefulness of fusion is the ratio of the energy gained from the reactions to the energy spent for the heating of the plasma, the confinement and the losses from the plasma. This paramter is called Q. Break even, which means $Q = 1$ and a net energy yield, has already been reached at JET. If the fusion reactions take place without any further external input of energy, this implies $Q \rightarrow \infty$. In analogy to a burning flame this condition is called ignition. In this case the energy necessary to compensate the losses is provided solely by the helium nuclei produced in the fusion reactions. This is known as α-particle heating. For safety reasons the operation below the ignition threshold is practically more convenient. For ITER $Q = 10$ is set as a main goal. The Q-thresholds of fusion performance can be expressed as physical parameters by means of the fusion product $n\tau_E T$. n is the ion density, T the ion temperature and τ_E the energy confinement time which can be defined by

$$P_{loss} = \frac{W}{\tau_E}. \tag{2.1.2}$$

Here P_{loss} is the power of all the losses from the plasma and W is the energy stored in the plasma. Thus, τ_E is a measure of the quality of the confinement. For $n\tau_E T = 0.5 \cdot 10^{21}\,\mathrm{m^{-3}s \cdot keV}$ break even is reached. Ignition means $n\tau_E T = 3 \cdot 10^{21}\,\mathrm{m^{-3}s \cdot keV}$ which can be realised with $T = 10\,\mathrm{keV}$, $n = 10^{20}\,\mathrm{m^{-3}}$ and $\tau_E = 3\,\mathrm{s}$ [10]. The amounts of energy released by fusion are enormous and if they are used effectively, about 2 L of water (containing deuterium) and 250 g of stones (containing lithium) provide the energy that a German family, consisting of four people, consumes during a year [27].

2.2 The Tokamak

The fusion plasma of the sun has a huge mass and so it is kept from expanding into space by its own gravitation. Of course, the plasma in a fusion reactor on earth cannot be that big and thus another way of confining the hot plasma has to be applied. It is not possible to contain the plasma simply by putting walls around it. The hot and thin plasma would be cooled down and destroyed immediatly by the contact to the cold wall. The current research on plasma confinement follows two branches: inertial confinement and magnetic confinement. Only the latter branch, which is characterised by strong magnetic fields keeping the plasma away from the wall of the vacuum chamber, should be of interest here. In the way of supplying the magnetic field the two most important types of magnetic confinement machines differ. The stellerator utilises a magnetic field which is completely generated by specially shaped coils. The magnetic field of a tokamak [28] is a superposition of fields generated by currents in coils and by a current driven in the plasma itself. This setup has the advantage of a rather simple coil geometry at the expense of physical complexity regarding stability. The tokamak principle is the most successful magnetic confinement scheme up to date. The next step fusion device ITER as well as TEXTOR are tokamaks. Thus, the basics of the tokamak are introduced in the following.

The simplest geometry of a magnetic field in a plasma consists of straight field

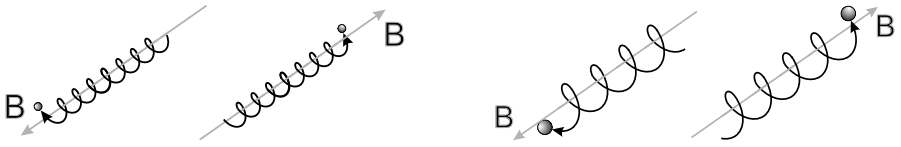

(a) Electrons (b) Ions

Figure 2.2.1: Schemes of the cyclotron gyration of charged particles around the lines of a straight magnetic field B with the electrons gyrating in the opposite direction than the ions

lines. This field forces the charged plasma particles into a gyromotion around the field lines as depicted in figure 2.2.1. The direction of the gyration depends on the charge of the particle and the direction of the magnetic field as shown for electrons in figure 2.2.1(a) and for ions in figure 2.2.1(b). The frequency of

the gyration is the cyclotron frequency

$$\omega_c = \frac{|q|B}{m} \tag{2.2.1}$$

where q is the electric charge and m the mass of the particle. B is the magnetic field strength. The radius of the gyro orbit is the Larmor radius

$$r_L = \frac{v_\perp}{\omega_c} = \frac{mv_\perp}{|q|B} \tag{2.2.2}$$

in which $v_\perp$ is the velocity of the particle perpendicular to the magnetic field. Thus, the electrons and ions are confined in the plane perpedicular to the magnetic field. The motion parallel to the magnetic field is unrestricted and so the particles are quickly lost along the field lines which in practice have to intersect a wall. Consequently, only closing the field lines upon themselves can lead to a good magnetic confinement. Following the Poincaré-Hopf theorem [29], the torus is the simplest closed magnetic geometry without singularities which can be formed by the field. Figure 2.2.2 illustrates the geometry including the major radius R, the minor radius r and the directions around the large circumference of the torus, called toroidal, and around the small circumference called poloidal. A purely toroidal geometry of the magnetic field is still too simple to provide

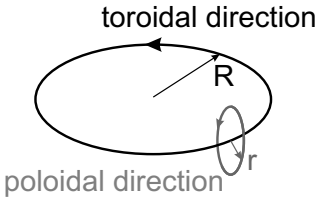

Figure 2.2.2: Visualisation of the terms in a toroidal geometry

a good confinement. The toroidal magnetic field has a curvature and it is not uniform along the major radius, rather $B \propto 1/R$. Thus, the magnetic field has a gradient perpendicular to its own direction. These nonuniformities lead to drifts of the particles' guiding centres as indicated in figure 2.2.3. The curvature drift has the velocity

$$v_R = \frac{mv_\parallel^2}{qB^2} R_c \times BR_c^2 \tag{2.2.3}$$

with the radius of the curvature R_c and the particle's velocity parallel to the magnetic field $v_\parallel$. The ∇B drift has the velocity

$$V_{\nabla B} = \pm\frac{1}{2} v_\perp r_L \frac{B \times \nabla B}{B^2}. \tag{2.2.4}$$

Both drifts have the same dependecy of the drift direction on the charge of the particles. This leads to a vertical charge separation in the plasma to the top

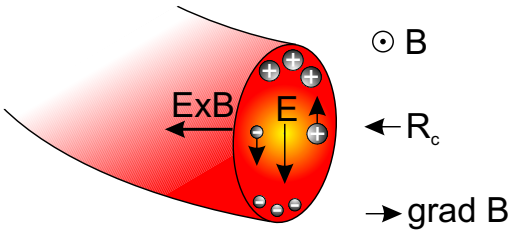

Figure 2.2.3: Scheme of the plasma particle drifts, the charge separation and the resulting outward force in a purely toroidal magnetic field

and the bottom of the torus as shown in figure 2.2.3. The charge separation establishes a vertical and hence perpendicular electric field which causes an additional drift motion with

$$v_E = \frac{E \times B}{B^2}. \tag{2.2.5}$$

As this drift is independent of the charge, the whole plasma is driven to the outer wall. This practically immediately terminates a plasma in a purely toroidal magnetic field. The problem can be overcome by superimposing a poloidal magnetic field B_p to the toroidal one B_t by driving a current through the plasma column. The resulting field is helically wound. It short-circuits the charge separation and prevents the formation of a vertical electric field. Both, the tokamak and the stellerator, work with a helical magnetic field although in the stellerator it is generated by coils only. The tokamak principle is illustrated by figure 2.2.4. The name tokamak is a russian abbreveation of *toroidalnaya kamera i magnitnaya katuschka* which means toroidal chamber with a magnetic coil. The toroidal vacuum chamber 1 is poloidally encircled by the toroidal magnetic field coils of which only one is indicated in the figure and labelled as 2. The poloidal magnetic field is produced by a transformer action. A temporally varying voltage in the primary coil 3 of the transformer induces a voltage around the plasma loop 5 which acts as the secondary transformer coil. The iron yoke 4, which improves the effectivity of the transformer, is optional. The loop voltage drives the plasma current I_p which produces the poloidal magnetic field. The superposition with the toroidal field gives the helical field which is needed to confine the plasma. Due to the transformer action, the tokamak is a pulsed device. The pulses are referred to as discharges or shots. Only using noninductive current drive schemes can allow a steady state operation of the machine in the future. The injection of neutral particles and the use of plasma waves at the electron or ion cyclotron frequency or at the lower hybrid frequency are being studied. The plasma current is also used to heat the plasma ohmically. As the resistivity of the plasma decreases with increasing temperature, $\eta \propto T_e^{-3/2}$, the effectivity of the ohmic heating decreases, too. Thus, the temperatures needed for fusion cannot be achieved by ohmic heating alone and auxiliary heating schemes are needed. Waves resonant to the gyromotion of the ions or the electrons and

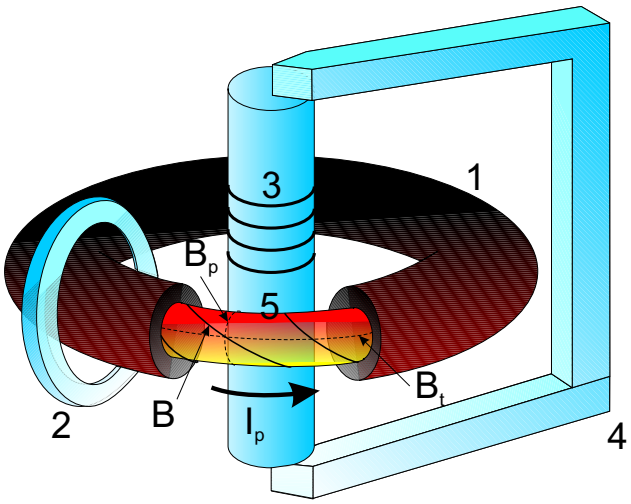

Figure 2.2.4: Schematic view of a tokamak including the most important components: 1 - the vacuum vessel, 2 - one of the toroidal field coils, 3 - the primary coil of the transformer, 4 - the iron yoke, 5 - the plasma column, I_p - the plasma current, B - the magnetic field consisting of B_t - the toroidal magnetic field and B_p - the poloidal magnetic field

neutral particle beams can be launched into the plasma to heat it. In a fusion reactor the helium which is produced is foreseen to contribute to the heating. This α-particle heating was mentioned before. For this thesis no auxiliary heating schemes were used at TEXTOR. To enable some means of plasma position control another set of coils going toroidally around in the upper and lower midplane is commonly used to generate a relatively small vertical magnetic field.

The magnetic topology of a tokamak plasma is a result of the use of all the

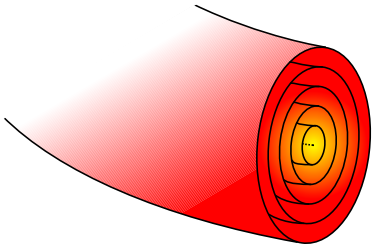

Figure 2.2.5: Scheme of the ideal magnetic topology of a tokamak consisting of nested toroidal surfaces and the magnetic axis in the centre

different coils and of the plasma current. It can be calculated by means of ideal

magnetohydrodynamics (MHD). This theory describes the plasma as an ideally conductig fluid which excludes displacement currents in the Maxwell equations ($j = \nabla \times B$). In order to confine the plasma, the pressure has to be balanced by the magnetic field implying

$$\nabla p = j \times B. \tag{2.2.6}$$

The according tokamak equilibrium is calculated as the solution of the Grad-Shafranov equation. The magnetic topology consists of nested toroidal surfaces on which the magnetic field lines lie and which enclose the magnetic axis at $r = 0$. These nested tori, shown in figure 2.2.5, are called magnetic flux surfaces which is justified by the toroidal magnetic flux being constant on these surfaces. As also the lines of the current density lie on these surfaces, it follows from

$$B \cdot \nabla p = 0 \tag{2.2.7}$$

and

$$j \cdot \nabla p = 0 \tag{2.2.8}$$

that the pressure p and hence the temperature T times the density n are constant on these surfaces. Due to the toroidal geometry, the magnetic surfaces are displaced outwards from the magnetic axis along the major radius by the Shafranov shift. Thus, the flux surfaces are nonconcentric. In the ideal equilibrium case the magnetic field lines lie on the magnetic surfaces and due to their helical winding, they can either close upon themselves after a finite number of toroidal turns or they fill up the whole surface.

As the helical winding of the field lines is characteristic for each magnetic surface, a paramter q can be assigned to the flux surfaces, respectively. The safety factor q is the number of the toroidal turns a field line exerts per poloidal turn.

$$q = \frac{1}{2\pi} \int_0^{2\pi} \frac{d\Phi}{d\Theta} d\Theta = \frac{1}{2\pi} \oint \frac{B_t}{R} \frac{d\ell}{B_p} \tag{2.2.9}$$

The field lines which close upon themselves after a finite number of turns correspond to values of $q = m/n$ with $m, n \in \mathbb{N}$ and thus lie on rational surfaces. Typically, q is a function of the minor radius with a minimum at the magnetic axis and a maximum at the plasma boundary at $r = a$. Configurations differing from this are regarded to as reversed shear. The function $q(r)$ cannot be tailored arbitrarily as several limits on q are imposed by plasma instabilities. Typical restrictions are $q > 1$ at the magnetic axis and $q > 2$ at the edge. The role of q in the MHD stability theory is the reason for the name safety factor.

2.3 Transport in Tokamaks

The ideal magnetic topology of a tokamak consists of nonconcentric, nested toroidal surfaces as introduced above. The helical magnetic field lines are bound to these surfaces. The transport of heat and particles along the field lines, called parallel transport, is very fast but it keeps the particles inside the plasma. No

losses are caused by the parallel transport in an ideal tokamak topology and thus only the transport across the magnetic surfaces accounts for losses. The cross field transport due to collisions in a straight cylindrical plasma geometry is described by the classical theory. Collisions are assumed to cause the particles to exert random walks. Hence, the transport can be quantified by a diffusion coefficient.

$$D = \frac{\langle (\Delta r)^2 \rangle}{\tau} \tag{2.3.1}$$

Here Δr is the typical radial step size that the particles jump due to a collision and $\tau = 1/\nu$ is the collision time of a particle while ν denotes the collision frequency. Due to the subject of this thesis, the emphasis of the following considerations is put on the plasma electrons. Using the electron Larmor radius $r_{L,e}$ as Δr, leads to the classical difffusion coefficient D_{class}. The mean free path of the particles depends on the collision frequency and the thermal velocity v_T.

$$\lambda = v_T/\nu \tag{2.3.2}$$

In the toroidal geometry of a tokamak the helical flow of the charged particles is used to prevent a charge separation caused by the particle drifts. The path of a particle helically around a magnetic surface is approximately $L \propto qR$ long. The parallel particle flow is hampered by collisions and thus the helical orbits are disturbed. The result are small electric fields which interact with the magnetic field to cause further drifts and an enhancement of the transport perpendicular to the magnetic field. These effects of the toroidal geometry are taken into account by the neoclassical transport theory.
The inverse aspect ratio of a tokamak is defined by $\epsilon = r/R$. In the following the limit of a large aspect ratio $\epsilon << 1$ is considered. The condition

$$\frac{\nu q R}{v_T} >> 1 \tag{2.3.3}$$

implies $\lambda < L$ and thus a mean free path of the particles which is small compared to the helical particle orbit length. The regime of high collisionality, in which the typical particles cannot complete their helical flow around the magnetic surfaces without being disturbed by collisions, is defined. It is also called the Pfirsch-Schlüter regime. The corresponding neoclassical diffusion coefficient is larger than the classical one:

$$D = D_{class} \left(1 + 2 \frac{\eta_{||}}{\eta_\perp} q^2 \right). \tag{2.3.4}$$

$\eta_{||}$ and $\eta_\perp$ denote the resistivity of the plasma parallel and perpedicular to the magnetic field, respectively.
The opposite limit

$$\frac{\nu q R}{v_T} >> 1 \tag{2.3.5}$$

characterises the regime of low collisionality for which $\lambda > L$. The typical particles can complete their orbits around the magnetic surfaces which brings

another toroidal effect to importance. As $B \propto 1/R$, the inner side of the torus is the high field side (HFS) and the outer side is the low field (LFS). Particles flowing helically between the HFS and the LFS can be trapped in this magnetic mirror. The orbit of such a trapped particle is visualised schematically in figure 2.3.1. The trapped particles bounce back and force between the HFS and the

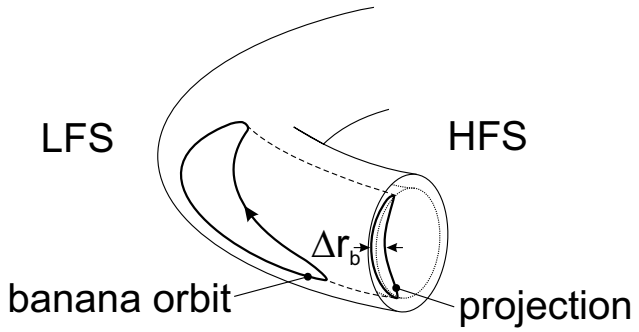

Figure 2.3.1: Scheme of the banana orbit of a plasma particle being trapped between the magnetic low field side (LFS) and the high field side (HFS); the width of the orbit Δr_b is indicated in its poloidal projection

LFS with the frequency

$$\omega_b \propto \frac{\sqrt{\epsilon} v_T}{qR}. \tag{2.3.6}$$

According to the shape of the poloidal projection of the orbits, these are called banana orbits and the regime is called the banana regime. Using the radial width of a banana orbit as the typical step length of the particles due to a collision instead of the Larmor radius, leads to a diffusion coefficient smaller than the Pfirsch-Schlüter coefficient:

$$D \propto D_{class} q^2 \epsilon^{-3/2}. \tag{2.3.7}$$

Figure 2.3.2 shows a scheme of the transport regimes. In the Pfirsch-Schlüter and in the banana regime the diffusion coefficients depend on the collision frequency. The diffusion in the intermediate plateau regime, characterised by

$$\epsilon^{3/2} << \frac{\nu qR}{v_T} << 1, \tag{2.3.8}$$

is independent of the collisionality. Here most of the untrapped particles can complete their orbits without being disturbed by collisions. The trapped particles are disturbed by collisions since the effective collision frequency $\nu_{eff} = \nu/\epsilon$, required to scatter them out of their magnetic mirror $\Delta B/B \propto \epsilon$, is larger than the bounce frequency ω_b. This implies

$$\frac{\nu_{eff}}{\omega_b} = \frac{\nu qR}{\epsilon^{3/2} v_T} >> 1. \tag{2.3.9}$$

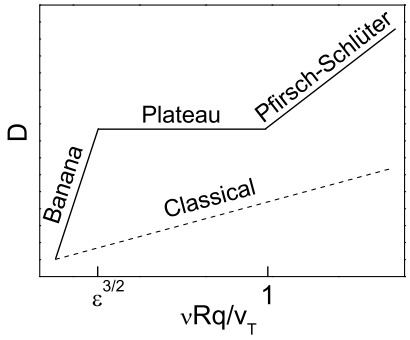

Figure 2.3.2: Qualitative representation of the neoclassical diffusion coefficient D of the transport of plasma particles in comparison to the classical diffusion coefficient

The value of the diffusion coefficient of the plateau regime matches the high and low collision diffusion at the appropriate collision frequencies. The three neoclassical regimes are that clear only in the limit $\epsilon \to 0$. For realistic aspect ratios the transitions between the regimes are smooth and there is no pronounced plateau in the curve. All the neoclassical diffusion coefficients are higher than the classical one.
Nevertheless, in tokamaks the experimentally observed electron transport is two orders of magnitude higher than the neoclassical predictions. The reason for this anomalous transport is found in electromangnetic turbulences in the plasma. The electrostatic contribution of the turbulences leads to $E \times B$ drifts which enhance the transport. In addition, small scale magnetic turbulences are always present in a tokamak plasma. They cause transient radial excursions of the magnetic field lines and thus enhance the transport substantially. Deviating from the ideal magnetic topology, macroscopic perturbations can occur and thus the nested tori can partially be destroyed. By a reconnection of the magnetic field lines, magnetic islands can be formed. In figure 2.3.3 a chain of magnetic islands can be seen within the plasma. Each magnetic island consists itself of a sequence of nested magnetic surfaces. Due to the formation of magnetic islands, the confinement is considerably degraded as the transport across the islands is enhanced. The radial overlap of several neighbouring island chains can lead to a complete ergodisation of the magnetic field lines. This means the field lines wander around in the ergodic region in a random manner and in a finite number of turns they come arbitrarily close to every point in this volume. Thus, the field lines are no longer bound to a surface, rather they fill out a volume which short-circuits the transport. Such a stochastic region is indicated at the plasma edge in figure 2.3.3.
Perturbed magnetic topologies, as described above, can for example be caused by the occurrence of a tearing mode [30]. This plasma instability involves an

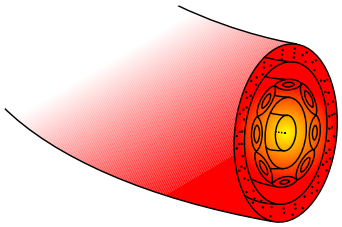

Figure 2.3.3: Scheme of a perturbed magnetic topology of a tokamak including a chain of magnetic islands and a fully ergodic edge region

unstable current density profile which leads to the tearing up and a subsequent reconnection of magnetic field lines. Consequently, magnetic islands start to grow at certain low order rational magnetic surfaces. If the magnetic islands grow too big and the degradation of the confinement is too large, the tearing mode results in a violent termination of the discharge - in a disruption.

2.4 Disruptions

In a tokamak the space of allowed operational parameters is restricted by several limits. Crossing a soft limit leads to a degradation of the plasma performance, the confinement becomes worse and more energy has to be supplied to keep the system working. Other limits are more strict. Crossing them eventually ends in a complete loss of the plasma confinement and hence a crude termination of the discharge by a disruption [16, 17, 21, 22, 31]. During such a serious event the energy stored in the plasma is expelled to the machine's walls in form of high heat fluxes. The plasma current decays exponentially fast to zero. Large magnetic forces arise and act on the machine's structures. Due to their dramatic consequences, disruptions pose a major problem for future large tokamaks with large plasma currents as ITER. Generally spoken, there are two main causes which can trigger a disruption: strong radiation from the plasma and MHD instabilities. Crossing a hard operational limit leads to one of the two causes.
The low q_a-limit is a well known hard restriction. q_a is the safety factor at the plasma boundary $r = a$. For a stable operation $q_a \geq 2$ is mandatory which presents a restriction on the maximum plasma current at a given magnetic field, $I_p(B_t)$. Increasing I_p moves the $q = 2$-surface outwards towards the plasma

edge. As the profile of the safety factor at the plasma centre is flattened by the sawtooth instability, the gradient of the q-profile becomes steeper. When $q = 2$ reaches the boundary, this is an unstable situation and a $m = 2$, $n = 1$ kink instability grows to a destructive level which leads to the disruption.

The density limit restricts the electron density $n_e(I_p)$ to a maximum value

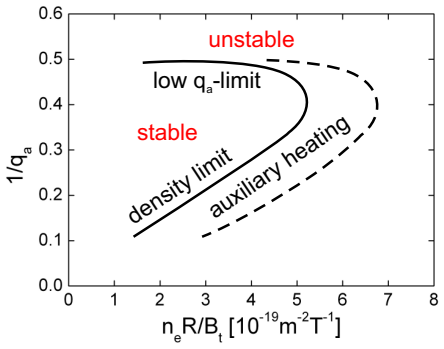

Figure 2.4.1: Qualitative representation of a Hugill diagram showing the region of stable operation of a tokamak

due to the radiation which in a plasma consists of bremsstrahlung, electron cyclotron emission (ECE) and line radiation. The latter is emitted by the plasma fuel, deuterium, but also by impurities. When the impurity density increases, the atoms, which carry much more electrons than deuterium, cannot be fully ionised at the plasma edge as the temperature is not high enough. The partially ionised impurities radiate strongly and cool down the edge region. A contraction of the current profile and an increase of the current gradient within the $q = 2$-surface are the consequences. Eventually, the situation becomes unstable and ends in a disruption. The density limit on the maximum allowed line averaged electron density was calculated by Greenwald [32]:

$$\overline{n_e} = \kappa \bar{j}. \tag{2.4.1}$$

Here κ is a measure for the elongation of the poloidal plasma cross section. The Greenwald limit can be pushed to higher densities by utilising auxiliary heating which allows higher losses due to radiation. Nevertheless, beyond the Greenwald limit the plasma performance is degraded which makes such a situation less convenient. Moreover, without additional heating the limit is only reached transiently as already below the onset of a neoclassical tearing mode is triggered.

The low q_a-limit and the density limit are often displayed in a Hugill diagram which shows the allowed operational space for a machine. A schematic example including the extension of the operational space by applying auxiliary heating can be seen in figure 2.4.1. There is also a number of limits which are not obvious in a Hugill diagram.

Magnetic field errors showing a low amplitude deviation from axisymmetry can be sufficient to promote the growth of tearing modes which can lead to a disruption. Tearing modes are a resistive instability which includes a reconnection of the magnetic flux surfaces to form magnetic islands. The islands can grow to sizeable widths until saturation is reached. This modifies the current density profile at the plasma edge which can become unstable.
The vertical instability is especially relevant for plasmas with an elongated cross section. These plasmas are unstable to motions in the direction of the elongation which is typically the vertical one. This can lead to a vertical displacement event (VDE), the plasma touching the wall and eventually a disruption.
The ideal β-limit was calculated by Troyon [33]. β is the ratio of the plasma pressure to the magnetic field pressure and hence presents a measure of the effectivity of the confinement,

$$\beta = \frac{2\mu_0 \langle p \rangle}{B^2}. \tag{2.4.2}$$

The angled brackets imply a volume averaged pressure. At maximum β and hence high performance the maximum plasma pressure is confined by a given magnetic field.
Finally and rather obviously, also UFOs, fragments detached from the wall and falling into the plasma, can cause a disruption.
The evolution of a disruption can be described in several phases. At first some event has to initiate an unstable situation, mostly by a modification of the current density profile. Then a precursor phase sets on to show magnetic oscillations. These oscillations result from the motion of a helical perturbation of the magnetic configuration. In order to describe the instability, often a Fourier decomposition is chosen:

$$\zeta(r,t) = \zeta(r) \exp i(\omega t + m\theta - n\varphi) \tag{2.4.3}$$

where θ is the poloidal angle, φ is the toroidal angle and m and n are the poloidal and toroidal mode numbers of the perturbation, respectively. The nonlinear growth of such instabilities leads to the loss of the confinement. β-limit disruptions are often preceeded by neoclassical tearing modes [30, 34]. Before most other disruptions a mixture of modes, in particular including $m/n = 3/2$ and $m/n = 2/1$ modes, is often observed as a precursor.
The next two phases are the main parts of the disruption. During the thermal quench the plasma confinement is lost and the plasma temperature drops to a few eV. The thermal energy is expelled to the wall. The whole phase lasts only a few ms. In the next phase, the current quench, the plasma current decays exponentially to zero within some tens of ms. If a sizeable amount of REs is generated, the current decay can be retarded up to hundreds of ms. The reason is the low collisionality of the REs. The complexity of the disruption development and the variance in the details of the thermal and the current quench hamper theoretical predictions and the modelling of disruptions which is an ongoing field of research.

There are several harmful aspects for which disruptions have to be avoided. The high heat fluxes onto the wall during the thermal quench can cause erosion or even melting of the wall materials and hence reduce the lifetimes of the PFCs. Large forces on the vessel and the support structures can stem from a displacement of the plasma column. If it hits the wall, a fraction of the plasma current can be driven through the wall elements. Such halo currents cause large $j \times B$ forces and are especially severe during a VDE. The REs, which can be generated during the current quench phase, are studied in this thesis. The high energetic electrons can strike the wall and lead to the localised deposition of severe amounts of energy. A detailed discussion of disruptions with REs will be given in the third chapter.
The list of dangers caused by disruptions becomes even more critical going to reactor regime tokamaks like ITER. While the size of the machine increases, the thermal energy stored in the plasma increases with the plasma chamber volume and thus to the third power of the machine's dimensions. The wall area which has to take the deposition of the thermal energy increases only to the second power of the machine size. Consequently, such dramatic events as disruptions have to be avoided whenever possible. This requires the prediction of impending disruption occurrences in order to keep the plasma away from critical operational conditions. Corresponding actions have to be taken before the onset of the precursor or before the precursor growth leads to the irreversible onset of the thermal quench. In the optimal case the plasma can be kept from leaving the stable operational conditions. Neural networks have been trained to identify stable and unstable regions of the operational phase space [35–37]. The next best solution is to detect and stabilise the precursor modes by the input of heating power or particle momentum [30, 38, 39]. If the disruption is already unavoidable, it has to be mitigated or the harmful effects have to be ameliorated. The injection of massive amounts of gas [40–50] or of killer pellets [51–53] into the vessel are used to mitigate forces and heat loads. The suppression or mitigation of REs is more demanding. Techniques being studied are presented at the end of the following chapter.

3 Review of Runaway Electrons in Tokamaks

This chapter introduces the phenomenon of the electron runaway in tokamaks which is comprehensively reviewed in [18, 54, 55]. The generation mechanisms of runaway electrons are reviewed before some physical properties, which distinguish the relativistic electrons from the thermal ones, are discussed. The orbits, the transport and the energy of the runaways are treated to set up the background required for the presentation of the studies in the chapters 5 and 6. After the common possibilities to detect runaways are described, an overview of the operational regimes in tokamaks which can include the generation of runaway electrons is given. As the physcis of the runaway electrons in disruptions are a main issue of this thesis, an emphasis is put on describing the evolution of disruptions in which runaways are generated. The chapter ends with a brief discussion of the runaway mitigation schemes which are currently being studied or are proposed, i.e. for ITER. A discussion of the runaway electrons in view of ITER disruptions including mitigation techniques is given in [21]. Accessible introductions to runaway electrons can be found in [56, 57].

3.1 Electron Runaway

The runaway phenomenon was first identified by C.T.R. Wilson[3]. It is a basic aspect of the kinetic theory of ionised gases and a direct consequence of the long range, small angle scattering which is characteristic for collisional interactions of plasma particles. The runaway of plasma ions is studied in [58]. It is shown that at high enough resistivities a small fraction of the ions in a tokamak plasma can runaway. Plasma electrons are much more prone to runaway and thus the runaway of electrons can occur in various kinds of plasmas, for example in astrophysical ones [59] and in thunder storms where it provides a breakdown mechanism for the production of lightning. Runaway effects are even found numerically in solid-state physics [60, 61]. Relativistic REs have been studied in toroidal plasma devices since the midfifties. From the very beginning of tokamak physics REs have been detected [62–64]. In tokamak plasmas REs can be produced during the startup phase, in ohmic discharges at low densities and in the current quench phase of disruptions. Avoiding the generation of a substantial RE population is highly desired in large fusion devices because the high energetic electrons can strike the vessel wall and deposit their energy quite locally which may cause material damages. In addition, a large RE population hampers the ohmic heating as the heating energy is transferred to the REs which are practically decoupled from the bulk plasma and hence don't share the energy.

The mandatory requirement for the generation of REs in a plasma is the presence of an electric field E parallel to the magnetic field. Since the tokamak plasma is the secondary winding of a transformer, there is always a voltage around the toroidal loop and hence an electric field which is almost DC. This field exerts

[3] Wilson is well known for inventing the cloud chamber.

an accelerating force $F_E = eE$ on the plasma electrons along the magnetic field where e is the electron charge. In the opposite direction Coulomb collisions with the background plasma cause a drag force $F_C = m_e v \cdot \nu(v)$. m_e is the rest mass of an electron, v the velocity of a test electron population relative to the bulk electrons and ions and $\nu(v)$ is the frequency of the collisions with the bulk plasma. Following a relativistic derivation, given in [65], the drag force is

$$F_C^c = \frac{e^4 n_e \ln(\Lambda)}{4\pi\epsilon_0^2 m_e v^2}\left(1 + \frac{Z_{eff}+1}{\gamma}\right). \tag{3.1.1}$$

n_e is the electron density, $\ln(\Lambda)$ the Coulomb logarithm and ϵ_0 the vacuum permittivity. The effective charge of the plasma ions is calculated as $Z_{eff} \equiv \sum_i n_i Z_i^2/n_e$, where i denotes the ion species in the plasma and n_i is the ion density. $\gamma \equiv (1-(v/c)^2)^{-1/2}$ is the relativistic parameter with c the speed of light. A nonrelativistic expression for the drag force can be given as

$$F_C = \frac{e^4 n_e \ln(\Lambda)}{4\pi\epsilon_0^2 m_e v^2}(2 + Z_{eff}). \tag{3.1.2}$$

$F_C(v)$ has a global maximum at the thermal velocity v_T. At velocities $v >> v_T$ the collision frequencies with electrons and ions decrease strongly with increasing velocity, $\nu \propto v^{-3}$. Hence, $F_C \propto v^{-2}$. For electrons which exceed a critical velocity v_{crit} the acceleration by the electric field decreases the decelerating drag force and hence further acceleration takes place. This is the unstable situation illustrated in figure 3.1.1 and called electron runaway. The critical

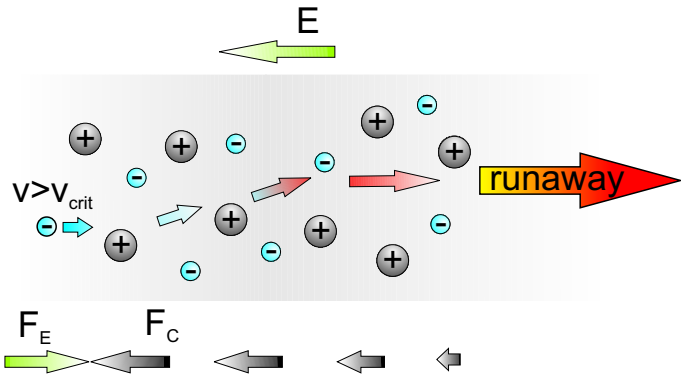

Figure 3.1.1: Schematic visualisation of the runaway of the plasma electrons with velocities v higher than the critical velocity v_{crit} due to the electric field E causing the accelerating force F_E which acts in the opposite direction to the collisional friction force F_C

velocity above which the onset of the runaway can take place is calculated by balancing the two forces, $F_E = F_C$.

$$v_{crit} = \sqrt{\frac{e^3 n_e \ln(\Lambda)(2+Z_{eff})}{4\pi\epsilon_0^2 m_e E}} \tag{3.1.3}$$

The corresponding nonrelativistic critical electron energy is

$$W_{crit} = \frac{1}{2} m_e v_{crit}^2 = \frac{e^3 n_e \ln(\Lambda)}{8\pi\epsilon_0^2 E}(2 + Z_{eff}). \tag{3.1.4}$$

Setting $W_{crit} = 1/2 \cdot m_e v_T^2$ the critical electric field of the electron runaway can be estimated:

$$E_{crit} = \frac{e^3 n_e \ln(\Lambda)}{4\pi\epsilon_0^2 m_e v_T^2}(2 + Z_{eff}) = \frac{e^3 n_e \ln(\Lambda)}{8\pi\epsilon_0^2 T_e}(2 + Z_{eff}). \tag{3.1.5}$$

Here $T_e = 1/2 \cdot m_e v_T^2$ is the electron temperature in J. The given critical electric field is larger than the critical field which neglects the electron-electron collisions and assumes $Z_{eff} = 1$:

$$E_D = \frac{e^3 n_e \ln(\Lambda)}{4\pi\epsilon_0^2 T_e}. \tag{3.1.6}$$

This field is named after Dreicer who brought to attention [66] what was found earlier in [67, 68].
In order to estimate the electron runaway in a plasma with a given electric field, the parameter $\epsilon \equiv E/E_{crit}$ is defined. If $\epsilon >> 1$, the bulk of the plasma, the thermal part of the Maxwell distribution, runs away and thus the plasma is not in a steady state and the distribution will not stay Maxwellian. In the case of $\epsilon << 1$, the thermal bulk of the plasma is in a steady state and its velocity distribution is Maxwellian. Only the small part of the electrons which is in the high energy tail of the distribution can run away. In the course of the runaway the tail is pulled to higher and higher energies by the electric field, but the main part of the distribution stays approximately Maxwellian. This situation is called a quasi steady state. The exact distribution function can be calculated by means of the Fokker-Planck equation utilising the appropriate operator to describe the collisions of the fast electrons with the thermal electrons and ions. The typical parameters of a purely ohmic RE discharge at TEXTOR are $n_e = 10^{19}\,\mathrm{m}^{-3}$, $\ln(\Lambda) = 16$, $Z_{eff} = 2$ and $T_e = 1.5\,\mathrm{keV}$. The loop voltage $U_{loop} = 1\,\mathrm{V}$ causes a parallel electric field of about $E = 0.1\,\mathrm{V/m}$. Consequently, the critical velocity of the electron runaway is $v_{crit} \approx 0.57c$ which corresponds to an energy of $W_{crit} \approx 80\,\mathrm{keV}$. As $\epsilon \approx 0.02$, the distribution function can be assumed to stay Maxwellian. In the current quench phase of TEXTOR disruptions the loop voltage is much higher. $U_{loop} \approx 40\,\mathrm{V}$ leads to an electric field which is of the order of 10 times the one in the stationary discharges. Simultaneously, the plasma is cold during the current quench ($T_e \approx 5\,\mathrm{eV}$) and Z_{eff} increases due to the influx of impurities. Thus, E_{crit} is larger by a factor of the order of 1000. Eventually, ϵ is even smaller than in the ohmic discharges and the plasma is commonly assumed to be thermal.

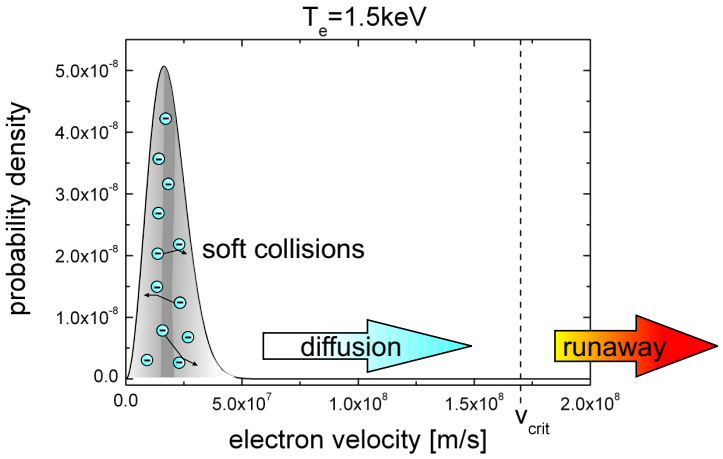

Figure 3.2.1: Schematic visualisation of the primary RE generation indicating the diffusion of the plasma electrons with velocities above $v_{crit} \approx 0.57c$ out of a Maxwell distribution with $T_e = 1.5\,\mathrm{keV}$ due to small angle collisions

3.2 Generation

3.2.1 Primary Generation

As described above, for $\epsilon << 1$ only the high energy tail of the Maxwell distribution runs away. The RE production due to the phase space diffusion of electrons into the tail, where $v > v_{crit}$, is called primary RE generation or the Dreicer mechanism. The diffusion in phase space is a cumulative effect of multiple small angle collisions. They cause the diffusion rate of the electrons with velocities around v_{crit} and therefore determine the birth rate of the REs. A calculation of the primary RE birth rate requires solving the steady state kinetic equation

$$-\frac{eE}{m_e}\frac{\partial f}{\partial v} = C(f). \tag{3.2.1}$$

Here f is the distribution function. $C(f)$ is the Fokker-Planck collision operator of the collisions of the fast electrons with the thermal electrons and ions. Inserting it, the equation reads

$$\begin{aligned} &-\tfrac{eE}{m_e}\left(\tfrac{\partial f}{\partial v} + \tfrac{1-\xi^2}{v}\tfrac{\partial f}{\partial \xi}\right) \\ &= \nu_{ee} v_T^3 \left[\tfrac{1-Z_{eff}}{2v^3}\tfrac{\partial}{\partial \xi}(1-\xi^2)\tfrac{\partial f}{\partial \xi} + v^{-2}\tfrac{\partial}{\partial v}\left(f + \tfrac{T_e}{m_e v}\tfrac{\partial f}{\partial v}\right)\right]. \end{aligned} \tag{3.2.2}$$

ν_{ee} is the electron-electron collision frequency and $\xi = v_{||}/v$ is the cosine of the pitch angle. E is the electric field parallel to the magnetic field and the orbit of the electron guiding centres. Following the nonrelativistic approach briefly

reviewed in [18] and carried out in detail in [69–71], the rate of the primary RE generation can be written as

$$\frac{dn_{RE1}}{dt} = \lambda_{RE}\nu_{ee}n_e \tag{3.2.3}$$

where the dependence of the diffusion on the collision frequency can be found. The crucial dependence on the electric field is contained in

$$\lambda_{RE} = K(Z_{eff})\epsilon^{*-3(Z_{eff}+1)/16}\exp\left(-\frac{1}{4\epsilon^*} - \sqrt{\frac{1+Z_{eff}}{\epsilon^*}}\right). \tag{3.2.4}$$

Thus, the primary generation is an exponential function of $\epsilon^* \equiv E/E^*_{crit}$ with

$$E^*_{crit} = \frac{e^3 n_e \ln\Lambda}{4\pi\epsilon_0^2 m_e v_T^2}. \tag{3.2.5}$$

The latter is the critical electric field defined without the dependence on Z_{eff} which explicitly appears in λ_{RE}. The function $K(Z_{eff})$, given in [71], is only weakly changing[4]. It has a local maximum between $Z_{eff} = 2$ and 3.
Of course, in the relativistic limit the runaway process has to cease. In the regime $v \approx c$, $\gamma >> 1$ the friction force is given by equation 3.1.1. Above a velocity v^c the friction force stays approximately constant and so it doesn't fall to zero. The velocities $v \geq v^c$, for which the relativistic effects become important, can be calculated by balancing the friction force and the accelerating force, $F^c_C = F_E$.

$$v^c = \epsilon^{-1/2} v_T \left(1 + \frac{Z_{eff}+1}{\gamma}\right) \tag{3.2.6}$$

An exponential correction factor of the RE birth rate, taking into account the relativistic effect, is calculated in [72].

$$\lambda^c_{RE} = \lambda_{RE}\exp\left(-\frac{T_e}{m_e c^2}\left(\frac{1}{8}\epsilon^{*2} + \frac{2}{3}\epsilon^{*3/2}\sqrt{1+Z_{eff}}\right)\right) \tag{3.2.7}$$

The correction vanishes for $E < E^*_{crit}(v = c)$ and thus no REs are generated.

3.2.2 Secondary Generation

The primary RE generation is described as a diffusion in phase space due to multiple small angle collisions. Although less often, also collisions resulting in large deflection angles occur in plasmas. These hard collisions are mostly unimportant for plasmas with $\ln\Lambda >> 1$ unless REs are present. If a seed population exists, these REs can knock thermal electrons into the runaway regime and hence create secondary REs while staying above the runaway threshold themselves. Eventually, this leads to an exponential growth of the RE population which justifies the name RE avalanching also used for the secondary generation

[4] $K(1) = 0.32$, $K(2) = 0.43$, $K(3) = 0.42$, $K(10) = 0.13$

mechanism. The process was first mentioned in [73] and studied in detail in [74–76]. The relativistic drift-kinetic equation is solved in the orbit-average in [76].

$$-\frac{eE\xi}{m_e c}\left(\frac{\partial f}{\partial p}-\frac{2\lambda}{p}\frac{\partial f}{\partial \lambda}\right)=C(f)+S \tag{3.2.8}$$

Here $p=\gamma v/c$ is the normalised relativistic momentum and $\lambda=(1-\xi^2)/B$ is the magnetic moment variable. The relativistic Fokker-Planck collision operator

$$C(f)=\frac{1}{\tau p^2}\left[\frac{\partial}{\partial p}(1+p^2)f+\frac{1+Z_{eff}}{2}\sqrt{1+p^{-2}}\frac{\partial}{\partial \xi}(1-\xi^2)\frac{\partial}{\partial \xi}\right] \tag{3.2.9}$$

includes pitch angle scattering and the slowing down but not the energy diffusion which means the primary generation. The collision time of the relativistic electrons is $\tau=(c/v_T)^3\nu_{ee}^{-1}$. The source term of the fast electrons due to hard collisions S is given explicitlely in [76, 77]. It is proportional to the density of the RE seed population n_{RE} and the frequency of the hard collisions $(\tau\ln\Lambda)^{-1}$ rather than the usual Fokker-Planck collision frequency τ^{-1}. An interpolation formula which gives the RE birth rate due to the secondary generation was found from analytical solutions in several limits and it is presented in [76].

$$\frac{dn_{RE2}}{dt}\cong \frac{(\epsilon^*(c)-1)n_{RE}}{\tau\ln\Lambda}\sqrt{\frac{\pi\varphi}{3(Z_{eff}+5)}}\left(1-\frac{1}{\epsilon^*(c)}+\frac{4\pi(Z_{eff}+1)^2}{3\varphi(Z_{eff}+5)(\epsilon^*(c)^2+4/\varphi^2-1)}\right)^{-1/2} \tag{3.2.10}$$

Here $\epsilon^*(c)=E/E^*_{crit}(v=c)$. $\varphi=1-1.46(r/R)^{1/2}+1.72(r/R)$ implements the effect of a finite aspect ratio R/r. A much simpler expression of the birth rate can be given in the limit of $\epsilon^*(c)>>1$, $Z_{eff}=1$ and $r/R\to 0$.

$$\frac{dn_{RE2}}{dt}\cong\sqrt{\frac{\pi}{2}}\frac{(\epsilon^*(c)-1)n_{RE}}{3\tau\ln\Lambda} \tag{3.2.11}$$

The relative importance of the primary and the secondary RE generation depends on the existence of a seed population. In general if $\epsilon^*(c)>1$ and $n_{RE}>0$, avalanching seems to dominate at sufficient low electric fields as the primary process is exponentially small in ϵ. The first experimental evidence of the avalanching was found in ohmic TEXTOR low density discharges [78]. In this regime the secondary process is believed to play the dominant role. New results, contributing to the picture, are presented in chapter 6 of this thesis. In disruptions the avalanching is predicted to occur and even to dominate [79, 80]. As all the REs are expelled from the plasma during the thermal quench, a seed population must be generated by the primary or another process during the current quench. In ITER a RE seed could be provided by Compton electrons, produced by the emission of X-rays from the wall, or by the electrons of the tritium decay.

3.2.3 Hot Tail Generation

Another mechanism which can cause the generation of a RE population during disruptions is proposed in [81, 82]. During the thermal quench phase of tokamak disruptions the electron velocity distribution is not necessarily in a steady state as it is assumed in the derivation of the primary (Dreicer) generation rate. At high electron velocities the collision frequency can be smaller than the cooling rate of the plasma electrons. If this is the case, during a transient phase the high energy electrons do not have enough time to thermalise. They form a hot tail of the low energy bulk distribution. The latter is a Maxwellian with a decreasing temperature $T(t)$. If the time during which the plasma cools down is comparable to the collision time of the electrons which have velocities close to the runaway threshold, the buildup of a hot tail increases the number of the electrons in the runaway regime above the number which would result from a purely Maxwellian distribution at the temperature $T(t)$. The consequence is the abrupt generation of more REs than given by the primary generation rate. Using $T_e = 1/2 \cdot m_e v_T^2$ and equation 3.1.6 for the Dreicer field E_D, the critical velocity of the electron runaway v_{crit} (equation 3.1.3) can be written like it is done in [81]:

$$v_{crit} = v_T \sqrt{\frac{E_D}{2E}} \tag{3.2.12}$$

where E is the parallel electric field. During the approximately 1 ms long thermal quench phase the plasma inductance keeps the parallel plasma current $j_{||}$ constant. The resistivity of the plasma depends on its temperature, $\eta \propto T^{-3/2}$ [10, 83]. Thus, as long as the RE current is negligible the electric field depends on the temperature in the same way, $E = \eta j_{||} \propto T^{-3/2}$. Assuming the electron density to be constant, a normalised critical velocity of the electron runaway can be written as

$$x_c(t) = \frac{v_{crit}}{v_T} = \sqrt{\frac{E_{D0}}{2E_0}} \left(\frac{T(t)}{T_0} \right)^{1/4}. \tag{3.2.13}$$

The subscripts 0 denote the initial values of the corresponding parameters. As $T(t)$ decreases, x_c decreases in time as well and the electrons with velocities exceeding x_c do not have the time to thermalise. They run away in energy space. Usually, the electron density is not constant during a disruption, rather it increases due to the influx of impurities during the thermal quench. The corresponding effects are studied in [81]. The hot tail generation is studied numerically in [77, 84]. The injection of pellets into high temperature plasmas, which leads to the abrupt generation of REs, is simulated. Analytical studies are carried out in [81, 85, 86]. An experimental observation of the hot tail generation is described in [87]. The experiments were performed in DIII-D where the thermal quenches were induced by the injection of high atomic number killer pellets. It was found that the generation of REs sensitively depends on the cooling rate and the final temperature of the plasma.

3.3 Orbits

A toroidal coordinate system is introduced as a tool to decribe the orbits of the relativistic electrons in the ideal magnetic tokamak topology. ϕ denotes the toroidal angle, θ the angle in a poloidal plane and r the direction along the minor radius. The transformation of Cartesian unit vectors into the toroidal counter parts is done via

$$\begin{aligned} e_\phi &= -\sin\phi e_x + \cos\phi e_y, \\ e_\theta &= \sin\theta\cos\phi e_x + \sin\theta\sin\phi e_y + \cos\theta e_z, \\ e_r &= -\cos\theta\cos\phi e_x - \cos\theta\sin\phi e_y + \sin\theta e_z. \end{aligned} \tag{3.3.1}$$

Figure 3.3.1 illustrates the geometry of the coordinates. The motion of the REs

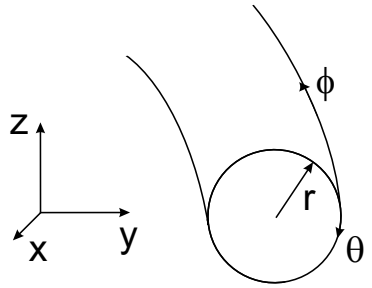

Figure 3.3.1: Overview of the geometry of Cartesian and toroidal coordinates

in the magnetic field of a tokamak is described by the velocity vector including contributions from the cyclotron, the guiding centre and the drift motion.

$$v = v_{cycl} + v_{gc} + v_{drift}. \tag{3.3.2}$$

The cyclotron motion of a charged particle in a magnetic field has been introduced in chapter 2. The cyclotron frequency and the Larmor radius of a relativistic electron are

$$\omega_{c,RE} = \frac{eB}{\gamma m_e}, \tag{3.3.3}$$

$$r_{L,RE} = \frac{\gamma m_e v_\perp}{eB}, \tag{3.3.4}$$

respectively. $v_\perp$ is the fraction of the velocity perpendicular to the magnetic field. The velocity vector of the gyration is

$$v_{cycl} = v_{bot}\left[\cos\alpha e_r + \sin\alpha(e_\theta - \frac{r}{q(r)R}e_\phi)\right]. \tag{3.3.5}$$

α is the phase angle of the cyclotron motion which is determined by $d\alpha/dt = -\omega_{c,RE}$. In the description q is assumed to be a function of r but not of θ.

This is not exactly true as $B \propto 1/R$ and thus there is a difference between the magnetic field on the inner and outer sides of the torus.
The second contribution in equation 3.3.2 takes the motion of the guiding centre of a test particle into account. The guiding centre is the centre of mass of the electron averaged over the cyclotron motion. Due to the helical winding of the magnetic field lines, the guiding centre motion has contributions in the directions of ϕ, θ and z.

$$\begin{aligned} v_{gc} &= v_{||}e_\phi + v_\theta + v_z \\ &= v_{||}e_\phi + \frac{v_{||}r}{Rq(r)}e_\theta - v_{||}\frac{B_z}{B_t}e_z \\ &= v_{||}e_\phi + \frac{B_p(r)}{B_t}e_\theta - v_{||}\frac{B_z}{B_t}e_z \end{aligned} \tag{3.3.6}$$

B_z is the contribution of the magnetic field in the vertical direction. As described in chapter 2, the helical magnetic field short-circuits the charge separation caused by the particle drifts.
Nevertheless, the drifts are present and with regard to the REs they lead to a drift velocity contribution of

$$v_{drift} = \frac{1}{R_{mag}\omega_{c,RE}}(v_{||}^2 + \frac{1}{2}v_\perp^2)e_z. \tag{3.3.7}$$

R_{mag} denotes the radius of the curvature of the magnetic field lines. The left term is the contribution of the curvature drift and the right term is the ∇B-drift. The $E \times B$-drift is negligible for the REs.
Summing up the three contributions to the RE motion yields

$$\begin{aligned} v &= v_{bot}\left[\cos\alpha e_r + \sin\alpha(E_\theta - \frac{r}{q(r)R}e_\phi)\right] + v_{||}(\frac{r}{q(r)R}e_\theta + e_\phi) \\ &+ \left[\frac{1}{R_{mag}\omega_{c,RE}}(v_{||}^2 + \frac{1}{2}v_{bot}^2) - \frac{B_z}{B_t}\right]e_z \end{aligned} \tag{3.3.8}$$

Figure 3.3.2 schematically shows a RE orbit. The cyclotron gyration and the movement of the guiding centre along a helical trajectory can be seen. In addition, the drift orbit surface appears to be outward shifted with respect to the magnetic flux surface. This is an effect of the drift velocity which occurs for the REs with $v_{||} >> v_\perp$. In the first order the shift can be calculated as

$$d \approx \frac{\overline{q}\gamma m_e v_{||}}{eB} \approx \frac{\overline{q}W_{RE}}{ecB}. \tag{3.3.9}$$

$\overline{q}$ is the safety factor averaged over a drift surface and W_{RE} is the RE energy. Thus, the outward shift is a function of the RE energy. In TEXTOR the shift is typically a few cm. Higher order effects of the drifts are studied in [88, 89]. The classical perturbation theory is used for a Hamiltonian description of the guiding centre motion of the relativistic electrons in a toroidal, axially symmetric magnetic field. It is found that while a given electron is accelerated, the

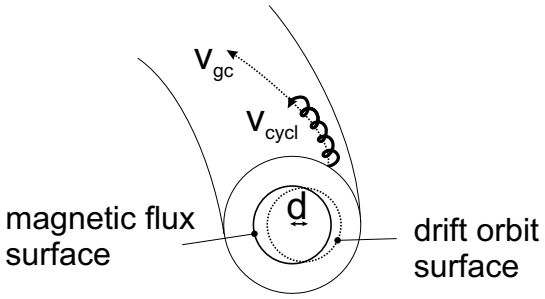

Figure 3.3.2: Schematic illustration of the orbit of a RE being determined by the guiding centre motion v_{gc}, the cyclotron gyration v_{cycl} and the shift d of the drift orbit surface with respect to the magnetic flux surface

rotational transform of the drift orbit surface $1/q_{drift}$ decreases. The rotational transform is the inverse of the safety factor and thus a measure for the helical winding of the orbits. During the acceleration the radius of the orbit stays almost constant. Consequently, the minor radius of the drift orbit surface at a fixed $1/q_{drift}$ has to decrease and thus it becomes smaller than the radius of the magnetic flux surface with the same rotational transform $1/q = 1/q_{drift}$. On the latter magnetic surface the particle would be if it had zero energy. Additionally, the outward shift of the drift orbit surfaces is larger than the classical value given above. In conclusion, the ouward shift and the minor radius of the drift orbit surfaces are functions of the RE energy.

3.4 Transport

In chapter 2 the collisional neoclasscial transport of the thermal electrons has been introduced. The experimentally observed anomalous transport has been explained as an effect of the electromagnetic turbulences. REs are characterised by a much better confinement than the one of the thermal electrons. Hence, the transport of the REs is substantially different from the transport of the thermal electrons. In the following the three mechanisms which may have an influence on the RE transport will be briefly discussed.

3.4.1 Collisions

Assuming a Maxwell distribution, the collision frequency of the electrons is

$$\nu_e = \frac{|dp/dt|}{p} = \frac{|F_C + eE|}{\gamma m_e v}. \tag{3.4.1}$$

In tokamaks typically $eE << F_C$ and the electric fields can be neglected in the expression of the collision frequency. This results in

$$\nu_e = \frac{|F_C|}{\gamma m_e v} = \frac{e^4 n_e \ln\Lambda(Z_{eff}+2)}{4\pi\epsilon_0^2 m_e^2 v^3}. \tag{3.4.2}$$

From this a collision time of $\tau_{RE} = \nu_{RE}^{-1} \approx 10\,\mathrm{s}$ can be estimated for high energy REs, assuming $\gamma = 60$. The Larmor radius of the REs in TEXTOR low density discharges was measured by the detection of the synchrotron radiation as $r_{L,RE} \approx 5\,\mathrm{mm}$. This results in a classical diffusion coefficient of the order of

$$D_{class,RE} = \frac{r_{L,RE}}{\tau_{RE}} \propto 10^{-6}\,\frac{\mathrm{m}^2}{\mathrm{s}}. \tag{3.4.3}$$

The low collisionality of the REs leads to a very low transport due to collisions. In addition, REs cannot be trapped and excert banana orbits as their parallel velocity is too high. Eventually, collisions are not the dominant mechanism of the RE transport.

3.4.2 Electrostatic Turbulence

Fluctuating electric fields can cause an enhancement of the cross field transport due to $E\times B$ drifts. A fluctuating electric field $\tilde{E}$ perpendicular to B causes a drift velocity $\tilde{v} \propto \tilde{E}/B$. Assuming a random walk of the particles, $\tilde{v}$ causes a radial displacement $\Delta r \approx \tilde{v}\tau_{trans}$ where $\tau_{trans} = \pi qR/v_{||}$ is the transition time. It follows a diffusion coefficient caused by electrostatic turbulences of

$$D_E = \frac{\langle(\Delta r)^2\rangle}{\tau} \approx \tilde{v}^2\tau_{trans} \approx \frac{\pi qR}{v_{||}}\left(\frac{\tilde{E}}{B}\right)^2. \tag{3.4.4}$$

For REs $v_{||}$ is very high and D_E is believed to be small and not the effect which dominates the RE transport.

3.4.3 Magnetic Turbulence

The plasma particles follow the turbulent radial excursions of the magnetic field lines. Thus, the magnetic turbulence leads to a parallel transport which causes losses. In [90] this transport is described by the diffusion of the magnetic field lines. In a fully stochastic, static magnetic field the field line diffusion is estimated as

$$D_M \propto L_{||}\left(\frac{\tilde{B}}{B}\right)^2 \tag{3.4.5}$$

where $L_{||} \approx \pi qR$ is the correlation length of the fluctuations along B. The field $\tilde{B}$ denotes the magnetic fluctuations. In [90] a diffusion coefficient of the electrons of

$$D \propto v_{||} D_M \tag{3.4.6}$$

is concluded. But in [91] it is shown that the field lines in stochastic regions do not carry out Gaussian random walks as it was assumed in [90]. Rather, the role of the magnetic shear, the change Δq of the safety factor between adjacent magnetic surfaces, must not be neglected. Implementing the magnetic shear results in a weaker scaling of the electron diffusion coefficient with $v_{||}$.

$$D \propto v_{||}^{1/3} v_{\perp}^{1/3} \tag{3.4.7}$$

In addition, the drift orbit displacement weakens the effect of the magnetic turbulence as the REs are shifted from the fluctuating magnetic field lines [92, 93]. If $d > \delta$ with d the orbit displacement and δ the typical length scale of the turbulence, the effect of the magnetic turbulence on the RE transport is small. As d increases with increasing RE energy, the effect of the turbulence decreases with increasing RE energy. Thus, the drift orbit displacement can be interpreted as a shielding of the REs against the magnetic fluctuations [92].

$$D \propto \Upsilon v_{||} D_M \tag{3.4.8}$$

Here Υ is a shielding parameter. Up to now D_M and hence D have been estimated for the transport in fully stochastic magnetic fields. A realistic magnetic topology of a tokamak includes regions of regular flux surfaces as well. The transport of fast electrons in mixed topologies is studied in [94]. It is shown that in a structure consisting of regions with regular flux surfaces, magnetic islands and stochastic regions the transport is substantially lower than in a purely stochastic magnetic field.
Eventually, the electron diffusion coefficient increases with increasing parallel velocity $v_{||}$. Hence, magnetic fluctuations are believed to be the dominating mechanism regarding the RE transport. As the REs are quite sensitive to the magnetic structure, they can be used to probe the small scale magnetic turbulence and macroscopic perturbations. The other way round, perturbing the magnetic field in a well defined manner is an effective way to influence the RE transport.

3.5 Energy

For a given electron the runaway process can temporally be devided into three phases. The first phase comprises the birth of the REs at energies close to W_{crit}. In the second phase the energy of the REs is larger than W_{crit} up to energies at which the drift orbits are significantly displaced from the magnetic surfaces. Here collective interaction processes and the enhanced emission of electromagnetic waves become important. The confinement time of the REs is in the same range as the one of the thermal electrons. This changes in the third phase when the REs have energies above 1 MeV. The drift surfaces are shifted on a cm scale. Thus, the REs are less affected by the small scale magnetic turbulences and the confinement time exceeds the one of the thermal electrons. The further acceleration of the REs by the electric field experiences some limitations which will be briefly discussed.

3.5.1 Synchrotron Radiation

While the REs are accelerated in a toroidal electric field, they gain energy. The corresponding power is

$$P_{gain} = \frac{ecU_{loop}}{2\pi R} \tag{3.5.1}$$

with U_{loop} denoting the toroidal loop voltage. For the estimation the REs are assumed to travel at the speed of light although the calculation is nonrelativistic. The toroidal trajectories of the REs imply an angular acceleration of the charged particles and hence the emission of electromagnetic synchrotron radiation. The corresponding power loss [95, 96] is approximately

$$P_{loss} \approx \frac{2m_e c^3 r_e \gamma^4}{3R_c^2}. \tag{3.5.2}$$

Here $r_e = e^2/(4\pi\epsilon_0 m_e c^2)$ is the classical Thomson radius of the electron and R_c is given in [97] as

$$\frac{1}{R_c} \approx \frac{1-\theta^2}{R} + \frac{eB\theta}{\gamma m_e c} \tag{3.5.3}$$

with $\theta = v_\perp / v_{||}$ the pitch angle of the REs. The energy loss due to friction is comparably small and can be neglected. Thus, the change of the RE energy is a competition between the acceleration and the radiation losses.

$$\frac{dW_{RE}}{dt} = m_e c^2 \frac{d\gamma}{dt} = P_{gain} - P_{loss} \tag{3.5.4}$$

An upper limit of the RE energy W_{RE} is found from the power balance $P_{gain} - P_{loss} = 0$. The RE pitch angle was measured at TEXTOR during stationary RE discharges by the detection of the synchrotron emission. $\theta = 0.1$ was found [56]. Using $\gamma = 60$ for the upper limit on the RE energy, it follows $W_{max} \approx 30\,\mathrm{MeV}$ according to [56].

3.5.2 Drift Orbits

REs can only be confined within the plasma as long as the sum of the radius of their drift orbit surface and the orbit shift is smaller than the minor radius of the plasma. In a first approach the drift radius is assumed to be equal to the radius of the magnetic surface with $q = q_{drift}$. From equation (3.3.9) follows

$$W_{max} = \frac{aecB}{q_a} \approx 80\,\mathrm{MeV} \tag{3.5.5}$$

for the upper limit on the RE energy. For the calculation in [56, 57] an edge safety factor of $q_a = 3.8$, a plasma current of $I_p = 350\,\mathrm{kA}$ and a magnetic field of $B = 2.2\,\mathrm{T}$ are used. The values represent typical operational conditions of the stationary discharges in TEXTOR. The corresponding minor radius is

$a = 0.46\,\mathrm{m}$.
Going beyond the zeroth order approximation, the drift orbit radius decreases and the orbit shift increases with increasing RE energy as it has been shown above. The dependence of the drift orbit radius is stronger than the one of the orbit shift. Thus, the radius of a drift orbit surface can become so small that it lies completly within the magnetic surface. This effect can be more important for the energy limit than the orbit shift. In [56, 57] $q_a = 3.8$ and $I_p = 350\,\mathrm{kA}$ are assumed to calculate the energy at which the $q_{drift} = 1$ surface vanishes. It is found that $W_{max} \approx 60\,\mathrm{MeV}$. This limit increases for larger q_{drift} or smaller q_a. As the drift orbit limit is much higher than the radiation limit, it is not believed to be the dominating effect which limits the RE energy.

3.5.3 Lifetime

In stationary discharges the REs can be accelerated as long as the transformer action of the tokamak provides a magnetic flux swing. Not taking the radiation losses into account, it follows

$$W_{max}(t) = \int_0^t \frac{dW_{RE}}{dt'} dt' = \frac{ec}{2\pi R} \int_0^t U_{loop}(t' dt' = \frac{ec}{2\pi R} \Phi(t) = 27.25 \Phi(t)\,\mathrm{MeV}. \tag{3.5.6}$$

Here $\Phi(t)$ is the flux swing. The radiation limit of 30 MeV is already exceeded for $\Phi(t) > 1.1\,\mathrm{Wb}$. Assuming $U_{loop} = 1\,\mathrm{V}$, which is typical for TEXTOR, the limit is reached after 1.1 s. As TEXTOR RE discharges are several seconds long, the flux swing does not determine the maximum RE energy.
In the current quench phase of disruptions U_{loop} is much higher than in stationary discharges. At TEXTOR the maximum is typically at about 40 V. As U_{loop} changes significantly during the current quench, an average value of 15 V is assumed for a duration of 30 ms. The values are chosen under consideration of a typical TEXTOR disruption like it is shown in figure 3.7.1. The resulting energy limit of $W_{max} \approx 12\,\mathrm{MeV}$ is much lower than the radiation limit and seems to be realistic as can be seen by comparison with the experimental results which will be presented in chapter 5.

3.5.4 Toroidal Magnetic Field Ripple

The toroidal magnetic field of a tokamak is generated by the toroidal field coils. As the number of the coils N is finite, the field shows a modulation going around the torus. During their toroidal turns the REs experience this modulation with the frequency

$$\omega_{ripple} = \frac{nNc}{R}. \tag{3.5.7}$$

Here n denotes the number of the harmonic. According to [56, 57, 98], this ripple frequency can be in resonance with the cyclotron motion of the REs for $\gamma_{res} = eBR/(nNm_ec)$. It follows a resonance energy of $W_{res} = 70/n\,\mathrm{MeV}$ for

TEXTOR where $N = 16$. As the strength of the resonance decreases for higher harmonics, only $n = 1$ and 2 are expected to be of relevance. If a resonance occurs, the REs can be scattered and their pitch angle θ is increased. This leads to enhanced radiation losses and hence a lower radiation limit of the RE energy. In [56] the effect is estimated for the $n = 2$ harmonic at TEXTOR. The effective energy limit is found to occur before W_{res} at $W_{max} = 30\,\mathrm{MeV}$ for $\theta = 0.1$.

3.5.5 Instabilities

Since the electron runaway drags the distribution function to higher velocities, it is disturbed from the Maxwellian shape. The corresponding free energy enables the excitation of various instabilities [99–101]. The plasma electrons can, for example, interact with plasma waves. If the slope of the distribution function fulfils $df(v)/dv > 0$, the electrons can excite waves and if $df(v)/dv < 0$, the waves can be Landau-damped by the electrons. The resonance condition of the electrons reads

$$\omega_k - n\omega_{c,e} = k_{||} v_{||}. \tag{3.5.8}$$

ω_k denotes the wave frequency, n the number of the harmonic and $k_{||}$ the wave number parallel to the magnetic field. The case $n = 0$ is called the Cerenkov resonance. The case $n < 0$ is called the anomalous Doppler resonance. Under this condition parallel electron energy can be transferred to perpendicular energy. $n > 0$ is the normal Doppler resonance where perpendicular energy can be transferred to the parallel direction. The latter effect is not expected for REs as their perpendicular energy is relatively small.
The Parail-Pogutse instability can occur at the anomalous Doppler resonance of the REs [102]. The REs exceeding a critical energy excite waves which are Landau-damped by the thermal electrons at the Cerenkov resonance. If there is a flat top of the distribution function at the thermal resonance, the damping saturates and hence the waves grow unstably. At these waves the REs can get pitch angle scattered. θ, which is usually small due to $v_{||} >> v_{\perp}$, increases and hence the radiation losses increase, too. After the REs have been accelerated above the critical energy again, the process repeats which gives the instability an oscillatory nature. The Parail-Pogutse instability can occur for REs with energies from 0.1 to 1 MeV but it is usually avoided by the choice of the plasma parameters.
In [56] a repetitive, sudden increase of the pitch angle of the REs was observed. This fast pitch angle scattering is explained by means of the Parail-Pogutse instability. It is estimated that the REs with 23 MeV are scattered. An increase of the pitch angle from $\theta = 0.1$ to 0.17 was experimentally observed. This leads to a decrease of the radiation limit to $W_{max} = 20\,\mathrm{MeV}$.

Eventually, the energy of the REs depends on the ratio of the generation mechanisms. According to [16], the secondary electrons are theoretically expected to show a spectrum which is close to exponential, $f(E) \propto \exp(-E/E_0)$ with an average energy between 10 and 15 MeV. New Results about the role

of the secondary generation process are presented in chapter 6. The energy spectrum of the REs is one of the main issues of interest in this thesis and thus the spectral properties of the REs are treated throughout the chapters 5 and 6.

3.6 Diagnostics

As an experimentally working physicist is curious by nature, his ideal diagnostics would measure the complete electron distribution function in space and time. Of course, this is not realistic and hence the information about the REs have to be inferred from the detection of other quantities. Some standard plasma parameters which can be important for RE studies are: the electric field, the electron temperature, ion and electron densities and the effective ion charge for the RE generation rates and the plasma position, the current density or the plasma current for the determination of the RE orbits. Due to the exceptional properties of the REs some more direct diagnostics are available of which the most important should be briefly discussed. An extensive review of the tokamak diagnostics can be found in [103].

3.6.1 X-rays

The detection of X-rays is a common technique for RE studies [22, 104–106]. Soft X-rays are emitted by the plasma as bremsstrahlung due to electron-electron and more important electron-ion collisions. Hard X-rays are emitted by the plasma and also by electrons striking material surfaces. Thus, hard X-rays can be used as a signal of the REs which are expelled from the plasma. As these X-rays are detected outside of the plasma, the radiation has to pass through wall materials and hence for quantitative measurements a scaling of the X-ray quanta with the electron energy has to be taken into account. In [107] a probe was inserted into the plasma to enhance the yield of X-rays due to the impact of REs. High excitation lines like the K- and L-lines of heavy impurity ions can also be used to study REs. For example, detecting the intensity of the K_α-line of krypton, which had been added to a discharge, was used to determine the RE component. The treshold of this line is at 15 keV.
Nonrelativistic electrons emit the maximum intensity of their bremsstrahlung perpendicular to their velocity vector. The bremsstrahlung of relativistic electrons shows a pronounced forward peaking with the half width of the angle between the particle velocity vector and the wave vector of the radiation $\theta_x \approx \pm 0.5 m_e c^2 / W_{RE}$.

3.6.2 Electron Cyclotron Emission

ECE is the electromagnetic radiation which electrons emit due to their cyclotron motion around the magnetic field lines. In a thermal plasma the emission and absorption of the ECE are in equilibrium. Thus, assuming black body radiation, the ECE can be used to measure the electron temperature. In the presence of REs higher harmonics of the cyclotron frequency are excited, too.

The interplay between the absorption of the ECE by the thermal plasma and the emission by the REs hampers the quantitative evaluation of the radiation signal. Nevertheless, the presence of REs results in an enhancement of the ECE signal which can be useful [108, 109].

3.6.3 Synchrotron Radiation

Synchrotron radiation is the electromagnetic radiation which is emitted by the electrons due to their toroidal trajectories. Superthermal REs modify the spectrum and the intensity of the radiation which is usually seen from a thermal plasma. The uniform circulation of the particles with energies below 1 keV causes the radiation at the cyclotron frequency $\omega_{c,e}$. The higher energetic REs excite various higher harmonics which then carry a considerable fraction of the radiation. In the relativistic limit the radiation at the higher harmonics is broadened and thus the harmonics merge to a continuum described by the Schwinger equation. Similar to the X-rays the synchrotron radiation of the relativistic REs is directed along the velocity vector of the particles. Thus, synchrotron radiation of REs confined in the plasma can be detected by a camera which is sensitive in the infrared range and which looks in the direction tangential to the torus. This technique allows the extraction of information about the generation of REs, their energy by using a set of different filters in front of the camera and the pitch angle [110, 111]. A detailed description of the synchrotron radiation and their detection is given in [56, 57].

3.6.4 Neutrons

High energy REs can cause nuclear reactions which are induced by their bremsstrahlung striking limiter or wall materials. In these reactions protons or neutrons can be produced. Due to their charge neutrality, the neutrons can leave the plasma and hence be detected [104, 112]. The threshold energy of the REs to produce photoneutrons is at about 10 MeV in graphite. The yield of neutrons increases significantly for higher RE energies.
In [113] an electron induced Coulomb dissociation of deuterium is discussed as a source of neutrons. The threshold of the process is at 2.2 MeV. The advantage over the photoneutron detection is that these neutrons can be detected while the REs stay confined within the plasma.

Another technique which delivers information about REs is the detection of laser light which had been Thomson scattered and Doppler shifted on the fast circulating REs.
Although there is a number of RE diagnostics, spectral data are rare and the measurement of a RE spectrum at an instant of time is not possible with the techniques presented above. In addition, the temporal resolution of the diagnostics is often not good enough for the very fast RE events in tokamak disruptions. It is the ansatz of the Institut für Laser- und Plasmaphysik to overcome these limitations by developing specialised probes for the detection of the REs at the

plasma edge. As will be shown in chapter 4, these probes enable the measurement of spectral and temporal information which has not been available before and thus new insights into the physics of the REs are achieved in the chapters 5 and 6.

3.7 Operational Regimes

During the long history of RE studies the generation of relativistic electrons has been observed in serveral operational regimes of tokamaks. A short overview is given below.

3.7.1 Tokamak Start up

In the first 200 to 400 μs of a tokamak discharge, during the electrical breakdown, REs can be generated across the whole vessel volume. The runaway process is believed to determine the breakdown dynamics and the early influx of impurities into the plasma in a substantial manner.
When the plasma is being formed, the discharge channel is smaller than the vessel. It gradually becomes hotter and expands. While doing so, impurities are ionised and trapped. If the density is high enough, this leads to an additional radiative cooling of the plasma. If the density is too low for this effect to be significant, the increase of the resistivity due to the larger collision cross sections of the impurities dominates. Both effects tend to enhance the generation of REs. The underlying cause is the enhanced loop voltage in the developing discharge from about 0.5 to 15 ms.

3.7.2 Runaway Beam Regime

This regime is characterised by a low density and a high impurity content. A large fraction of REs can be produced at the beginning of the discharge and this population can carry most of the plasma current.

3.7.3 Slide away Regime

Plasmas which have a low density and a low loop voltage can go into the slide away regime. The formation of this regime is explained by means of the Parail-Pogutse instability [102]. Hereby, the RE energy is limited by the pitch angle scattering. Thus, only low energy REs are observed.

3.7.4 Stationary Runaway Regime

In steady state discharges with low enough densities REs can be produced continuously in the hot, central part of the plasma. At TEXTOR stationary RE discharges are characterised by an electron density of about $n_e \propto 0.6 \cdot 10^{19}\,\mathrm{m}^{-3}$ and ohmic heating only. A freshly, by boronisation conditioned wall favoures the generation of REs with energies up to 30 MeV additionally. The well defined and

well reproducable regime and the reliable RE generation make the low density discharges at TEXTOR a regime very convenient for RE studies.
In the early days of RE studies, when the plasma confinement used to be much worse than today, the possibility of stationary discharges in which the current is carried by the well confined REs was studied. But in order to achieve high fusion yields, high electron densities are desired. At these high densities the electric field which drives the ohmic discharges is too small to cause a substantial RE generation.

3.7.5 Disruptions

In today's tokamaks REs are mainly studied to prevent or mitigate their generation during disruptions where they attain the highest energies and consequently present a severe thread for the integrity of the tokamak. In fact, REs are one of the most serious concerns about disruptions in ITER. The conversion of up to 70 % of the presdisruptive plasma current into a RE current is predicted to lead to the generation of a RE energy content of about 50 MJ [21]. Each of the REs can carry tens of MeV. Due to the small strike areas in the range of tens of cm^2, they can cause local energy depositions enough to melt or ablate the ITER wall materials. The penetration depths of tens of cm in beryllium and graphite are especially dangerous for underlying cooling structures [20]. Thus, REs can considerably reduce the lifetimes of the PFCs or even cause material failures which call for maintenance. REs are a serious concern for the integrity of ITER and other reactor sized tokamaks and the importance to understand the physics of the REs in disruptions including the RE generation, loss and wall interactions is evident.
Figure 3.7.1 displays the temporal evolution of several signals measured during a typical disruption with REs induced by the injection of argon into a purely ohmic discharge of TEXTOR. The thermal quench phase is outlined by a dashed, red box. It includes the negative spike in the loop voltage, seen in figure 3.7.1(a), and a sudden drop of the ECE signal in figure 3.7.1(b). At this stage the predisruptive, magnetic topology and hence the confinement is lost. The thermal energy of the plasma and also the REs which were generated prior to the disruption are expelled to the PFCs. Hence, the plasma becomes cold and the resistivity and the loop voltage rise which leads to a large electric field. During the current quench phase, which is indicated in the figure by a dashed, blue box, the magnetic topology is temporally rehealed. The electric field enables the acceleration of electrons into the runaway regime. The buildup of a RE population is observed via the enhancement of the ECE signal in the cold plasma. The RE current channel is believed to be centrally peaked and smaller than the predisruptive plasma column. When the plasma current, shown in figure 3.7.1(c), starts to decay exponentially fast, this is retarded by the formation of a RE plateau current. Finally, the loss of the REs is triggered and the RE current decays in one step or subsequently showing smaller RE plateaus as in figure 3.7.1(c). The loss of the REs causes an increase of the signal of a neutron detector positioned outside of the TEXTOR vessel. The signal seen in

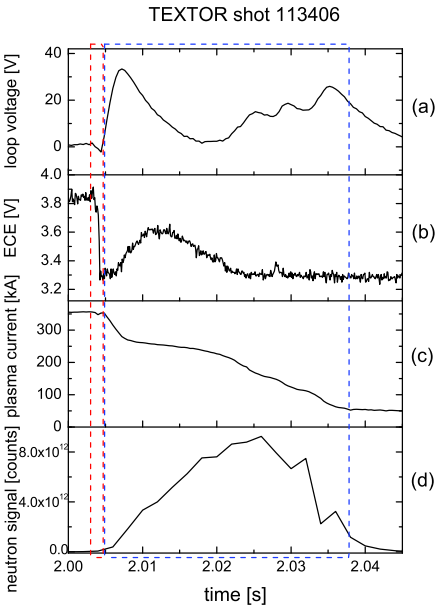

Figure 3.7.1: Temporal evolution of signals measured during a disruption with RE generation at TEXTOR: (a) the loop voltage, (b) the ECE, (c) the plasma current and (d) the neutron signal; the red, dashed box outlines the thermal quench and the blue, dashed box the current quench phase

figure 3.7.1(d) is already saturated when the fast decay of the RE plateau starts. Better measurements of the RE losses were achieved in [22] by monitoring the emission of hard X-rays during disruptions at JET. It was found that the REs get expelled from the plasma in form of repetitive events which are very short in time. The temporal resolution of the measurement was not high enough to measure the properties of the RE bursts having durations in the ms regime.
Thus, there are several substantial open questions about the physics of the REs in disruptions. The loss mechanism which triggers the RE bursts, their temporal properties and the energy spectra of the REs in the bursts are unknown. Even the total RE energy in disruptions has never been measured although it was often predicted by simulations. Deriving from this, also the conversion efficiency of the predisruptive, magnetic energy into a RE energy has not been measured. These issues are studied in chapter 5 of this thesis. The diagnostics used to carry out the corresponding measurements are introduced in chapter 4. The energy loading of the REs onto the first wall is a crucial concern which depends on the size of the strike area. This size is detemined by the properties of the RE beam, i.e. the radial decay length of the REs. The latter is experimentally studied in chapter 5.

3.7.6 Fast Plasma Shutdown

Methods to shut down the plasma power and current have to be available for the operation of a tokamak. They may, for example, be used if a loss of the coolant flow is recognised, safety related license requirements call for it, the plasma is about to leave the operational parameter region, a pending disruption is detected or the plasma has to be kept from touching the wall. The methods currently being studied involve the injection of low atomic number impurites in form of gas, pellets [51] or liquid jets. Such a fast shutdown of the plasma current can lead to the genration of REs [114].
During the restart of JET, after the installation of a full beryllium and tungsten wall fast plasma shutdowns became necessary in the discharges 80263 and 80273. The fuelling of the plasma was stopped and due to the new metal wall the density was lowered quickly by the vacuum pumps below the RE generation threshold. In consequence, REs striked and damaged a beryllium tile. This current example shows that also regarding to fast plasma shutdown techniques the generation of REs has to be considered.

3.8 Mitigation

All the methods of RE mitigation presented below have to be seen in view of tokamak disruptions. This means they will be applied if preventing a disruption has already failed and the violent termination of the discharge has become unavoidable anyway. On a genaral level two strategies of RE mitigation can be considered: the direct way allows to completely prevent the generation of REs, the indirect way has to be used if a population of REs already exists. Increasing the prompt losses can prevent the growth of the population and the acceleration of the REs to higher and hence more harmful energies.
Directly preventing the generation of REs must include the suppression of the primary and the secondary mechanisms. The Dreicer effect scales exponentially with $\epsilon = E/E_{crit}$ and thus is prevented for small values of the parameter which can be achieved by increasing the electron density n_e. Suppressing the avalanching process calls for much higher densities [21, 41, 42, 115]. In the case of ITER $n_e \propto 10^{22}\,\mathrm{m}^{-3}$ must be achieved which means a density about 100 times the flat top value. According to [115], this requires the injection of 10^{25} atoms and according to [21], the injection of 10^{26} particles into the vacuum vessel. The method can be implemented by massive gas injection (MGI) [41, 42, 116–118], the injection of a single or multiple pellets or liquid jets [119]. Choosing argon as the injected species, this would imply several kg quickly being added to the plasma and presenting a heavy load for the vacuum system. Moreover, the mechanical momentum of the impurity alone could cause damages.
If REs are already present, injecting pellets could induce magnetic fluctuations which enhance the RE transport and hence the losses. In order to implement this method appropriately, the penetration of the pellets into the plasma has to be controlled to ensure the deposition of the material near the integer magnetic surfaces like $q = 1$ and 2. A single, large killer pellet [51, 52, 120] can easily

penetrate to the centre of the plasma but it presents also a source of possible mechanical damages to the first wall as it could go right through the whole plasma volume. This problem is overcome by injecting several smaller pellets after each other in a train or at the same time like from a shot gun. The possibility to induce the magnetic fluctuations by the ultrafast injection of moderate amounts of gas is also being studied [121].
Applying an external magnetic field which is resonant to certain flux surfaces causes a perturbation of the magnetic topology. Magnetic islands are formed and overlapping magnetic island chains cause the formation of ergodic zones in the plasma. Thus, a resonant magnetic perturbation (RMP) [115, 122–125] increases the transport and hence the losses of the REs. The influence of a RMP on the RE transport is studied in chapter 6. A detailed explanation of the transport including its temporal and spectral features is given.
Externally imposing a negative loop voltage is a means of shortening the RE current plateau. The implementation of this method in ITER is a massive engeneering problem due to the limits on the voltage in the poloidal coils. The required power implies a one turn voltage in the coils of more than 1 kV. It remains unclear if high enough voltages can be achieved in ITER. Probably, the applied voltage would have to be comparable to the loop voltage after the thermal quench which would call for an on demand power supply.
The last option of RE mitigation could be a mechanical intervention. Inserting control rods or material jets which catch the REs is considered to protect the wall from the RE impact. The blow off which a high energy laser produces from a sacrificial target could create a protective high density plasma in front of the first wall. The temporal and operational feasibility of these methods is not clear as they are not studied in tokamaks currently.

4 Scientific Instruments

This chapter is laid out to introduce the instruments which are routinely applied throughout the thesis and which are characteristic for the studies performed: the tokamak TEXTOR [126], the valve used to induce the disruptions [127], the Dynamic Ergodic Divertor used in the RE transport studies [128] and the GEANT4 *simulation toolkit [129, 130] which was applied for the development of the runaway probes and the evaluation of the measured data. In addition, the relevant runaway electron diagnostics are discussed in detail: the features of the scintillator probe are given [131], the design and development of the heat load and the calorimeter probe are reported and the schemes of the neutron, the electron cyclotron emission, the soft X-ray and the magnetic measurements used to support the probe data are given. The texts and figures of the sections 4.7 and 4.8 are based on the papers [132] and [133], respectively.*

4.1 TEXTOR

According to the abbreviation, TEXTOR is a Tokamak Experiment for Technology Oriented Research in the field of plasma wall interaction. The scope of the machine includes a detailed analysis of the exchange of particles and energy between the plasma and the wall. This implies studies of the erosion of the wall, the release of particles and the influx of impurities into the plasma core as well as the development of techniques to optimise the wall condition and the plasma boundary. The TEXTOR design features are given in [126] and the references therein from a technical point of view.
TEXTOR is a medium sized tokamak with a moderate magnetic field and a large plasma volume. The major and minor radii of the machine are $R = 1.75\,\mathrm{m}$ and $a = 0.46\,\mathrm{m}$, respectively. According to the design specifications, the maximum plasma current is $I_p = 0.8\,\mathrm{MA}$, the maximum toroidal magnetic field is $B_t = 3\,\mathrm{T}$ and the maximum pulse duration is 10 s. The pulse power of 125 MW is supplied by power stations which are concentrated around the TEXTOR site. Additional characteristics of the machine are a circular plasma cross section and the use of an iron core for the transfomer. TEXTOR features excellent accesses for diagnostics and to domains near the wall. There are several large portholes for, for example, radio frequency antennae, neutral beam injection and pumping. More than 300 portholes provide accesses in tangential and radial directions and contribute to TEXTOR's unique flexibility.
The toroidal shell of the machine is placed on a splittable base plate which can be seperated into halves to move the 200 t of the whole experiment. The welded vacuum vessel consists of four large and four small rigid sections which are made of 25 mm thick stainless steel of the type 1.4311. The rigid sections are connected to each other by eight bellows made of 0.5 mm thick stainless steel 1.4848. The transformer consists of a central leg and six yokes.
In order to guarantee the good access to the machine, a relatively small number of toroidal field coils with a large diameter are installed off axis. The 16 coils

with 20 turns each can carry up to 82 kA and hence produce a magnetic field of up to 3 T at the plasma centre. The coils consist of copper conductors which are cooled by water. The resulting ripple of the magnetic field amounts to less than 1.5 % at the plasma boundary. The poloidal field coils are cooled by water, too. The ohmic heating coil, which is the primary coil of the transfomer, consists of 294 turns and it enables a voltage sweep of 8.8 Vs at a current of ± 36 kA. In addition, TEXTOR is equipped with shaping coils, vertical field coils and position control coils which are used to deflect the RE beam during the disruption experiments presented in this thesis.
The vacuum vessel of the machine can be heated by pumping heat transfer oil through the pipes which are welded to its surface. For studies of the plasma wall interactions a first wall liner is installed with an average distance of 70 mm to the vessel wall. The liner is made of 1 mm thick Inconel which can be heated by driving a direct current through it. Usually, the liner is baked at 300° C but its maximum temperature amounts to 500° C. TEXTOR is equipped with a radio frequency glow discharge system. During the operation at 10^{-3} mbar its four antennae act as anodes while the grounded wall acts as the cathode.
Several different kinds of limiters are used to shape the TEXTOR plasma and

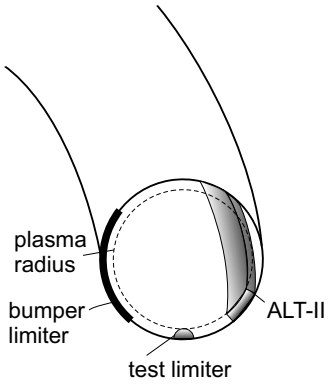

Figure 4.1.1: Schematic cross section through the TEXTOR vessel showing the three main types of limiters: the bumper limiter, the toroidal belt limiter ALT-II and the test limiters

to protect the first wall. The most important ones are indicated schematically in figure 4.1.1. The graphite tiles of a full toroidal bumper limiter cover about one third of the poloidal circumference on the HFS of the torus. They protect the wall against the plasma energy in case of disruptions. The coils of the DED, which are underneath the tiles, make the bumper limiter also a divertor target. At certain toroidal positions test limiters can remotely be moved in on the top, the bottom or on the LFS. These limiteres are used to shape the plasma and for material tests. Additional limiters protect sensitive parts close to the

plasma, e.g. radio frequency antennae. The Advanced Limiter Test-II (ALT-II) is a full toroidal belt limiter which can be pumped. It is mounted at 45° below the equarorial midplane on the LFS. The eight individual blades with each 28 graphite tiles, mounted on an Inconel base plate, are fitted to the poloidal and toroidal shape of the torus.

To heat the plasma auxiliarily, two neutral beam injectors, an ion cyclotron

Neutral Beam Injection	
particle energy	20 to 60 keV
equivalent neutral current	100 A
time on/off	15 s/300 s
beam cross section	400 mm × 320 mm
beam divergence	$< 1°$
working gas	H_2, D_2, He^3, He^4

Table 1: Main characteristics of the neutral beam injection (NBI) system at TEXTOR

resonance heating (ICRH) system and an electron cyclotron resonance heating (ECRH) system (not in operation) with a total power of 9 MW are installed at TEXTOR. The most important specifications of the neutral beam injectors are summarised in table 1.

The main design parameters of TEXTOR can be found in table 2. Some achievments that were realised at TEXTOR and which had a great impact should be mentioned [10]. The machine has been used for extensive studies of the deposition of low atomic number materials on the PFCs. The initial experiments introduced the technique of carbonisation in which layers of carbon are deposited over the entire inner wall during a glow discharge. Making use of carbonisation significantly improved the performance of the machine. The density limit was increased by 50 % and the impurity release from the wall was greatly reduced. In the following the siliconisation and the boronisation techniques, of which the latter is routinely used today, were developed and enabled to reduce the carbon and oxygen contaminations of the plasma. In addition, studies of disruptions, MGI for their mitigation and REs were and are carried out at TEXTOR.

4.2 Disruption Mitigation Valve

A valve which is designed for the fast injection of massive amounts of gas into the tokamak vessel is called a disruption mitigation valve (DMV). At TEXTOR a series of such valves has been developed and tested [127, 134, 135]. The latest version, the DMV-30 [136], was used for the experiments presented in this thesis. Besides the mitigation of the heat loads and forces due to disruptions, the valve enables to study REs.

Figure 4.2.1 shows a schematic cross section of the DMV-30. The release of the gas is triggered by the motion of the piston 4 inside the valve. The motion is initiated by eddy currents and thus no ferromagnetic materials are needed. This

Main TEXTOR Parameters	
plasma major radius R	1.75 m
plasma minor radius a	0.46 m
plasma cross section	circular
plasma volume	$7\,\mathrm{m}^3$
number of toroidal field coils	16
maximum toroidal magnetic field B_t	3 T
maximum plasma current I_p	0.8 MA
maximum pulse length	10 s
installed heating power	9 MW
auxiliary heating systems	NBI, ICRH, ECRH (not in operation)

Table 2: Main design specifications of the TEXTOR tokamak

allows to reliably operate the valve in the high magnetic field environment of a tokamak. The valve has a maximum volume of 1.3 L for the gas which is injected from the top of the TEXTOR vessel. The chamber 1 in figure 4.2.1 contains the gas which is to be injected under a maximum working pressure of $p_w = 40\,\mathrm{bar}$. At full pressure the valve releases slightly more than $40\,\mathrm{bar}\cdot\mathrm{L}$. A closing gas is contained in the chamber 2 under the back pressure p_b. The O-ring 5 at the piston shaft separates the working volume from the closing volume. Another O-ring seals the valve's exit. Both O-rings have inner diameters of 30 mm. Thus, if $p_w = p_b$, the piston is force free. The exit of the valve is leak tight if $p_b \geq 1.5\,\mathrm{bar}$. If the valve is initially not closed, a friction force has to be overcome to move the piston into the closing position. A back pressure of $p_b = 3\,\mathrm{bar}$ is sufficient for this.
In order to open the valve, a power supply (Fug company: HCK 100-200 MOD) discharges a capacitor bank (capacity $C \approx 400\,\mu\mathrm{F}$) at typically $U = 1.7\,\mathrm{kV}$ via a thyristor and activates the pancake coil 3 ($L = 150\,\mu\mathrm{H}$). The coil is isolated from the gas volumes by a casing fully made of stainless steel. Due to safety regulations, the wall thickness of the coil housing amounts to at least 5 mm. The magnetic field of the coil penetrates through the metal housing which, according to the studies in [136], does not effect the performance of the valve. The time varying magnetic field induces eddy currents in the mushroom-shaped back part of the piston. The latter is made of aluminium which makes it light, highly electrical conducting and nonferromagnetic. According to Lenz's rule, the piston is repelled by the coil due to $j \times B$ forces and the valve starts to open within 1 ms. After about 3 ms it is fully open. The DMV-30 releases the gas from chamber 1 through the orifice 6 with a diameter of 28 mm. The gas is guided by a tube to the vacuum vessel of the tokamak. The details of the dynamics of the gas flow in tubes of different lengths and diameters were measured and are reported in [136]. The studies showed that the front of the gas pulse propagates with Mach number 2.5 independent of the diameter of the guiding tube. During the quasi-stationary phase of the gas flow its velocity depends on the tube diameter. After the activation of the piston its back part

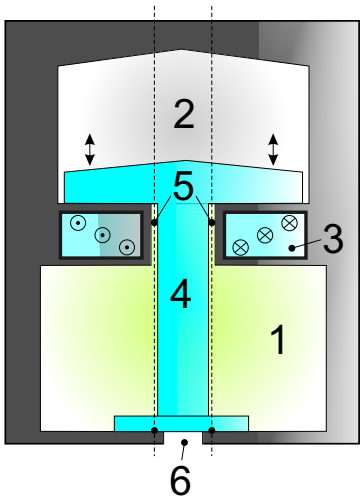

Figure 4.2.1: Schematic cross section of the DMV-30 including the chamber which contains the gas to be injected (1), the back chamber which contains a closing gas (2), a pancake coil (3), an aluminium piston (4), sealing O-rings (5) and the orifice through which the gas flows (6)

compresses the closing gas, which acts as a spring, causing a nearly elastic reflection of the piston. The gas pressure p_b guarantees that the piston reseals the valve under all conditions.
For the mitigation of disruptions in ITER a valve which injects a large number of particles in a short time is needed. The mitigation of REs is even more demanding as discussed in chapter 3. At TEXTOR the DMV is also used to induce disruptions which then can be studied systematically. For this the impurity gas is injected into the stationary phase of purely ohmically heated discharges where it encloses the plasma and gradually penetrates deeper into it. Meanwhile, the gas radiates and thus cools down the plasma. When the cooling front reaches the $q = 2$ surface, the situation becomes unstable and the disruption starts. Using argon as the imputity gas and injecting about 10^{21} atoms at $p_w = 1$ bar leads to disruptions with a reliable generation of REs during the current quench phase. This technique is applied to produce the disruption REs studied in this thesis.

4.3 Dynamic Ergodic Divertor

In chapter 6 the DED [108, 109, 126, 128, 137–143] is used to study the transport of the REs in resonantly perturbed magnetic configurations. The DED is a flexible tool which can influence the transport parameters of the plasma at its edge. Alternatively, static or rotating helical magnetic perturbation fields of different mode patterns are created and thus the magnetic field structure

is ergodised in the edge region. The DED is used to study the effects of the perturbation fields on the heat exhaust, the edge cooling, the impurity screening, the plasma confinement and the stability.
The main part of the DED is a set of 16 helical coils which is mounted on the inboard HFS of the vacuum vessel. The coils have one toroidal turn which is aligned in parallel to the equilibrium magnetic field at the plasma edge. The feeding of the coils is not ideal as it is not symmetric every 22.5° but every 90°. This causes some stray fields which would result in a vertical force on the plasma. The problem is overcome by two additional compensation coils respectively above and below the perturbation coils and in parallel to them. All the coils consist of specially designed, twisted copper conductors which are cooled by a combination of water and helium gas. The 18 coils are protected by the graphite tiles of the bumper limiter which acts as the target for the enhanced heat and particle flows from the plasma due to the divertor action. Additional ceramic tiles thermally insulate the coils from the divertor tiles. This enables to bake the divertor tiles above 300° C. The terminals of the coils are accessible from the outside of the vessel which allows to change the connections and thus the base mode of the perturbation field without breaking the vacuum of TEXTOR.
The base modes m/n are characterised by their poloidal mode numbers m and their toroidal mode numbers n. This classification is chosen because the coil configurations would form these patterns if they were continued around the poloidal circumference of the torus. Three different base modes are possible: for the 12/4 mode all neighbouring coils are operated separately, for the 6/2 mode two neighbouring coils are operated in parallel and for the 3/1 mode four neighbouring coils are operated in parallel. The maximum currents in the individual coils depend on the base mode: 15 kA in 12/4, half the current in 6/2 and quarter of the current in 3/1. This reduction of the currents is compensated by the number of the neighbouring coils which are operated in parallel and thus the perturbation field at the radius of the DED coils is nearly the same for all the modes. With respect to 6/2, the frequencies possible are also lower for the other two modes due to the enhanced conductivities of these configurations. The physical differences of the configurations result from their magnetic mode spectra. In 12/4 about seven dominant modes with $9 < m < 15$ and $n = 4$ occur. In 3/1 three dominant modes are present. These magnetic modes are resonant to the $q = m/n$ magnetic surfaces of the TEXTOR configuration. The region of resonance can be fine tuned radially by matching the pitch of the perturbation current to the magnetic field, e.g. by the choice of the plasma current. The radial penetration of the spectral modes into the plasma can roughly be approximated by r_{eff}^m. Here the effective poloidal mode number is given by $m_{eff} \approx 1.7m$ because the DED coils are laid more compactly on the HFS than on the LFS of the torus. The 12/4 perturbation field decays strongly along the minor radius and only the outer edge of the plasma is affected. The 3/1 field penetrates practically to the core but it also tends to excite a 2/1 tearing mode at rather low DED currents. In DC operation the maximum perturbation is achieved if two neighbouring sets of coils carry the full current in one direction

Main DED Parameters	
number of coils	16 perturbation and 2 compensation
turns per coil	1
conductor	$6 \times 7 \times 7$ twisted copper wires
wire diameter	0.95 mm
current density	$72\,\mathrm{A/mm^2}$
wire insulation	Polyimide 0.05 mm
cooling	helium gas / water
maximum coil temperature	250° C
coil inductance	approximately $7\,\mu$H
coil resistance	approximately 2 mΩ (DC to 1 kHz), approximately 14 mΩ (10 kHz)
time on/off	10 s/360 s
coil current (peak value)	15 kA (DC to 1 kHz), 10.6 kA (1 kHz to 5 kHz), 7.5 kA (5 kHz to 10 kHz)
maximum coil voltage	approximately 2.5 kV
power supply	9×0.9 MW frequency converter units

Table 3: Main DED parameters

and the next set in the opposite direction. This is just the situation which is realised by the base modes. The AC operation is possible with frequencies up to 10 kHz. The phase difference between the neighbouring coils is 90°. All the RE experiments in chapter 6 make use of the DC operation only. The main design characteristics of the DED are summarised in table 3.

4.4 GEANT4 Code

GEANT4 [129, 130] is a simulation toolkit which allows to calculate the propagation of particles through matter. It was designed and developed by an international collaboration formed by physicists and software engineers from a number of cooperating institutes, high energy physics experiments and universities. The basis of the development of GEANT4 was GEANT3 which was refined using software engineering and object oriented technology and implementing the code in C++. The first product has been released in 1998 after initiatives at CERN and KEK. The GEANT4 collaboration has been established in 1999. It takes care of the further development, refinement, maintenance and the user support. A documentation covering the installation, user and reference guides and training kits can be found online [144]. Regular releases of the source code are freely available on the website, too. GEANT4 has applications in many fields, the typical ones being particle and nuclear physics, accelerator design, space engineering and medical physics.
The toolkit enables to create a geometrical model with a possibly large number of components of different shapes and materials. For this purpose it comes with

a library of materials and elements but also the possibility to implement user defined materials. The definition of the primary particles, which should be tracked during their propagation through the materials, can be derived from internal and external sources. The GEANT4 library provides a large set of particles. A comprehensive set of physics models is implemented to describe the interaction of the particles with the matter including electromagnetic, hadronic and optical processes across a wide range of energies from eV to TeV. External magnetic fields can also be included. The geometrical components being declared as the sensitive detectors generate and record the event data (hits) and the detector response (digitisation). The events and particle tracks can be stored. The data can be captured at different levels of detail for the subsequent analysis. It is possible to visualise the trajectories and the detector. The user interacts with the toolkit through different interfaces. The resulting object oriented framework enables a flexible, modular setup and the transparent implementation of the physics. GEANT4 is extensable with new physics and open for customising. The key domains of the toolkit are:

- geometry and materials,
- particle interaction with matter,
- tracking management,
- digitisation and hit management,
- event and track management,
- visualisation and
- the user interfaces.

From these the currently 17 class categories with coherent interfaces are derived. The actual simulation program has to be assembled from the toolkit by the user. In the framework of this thesis GEANT4 is used to simulate the REs in the materials and geometries of the different probes applied for the measurements. The programs include the electromagnetic processes necessary to describe the physics of the electrons as well as an external magnetic field. The passage of the REs through the probe materials is calculated stepwise which includes the step lengths and directions, the energy lost via radiation or deposition in the materials and the creation of daughter particles which are then followed, too. The calculation of the deposition of the particle energy allows to estimate the spectral sensitivity, the heating and the consequent damage of the corresponding probe material. GEANT4 simulations were used in the design and the calibration process of the scintillator probe as well as in the development of the calorimeter probe and the RE heat load probe. GEANT4 was also applied for the evaluation of the probe measurements.

4.5 Reciprocating Mechanism

The REs which are confined inside the plasma are often detected by their synchrotron radiation or by the ECE. After the REs have been expelled from

the plasma the X-rays and the neutrons can be used for RE measurements outside of the tokamak. The spectral information about the REs provided by these diagnostics is limited. In order to measure the REs directly at the plasma edge of TEXTOR, several specialised probes have been developed at the Institut für Laser- und Plasmaphysik of the Heinrich-Heine-Universität Düsseldorf. The probes allow to study, for example, the energy and the spectrum of the REs as well as the temporal properties of the RE losses on a sub-ms timescale. Three different probes were used and two of them were also designed and built for the measurements presented in this thesis.

In order to insert the probes on a ms timescale into the plasma edge, a reciprocating mechanism is applied. It can be equipped with different probe heads of diameters smaller than 80 mm which then can be inserted in the radial direction of the equatorial midplane on the LFS of TEXTOR. The radial position of the measurement can be adjusted with a precision better than 5 mm.

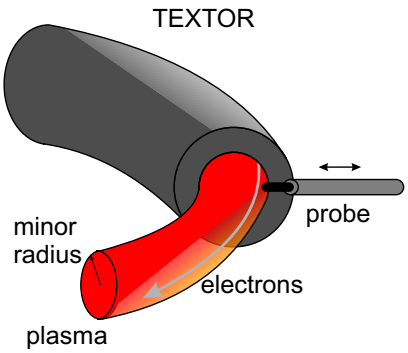

Figure 4.5.1: Scheme of the geometrical setup of the reciprocating mechanism which is used to insert the RE probes into the plasma edge of TEXTOR

4.6 Scintillator Probe

This probe is designed for spectrally and temporally resolved measurements of the REs directly at the plasma edge. Its development is reported in [131, 145–147]. The general setup can be seen in figure 4.6.1. The REs, propagating in a well defined direction around the torus, strike the probe on one side. Consequently, light is produced in a set of scintillating crystals. This light is fed into about 30 m long optical fibres which guide it outside of the TEXTOR hall. Away from the perturbing X-ray radiation and the magnetic fields of the tokamak a set of photomultiplier tubes produces the voltage signals which are fed into the data logger system via BNC-cables. The measured RE signals are spectrally analysed using the GEANT4 code.

The cross sectional scheme of the probe head in figure 4.6.2 illustrates its setup. The inner parts of the probe are shielded against particles and light from the plasma by a 5 mm thick housing made of EK98 fine grain graphite. According

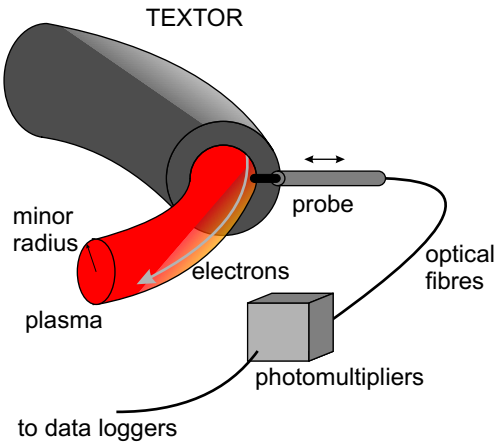

Figure 4.6.1: Scheme showing the general setup of the RE measurements with the scintillator probe at TEXTOR

to GEANT4 simulations, only REs with energies larger than 3 to 4 MeV can propagate through the housing in considerable fractions. These electrons can deposit their energy in the nine $Y_2SiO_5 : Ce$ crystals which are characterised by:

- a light output of 30.000 photons/MeV,
- a melting point at 2470° C,
- a length of 2 mm,
- a front side area of 1 mm^2,
- a decay time of 42 ns and
- the peak of the emitted light at a wavelength of 420 nm.

The energy per electron absorbed in each crystal is a slowly varying function for the electron energies of 1 to 40 MeV. About 700 keV are deposited per electron. The signals produced by electrons are two orders of magnitude higher than those due to γ-radiation. The crystals are shielded by different thicknesses of stainless steel against the direction of the incident electrons and hence detect different energy ranges giving the probe its spectral resolution in the range between 4 MeV and 30 MeV. The steel has the following thicknesses in front of the crystals with the numbers 1 - 0 mm, 2 - 1 mm, 3 - 2 mm, 4 - 2.5 mm, 5 - 3.5 mm, 6 - 4.6 mm, 7 - 5.5 mm, 8 - 7 mm and 9 - 9.5 mm. The Hamamatsu R928 photomultiplier tubes can be equipped with neutral density filters to prevent their saturation. The temporal resolution of the probe measurements is determined by the RC loading time of the setup which can be adjusted using variable resistors. The shortest obtainable loading time is about 30 μs. In addition, two thermocouples in the probe head can be used to monitor the heating of the probe materials on the ion side and on the elecron side, respectively.

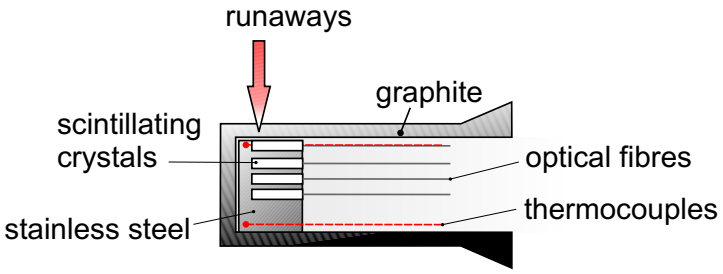

Figure 4.6.2: Cross sectional scheme of the scintillator probe head

The probe was absolutely calibrated using well defined monoenergetic electron beams provided by the electron accelerator ELBE at the Forschungszentrum Dresden Rossendorf. The energy deposition of electron beams in the probe crystals, which is proportional to the generation of the scintillation light, was simulated applying the GEANT4 code. Normalising the experimental and the simulated results to the first crystal, which is shielded only by the graphite housing, shows an agreement within 50 %. This determines the accuracy of the spectral resolution. The influence of the bremsstrahlung and neutrons on the probe signal were found to be negligible.

4.7 Runaway Heat Load Probe

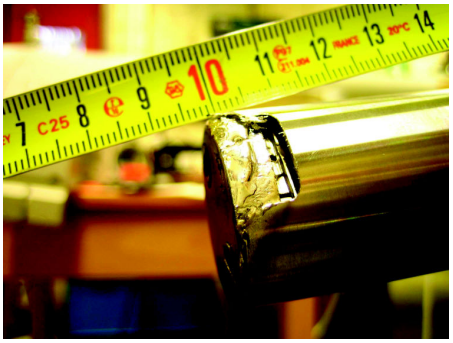

Figure 4.7.1: Electron side of the inner part of the scintillator probe with molten stainless steel

After using the scintillator probe in an experimental campaign of about 30 disruptions, it was removed from TEXTOR. It was found that the graphite housing had a hairline crack but it was still in place and shielded the inner parts of the probe throughout the whole campaign. Removing the housing uncovered a significant damage on the electron side of the inner steel part as can be seen in figure 4.7.1. The REs produced in the disruptions propagated

through the graphite and deposited enough energy to melt the steel. A single shot evaluation, which delivers data about the REs, is not possible with this damage because the scintillator probe has a long history of exposure to RE discharges. The heat load probe is designed to exploit the energy deposition of the REs in materials of different atomic numbers. Comparing the experimental results of the RE impact in the probe material with three-dimensional, GEANT4 code based simulations, single shot data of the energy spectrum and the radial decay length of the REs behind limiting obstacles are obtained.

A schematic cross section of the probe design can be seen in figure 4.7.2.

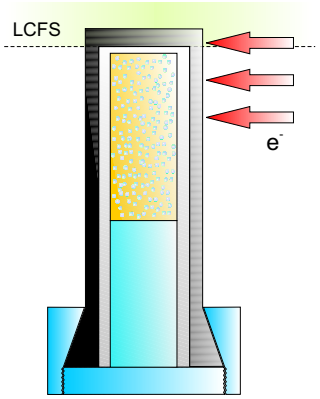

Figure 4.7.2: Schematic cross section of the heat load probe showing the graphite housing, the core made of an epoxy resin with copper particles, the stainless steel mounting and the position of the LCFS in the experiment

The probe has a cylindrical geometry, the outer part being a housing made of 5 mm thick EK98 fine grain graphite. This component shields the inner part against plasma ions and electrons with energies below 3 to 4 MeV. A vacuum gap is necessary to prevent the conduction of the heat to the inner probe part after the impinging particles heated up the housing. Electrons with energies higher than 4 MeV can propagate through the housing into the core of the probe which is the actual detector. It consists of spherical copper particles (maximum diameter 100 µm and 99.7 % purity) in a matrix of an epoxy resin withstanding high temperatures up to about 300° C. The mass fractions of the components are 88 % of copper and 12 % of the epoxy. The mixture was manufactured by blending the copper powder into the resin which then was hardened first at 100° C and finally at 160° C in a vacuum. The electrical insulation property of the material was confirmed by a measurement which proves that the copper spheres, being embedded in the resin, do not touch each other. To reduce the consumption of the resin and the metal powder, not the whole inner cylinder of the probe is made of the detector material, rather the core is fixed with J-B Industro Weld glue to a stainless steel cylinder. The rear end of the housing has a conic shape to avoid the breaking of the graphite due to the large force

the probe experiences along the cylindrical axis during the positioning for the measurement.
The probe head was designed to be used with the reciprocating mechanism at TEXTOR. As the electrons move toroidally in the machine, they strike the probe head from one side in the electron drift direction. Only the high energetic REs enter the core of the probe. Copper has a high atomic number and a high stopping power for electrons [148] and hence the REs deposit their energy mainly in these particles which consequently get heated. As the copper particles are separated from each other in the epoxy resin matrix, the latter obtains high temperatures in the surrounding of the heated copper particles only. Those temperatures locally should be above 300° C and hence the resin suffers visible damages by melting or evaporation. After the impact these damages can be evaluated as a signature of the REs. Provided the temperature at which the given damages occur in the material is known, conclusions about the energy of the REs can be drawn. By the evaluation of the spatial extent of the damaged area information about the radial decay length of the REs can be extracted. This way a single shot disruption evaluation is possible.

4.8 Runaway Calorimeter Probe

The calorimeter probe is designed to get struck by a disruption generated RE beam. The electrons deposit their energy in the probe material and consequently heat it. The resulting temperature profile flattens within several tens of seconds and an equilibrium temperature establishes throughout the material. This value of the temperature can be measured and used to estimate the RE energy in the disruption. The probe must be robust enough to withstand the disruption heat load and the impact of the RE beam. The REs have to get stopped in the probe material without melting it. Hence, a high electron stopping power, a high melting temperature and robustness in the face of thermal shocks are mandatory for the probe material.
In order to find the optimal choice, tests were carried out using the GEANT4 code [129, 144] to simulate the energy deposition of a RE beam in different materials [19]. For the test simulations a RE beam with an exponential energy spectrum (decay parameter $\lambda_E = 0.125\,\mathrm{MeV}^{-1}$) and an exponential radial distribution (decay parameter $\lambda_r = 0.085\,\mathrm{mm}^{-1}$) was chosen based on the results of the former measurements applying the RE heat load probe [132]. A RE beam which carries a current of 100 kA is typical for TEXTOR [115] and it was assumed to fully strike the probe. A toroidal magnetic field of $B_t = 2.4\,\mathrm{T}$ was included. This is particularly important for the scattering of particles and for the opening angle of the daughter particle showers.
Metals with a high atomic number usually have a high electron stopping power. Tungsten additionally has a very high melting temperature above 3400° C and so it was chosen for the first tests. The total linear electron stopping power of tungsten is shown in figure 4.8.1(a) for the relevant electron energies. The other materials which will be discussed are included as well. The linear stop-

ping power gives the energy loss of an electron which propagtes through 1 cm of the material. It is calculated as the product of the mass stopping power and the density of the material. The mass stopping powers were taken from the ESTAR database [148]. The total linear electron stopping power is given in figure 4.8.1(a). It is a sum of the collisional and the radiative contribution. The penetration depth of the REs in tungsten is only a few millimeters which leads to the melting of the material despite its high melting point. The radiative contribution to the total linear electron stopping power of tungsten can be seen in figure 4.8.1(b). This contribution is relatively large as can be seen in figure 4.8.1(c). The ratio of the radiative to the total electron stopping power is shown. The generation of X-rays and γ-radiation is unfavourable because this radiation mainly leaves the material without heating it. Thus, it does not contribute to the measurement of the RE energy. Graphite has a low atomic number. The total and radiative linear electron stopping powers are given in the figures 4.8.1(a) and 4.8.1(b), respectively. Both are substantially smaller than for tungsten. The sublimation temperature of graphite is above 3700° C. The REs easily propagate through several centimeters of graphite without causing a critical heating. Figure 4.8.1(c) shows that the losses due to γ-radiation are substantially smaller than in tungsten. To stop the RE beam, a long slab of graphite would be optimal, but the limitations on the probe's dimensions require a more elaborated design. After the REs have lost a major part of their energy in a slab of graphite, a material with a moderately high atomic number is needed to take the remaining RE energy. Molybdenum seems to be the optimal choice for this. It is nontoxic and it has a melting temperature above 2600° C. The total linear stopping power (figure 4.8.1(a)) is high enough to stop the priorly decelerated REs. The test simulations predict no melting of the molybdenum. The radiative linear stopping power (figure 4.8.1(b)) is quite large compared to graphite. Figure 4.8.1(c) shows the ratio of the radiative to the total stopping power for the relevant electron energies. As the REs are slowed down before they enter the molybdenum, the amount of γ-radiation is tolerable.

The probe design, which resulted from the test simulations, is shown in figure 4.8.2. The probe consists of a sandwich of materials in a stainless steel holder. Two 4 mm thick slabs of a carbon fibre composite (CFC) shield the inner probe parts against the thermal plasma in the directions of the electrons and ions which propagate along the magnetic field lines, respectively. The CFC conveniently takes the thermal loads and it does not break due to the occurring stresses. Thus, the CFC is much more suitable to shield the probe than fine grain graphite which tended to crack when being used for the scintillator and the RE heat load probes. The inner parts of the calorimeter probe, which are designed to stop the REs, do not experience comparable thermal shocks and can be made of an isotropic material. A 35 mm thick slab of EK98 fine grain graphite and a 6 mm thick slab of molybdenum are chosen as a result of the test simulations.

The heat exchange between the slabs and heat losses due to conduction are minimised by vacuum gaps between the CFC, the isotropic graphite and the molybdenum. A slab of an amorphous, high temperature resistant polyimide, called

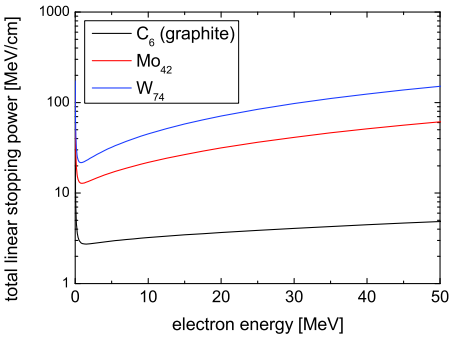

(a) Total linear electron stopping power including the radiative and collisional contributions

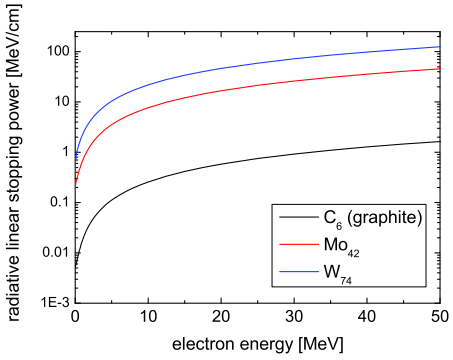

(b) Radiative linear electron stopping power

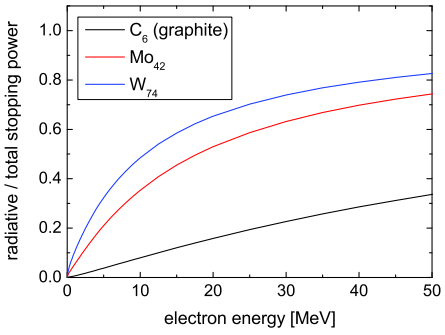

(c) Ratio of radiative to total electron stopping power

Figure 4.8.1: Linear electron stopping powers of graphite, molybdenum and tungsten; calculated as the products of the densities and the mass stopping powers according to the ESTAR database

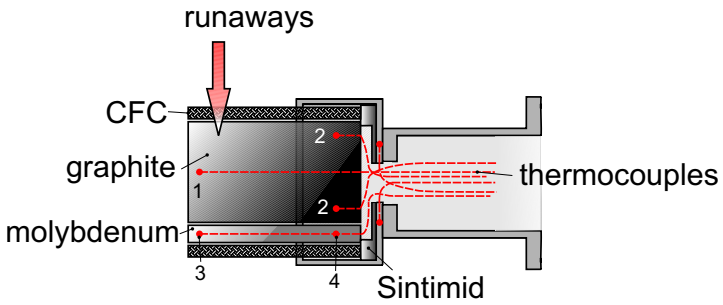

Figure 4.8.2: Scheme of the calorimeter probe. The CFC is used as a shield against the plasma. The heating of a EK98 graphite and a molybdenum slab by the REs is measured by thermocouples in the material, which is thermally insulated against the probe holder by a slab of Sintimid

Sintimid, is used to insulate the probe materials from the stainless steel holder. The coefficient of thermal conductivity of Sintimid is $\lambda = 0.22\,\mathrm{W/(K \cdot m)}$ at 23° C as specified by the manufacturer. The maximum working temperature of Sintimid is 350° C. Besides conduction, thermal radiation cools the probe between the discharges. The losses, which are due to radiation during the discharge and the following few tens of seconds of the temperature measurment, are minor: The radiation losses through the material surfaces which face the plasma are estimated in terms of black body radiation. At a temperature of 1000° C the graphite surface radiates 80 W and the molybdenum surface 14 W. At a temperature of 300° C the graphite radiates 0.6 W through the front surface and the molybdenum radiates 0.1 W. As the measured RE energies are in the kJ range, the losses due to thermal radiation can be neglected. In addition, the evaluation compensates for the losses due to conduction and radiation at the peak temperatures.
The thermocouples which are used to measure the heating of the two sensitive slabs are of the type K. Their measuring tips are positioned 5 mm below the front surfaces which face the plasma and 5 mm away from the opposite surfaces of the slabs. In order to monitor the heating of the holder and the Sintimid, two thermocouples are placed in the Sintimid as well.

A 100 kA RE beam, which is typical for a disruption with REs in TEXTOR [115], was simulated to fully strike the probe applying the GEANT4 code. The spectral and radial distributions of the beam were chosen as described above for the test simulations. The calculations showed that about 20(30) % of the REs with energies of 1(2) MeV can propagate through the CFC. This fraction increases to almost 60 % for the REs which carry 3 MeV. The heating of the isotropic graphite and the molybdenum slabs due to the impact of a RE beam is shown in figure 4.8.3. The vertical axes represent the direction in which the REs propagate into the materials. The horizontal axes give the direction of the radial decay of the RE beam. The colour codes show the heating of the materials due to the RE impact. The initial temperature profiles decrease strongly in the

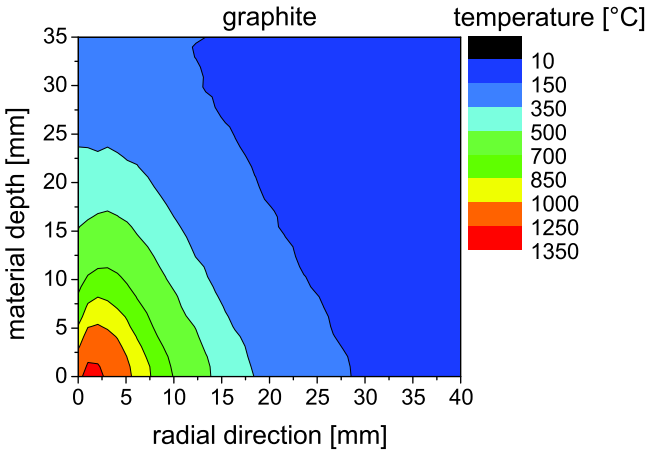

(a) Temperature profile of the EK98 graphite part after the RE impact

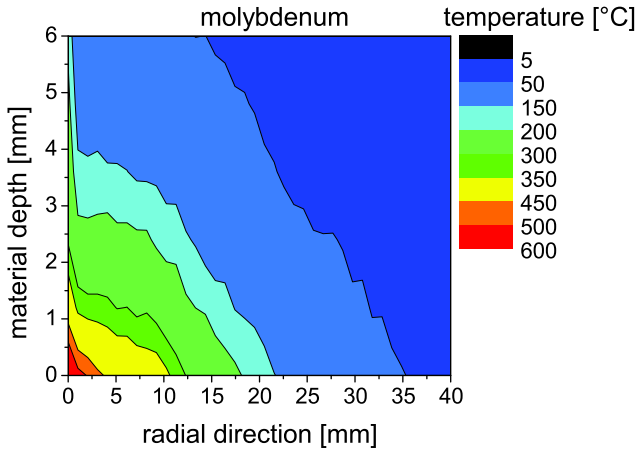

(b) Temperature profile of the molybdenum part after the RE impact

Figure 4.8.3: GEANT4 code simulation of the impact of a RE beam from a single TEXTOR disruption onto the calorimeter probe

radial direction and with the material depth. The exponential radial decay of the RE beam causes the molybdenum to have its maximum of the temperature profile at the front surface as can be seen in figure 4.8.3(b). Figure 4.8.3(a) shows that in the graphite this maximum of the temperature profile is not at the edge but a few mm radially inside. This is an edge layer effect which stems from the scattering of the REs in the CFC in front of the graphite. The effect varies if large changes of the magnetic field B_t are applied. It is shown that the temperatures in the isotropic graphite and the molybdenum due to the impact of the REs from one disruption stay well below the critical values. 67.6 % of the incident RE energy are deposited in the two sensitive slabs. The rest is lost via deposition in the CFC, the generation of γ-radiation, scattering out of the probe or via particles which leave the probe through the backside. Thus, a scaling factor of 1.48 has to be applied to the RE energies which are obtained from the temperature rise in order to estimate the total RE energy in the disruption. The scaling factor depends on the RE energy spectrum used in the simulations. The latter is chosen according to the latest measurements with the heat load probe and the scintillator probe during TEXTOR disruptions [132, 149].

4.9 Runaway Diagnostics used in Support

Besides the probes presented above, neutron and ECE measurements were used to support the RE studies. The data are less quantitative but nevertheless useful to monitor the RE content of the TEXTOR discharges. In order to support the discussion about the RE bursts, measurements of the soft X-rays and of the magnetic perturbations during disruptions were used. The according detectors are routinely available at TEXTOR. A brief overview is given below.

4.9.1 Neutron Detectors

When the REs are expelled from the plasma, they strike the limiter or some other PFC. Due to the sudden deceleration of the electrons, X-rays are emitted. These X-rays can cause photo-nuclear reactions in the plasma facing materials which results in the production of neutrons. The main TEXTOR limiters are made of carbon. The minimum energy the REs must have to cause the generation of neutrons in carbon is about 10 MeV. Thus, an enhancement of the neutron signal indicates the loss of the REs with energies of at least 10 MeV. For the experiments presented in this thesis the yield of neutrons from fusion reactions is negligible in TEXTOR.
Four neutron detectors are positioned outside of the machine in the TEXTOR hall. The numbers 1 and 2 are BF_3 detectors. They are characterised by a better stability than the detectors 3 and 4 which are liquid scintillators surrounded with lead. The scinitillators show the higher count rates. The sensitivities are decreasing from detector 1 to 4. Rates of 10^{11} to 10^{14} neutrons/s can be counted with a time resolution of 2 ms. The precision is better than 10 %. The detectors were calibrated by the activation of indium foils. For the RE studies presented

in the chapters 5 and 6 mainly the liquid scintillators were used as the other detectors tended to be saturated.

4.9.2 Electron Cyclotron Emission Spectrometer

Normally, in tokamak plasmas the absorption and emisison of the ECE are in an equilibrium. Thus, the ECE can be treated as a black body radiation which provides a means to measure the electron temperature T_e. A spectrometer measures the ECE at different frequencies in the GHz range and these correspond to T_e at different radial positions in the plasma.
The presence of REs in the plasma causes a superthermal contribution to the radiation. Due to the relativistic motion of the electrons, higher harmonics of the ECE are generated and form a radiation continuum (synchrotron radiation). This emission of the REs adds to the one of the background plasma. As there are two plasma components with very different energies, the concept of a thermal equilibrium breaks down and the ECE cannot be used to measure the absolute electron temperature. The qualitative interplay of the emission and reabsorption processes has not yet been interpreted successfully .
Nevertheless, the enhancement of the ECE indicates the presence of REs with energies below 3 MeV [115] in TEXTOR. Thus, ECE measurements can qualitatively show the generation of low energy REs inside the plasma. For the measurements reported in this thesis spectrometer channels detecting frequencies from 133 to 148 GHz were used.

4.9.3 Soft X-ray Cameras

The interaction of the REs with the background plasma causes the emission of bremsstrahlung and line radiation from impurities. Hence, an enhancement of the soft X-rays can be observed if REs are present in a tokamak plasma.
At TEXTOR there are four detectors which measure the soft X-rays. These pin diode arrays are all of the same type. Two of the cameras (the numbers 1 and 2) look from the top vertically through the plasma. Each of these two cameras has 20 lines of sight. The other two cameras (the numbers 3 and 4) look from the LFS horizontally through the plasma. They have 16 lines of sight each. The views of the four cameras are shown schematically in a poloidal cross section in figure 4.9.1. The horizontal observation lines are labeled as Mod_L1 to Mod_L38 and the vertical ones as Mod1 to Mod40. As indicated in the figure, the amplitudes of the signals can be adjusted by using different combinations of slits and beryllium filters in front of the detectors. Slits with widths of 1.5 mm, 10 mm, 15 mm, 20 mm and 25 mm are available. The thicknesses of the filters can be chosen from 10 μm, 20 μm, 40 μm, 80 μm and 500 μm. The spatial resolution of the measurements is approximately 3 cm. The differential amplifiers in use have a sampling rate of 200 kHz and they allow signal gains of 1, 10 and 100.
In section 5.2 the soft X-ray signal Mod_L21 is used to support the RE probe measurements. This line of sight is marked by a red arrow in figure 4.9.1. It

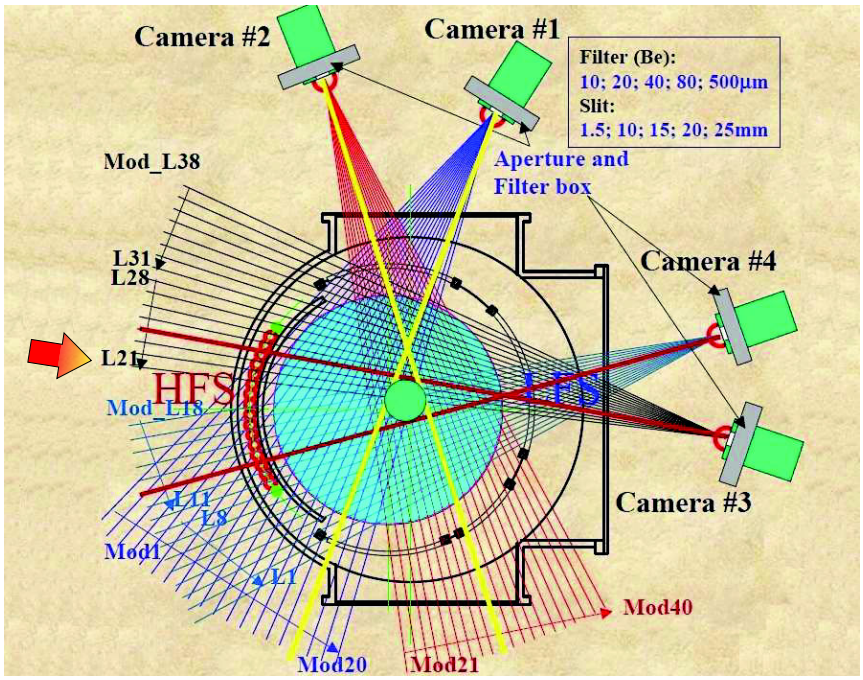

Figure 4.9.1: Scheme of a poloidal cross section of TEXTOR showing the four soft X-ray cameras; the vertically looking cameras 1 and 2 have 20 lines of sight each, the horizontally looking cameras 3 and 4 have 16 lines of sight each; the line Mod_L21 is marked by an arrow as it is used to support the RE measurements (reproduced with kind permission of the IEK-4, Forschungszentrum Jülich GmbH)

belongs to the camera 3 which looks from the LFS horizontally through the plasma centre to the upper half of the bumper limiter.

4.9.4 Mirnov Coils

Pick up coils which measure certain components of the magnetic field of a tokamak are typically called Mirnov coils. At TEXTOR different sets of Mirnov coils are operated. With respect to their location around the torus they can be distinguished into two groups. The first group consists of coils which are distributed around a poloidal cross section of the torus. The coils which are toroidally distributed around the torus at the same poloidal angle form the second group. Independent of their locations there are poloidal and radial Mirnov coils at TEXTOR. The latter are located inside the liner and at equatorial positions on the LFS. These coils measure the radial fluctuations of the magnetic field. The poloidal field coils are installed at the inner side

of the liner and they measure the poloidal perturbations of the magnetic field. In section 5.2 a Mirnov coil signal is used to support the RE studies. The corresponding poloidal field coil (Pi060) is located at 60° above the equatorial midplane on the LFS.

5 Runaway Electrons in Disruptions

This chapter contains novel results about the runaway electrons in tokamak disruptions. The runaway heat load probe was applied to study the spectrum and the radial decay of the runaways in TEXTOR disruptions [132]. The scintillator probe enabled the first temporally and spectrally resolved measurements of the burst-like losses of the runaway electrons during the current quench of tokamak disruptions [149]. The calorimeter probe was used to measure the total energy carried by the runaways during the disruptions [133]. The three main sections are linked to each other. Section 5.2 refines the results of section 5.1. The estimations of the runaway energy in section 5.2 are used to independently check the results of the calorimeter measuremens in section 5.3. All the texts and figures are based on the corresponding papers of the author. Each of the three main sections starts with a brief introduction which gives or repeats the information mandatory to follow the presented studies. For more details of the scientific background please see the review chapter 3 on the runaway electron physics and for more comprehensive descriptions of the applied scientific instruments please see chapter 4. The material analysis presented in the section 5.1.3 was carried out by the group of J. Linke at the IEK-2 of the Forschungszentrum Jülich GmbH. The thermogravimetrical measurements in section 5.1.4 were carried out at the Institut für organische und makromolekulare Chemie of the Heinrich-Heine-Universität Düsseldorf.

5.1 Energy Deposition and Radial Decay of Runaway Electrons

5.1.1 Introduction

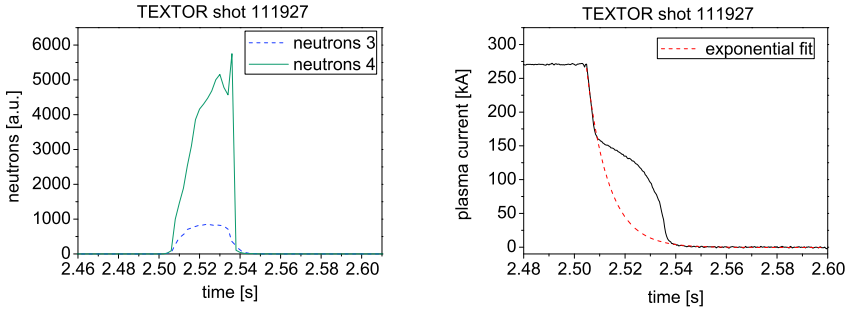

(a) Neutron detector signals

(b) Plasma current with a RE plateau and an exponentially decaying fit

Figure 5.1.1: Signals measured during the TEXTOR disruption to which the heat load probe was applied

As it is practically impossible to use standard electron detectors in the challenging environment of a tokamak, most of the experimental knowledge about the REs relies on other, indirect measuremental techniques using neutron signatures [104, 150], X-rays [22, 104–106], intervening probes to enhance the X-ray yield of the REs [107], synchrotron [110, 111] or electron cyclotron radiation [108, 109]. A great deal of data has been collected this way, but there are still many open questions, e.g. concerning the energy spectrum of the REs. The main measurement device of this section is the heat load probe which was designed to exploit the energy deposition of REs in materials of different atomic numbers. Comparing the experimental results of the RE impact in the probe material with three-dimensional, GEANT4 code based simulations, single shot data of the energy spectrum and the radial decay length of the REs behind limiting obstacles are obtained. The design and the working principle of the probe were explained in the section 4.7. In 5.1.3 and 5.1.4 the evaluation of the RE impact onto the probe is discussed in detail. The corresponding simulations lead to the results given in section 5.1.5. In a first step the following section informs about the probe measurement at TEXTOR.

(a) Heat load probe after the RE impact

(b) Probe core with the RE signature

Figure 5.1.2: Photographs of the heat load probe

5.1.2 Experimental Scenario

The TEXTOR disruption characterised here was induced by the injection of argon gas at 2.5 s after the start of the discharge [115, 116, 127]. For this the DMV-30 worked with a pressure of 1.2 bar and injected 0.02 bar · L. A cooling of the $q = 2$ surface is caused and hence the disruption is started. This procedure

guarantees the generation of a substantial number of REs. The proper radial position of the RE beam was controlled actively during the disruption by the vertical magnetic field. The toroidal magnetic field was 2.4 T and the plasma density before the gas injection was $1.5 \cdot 10^{19}\,\mathrm{m}^{-3}$. The RE content of the disruption is verified by the neutron detectors outside of the machine, the γ-dose outside of the TEXTOR hall and the time evolution of the plasma current. Due to the interaction of the REs with a material, photons are produced. Those photons can undergo photonuclear reactions which result in the generation of neutrons [150]. The minimum energy threshold for the REs to allow the production of neutrons is about 10 MeV. At TEXTOR four neutron detectors with different sensitivities are available. Figure 5.1.1(a) shows the signal of two of the detectors. The γ-dose outside the TEXTOR hall was enhanced to 7.7 µSv. The plasma current showed the typical retardation of the exponential decay in form of a RE plateau during the current quench phase of the disruption which can be seen in figure 5.1.1(b). In order to determine the maximum RE current of 97 kA, an exponential fit, also shown, was substracted from the plasma current. From this the number of the REs was calculated to be $2.3 \cdot 10^{16}$. The heat load probe was inserted 5 mm into the plasma for about 200 ms from 0.1 s before the argon injection. The position of the LCFS with respect to the probe during the experiment is indicated in figure 4.7.2. Due to their high energy, the orbits of the REs are shifted radially outwards from the flux surfaces. After the disruption the probe was taken out and dismounted to allow the evaluation of the RE impact.

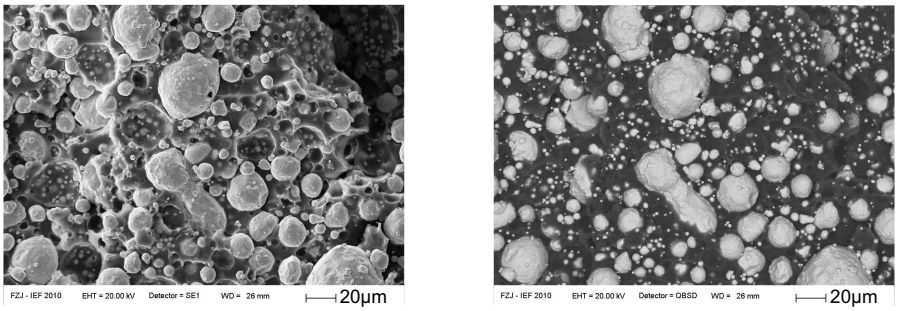

(a) Secondary electron detection mode (b) Backscatterd electron detection mode

Figure 5.1.3: Scanning electron microscope pictures of a part of the surface of the damaged probe core

5.1.3 Evaluation of the Runaway Electron Impact

Figure 5.1.2(b) shows the core of the probe after dismantling the housing. The damage to the copper-epoxy material is located exclusively at the electron side. As the housing shields against low energy electrons, the REs must be the cause for the damage. On the ion side of the probe no visible damage is found.

It has to be mentioned that the graphite housing was also damaged and the top part was destroyed as can be seen in figure 5.1.2(a). Although not appreciated, the probe material lost in the vessel caused no considerable delay of the TEXTOR program as the machine has effective ways of cleaning. The most likely explanation of the sequence of events is given here. The housing was heated significantly by the impinging particles while the REs were passing through the graphite and deposited the main part of their energy in the core, which was heated abruptly, leading to the evaporation of a part of the epoxy resin. Consequently, a gas pressure built up which together with the thermal shock was enough to crack the graphite and push off the top part. As described above, the graphite housing of the scintillator probe was damaged during a series of disruptions, but there was no gas pressure and hence the cracked piece stayed in place. This means that the graphite broke after the RE impact, but during the disruption the core was shielded at all times. The damage to the core showing no discontinuity at the radial position of the breakage of the graphite and going clearly deeper than this edge seems to strengthen this scenario.

To learn more about the nature of the damage and hence the RE impact,

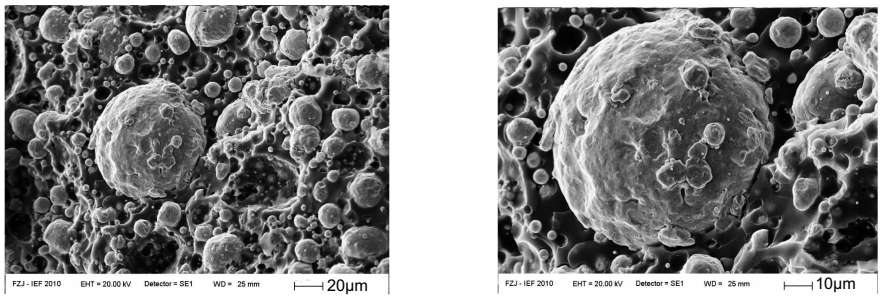

(a) (b)

Figure 5.1.4: Scanning electron microscope pictures of one part of the surface of the damaged probe core in secondary electron detection mode showing different levels of detail

studies with a scanning electron microscope were carried out. For this purpose, the material was sputtered with platin to get a thin coating. Figure 5.1.3 shows pictures of the same surface region in two different detection modi. For figure 5.1.3(a) secondary electrons were detected. Figure 5.1.3(b) results from detecting backscattered electrons. The latter shows the material with a high atomic number brighter and with a low atomic number darker. One can clearly see the approximately spherical copper particles in the matrix of the expoxy resin. The particles are mostly separated from each other which makes the material electrically insulating. Thus, the epoxy resin can be heated locally in the surrounding of the copper particles by heat conduction. In figure 5.1.4 a part of the damaged surface is depicted in two different levels of detail. The secondary electron detection mode is used. Together with figure 5.1.3(a) it proofs that there is no

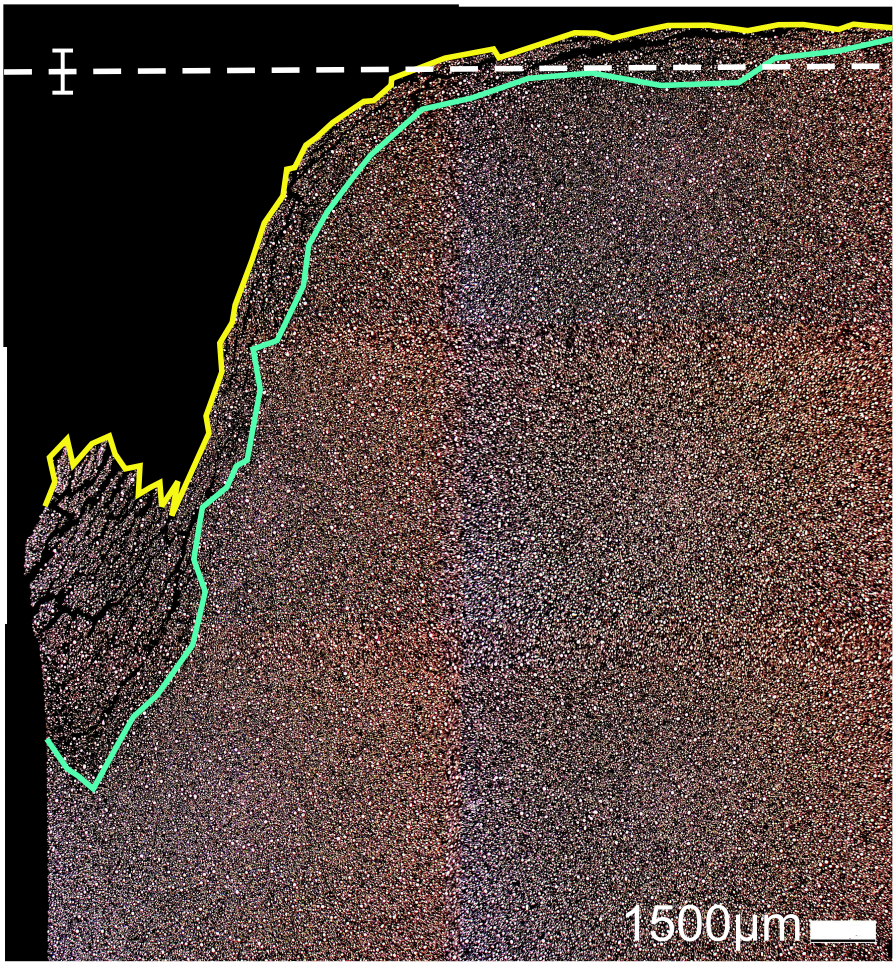

Figure 5.1.5: Cross section of the core of the probe with two added curves outlining the RE damages, cracks and empty holes where copper particles fell out, and a dashed line indicating the approximate position of the graphite edge after breaking

melting of the copper particles which remain in the resin, but there are empty positions where copper particles obviously fell out of the locally destabilised epoxy resin.
To be able to quantify our analysis, metallographical studies were carried out in the next step. Due to the many cracks and lose flakes of the material on the surface, the damaged region was very unstable. So it was necessary to embed the core in an additional epoxy resin which is darker than the high temperature resistant one. The additional resin also has a lower viscosity and was thus able to seal the unstable cracks near the surface. Prepared in this way, the core cylinder was cut in the longitudinal direction right through the damaged area by wire erosion. Carefully exerted, this technique introduces no additional changes due to heat or mechanical stresses to the material. The cutting and subsequent polishing delivered a cross section which was examined with an optical microscope. Figure 5.1.5 shows an overview of the damaged area. Cracks, oriented parallel to the surface, are visible. The dashed line indicates the radial position of the graphite edge after it broke. The larger, damaged piece on the left side was held in place behind the graphite housing during the discharge and thus should not be interpreted as a discontinuity in the damage. In figure 5.1.6 some details are presented with a larger magnification. It has to be mentioned, that the cross sections of the particles shown in the microscope pictures are of course smaller than the size of the full particle spheres by random factors due to the cutting. A crack filled with the darker resin as well as dark spots, being empty positions from which particles have fallen out, can be seen. In order to improve the visibility of the cracks and dark spots, the metallographic sample was coated with a 100 nm thick gold layer (figure 5.1.7). The dark holes appear obviously more often in the damaged region close to the surface up to a specific depths into the material. Deeper inside there are only very few such spots. The damages in form of cracks and dark spots appear to be the signature of the RE energy deposition.

Knowing this, a spatial measurement of the signature had to be done. For

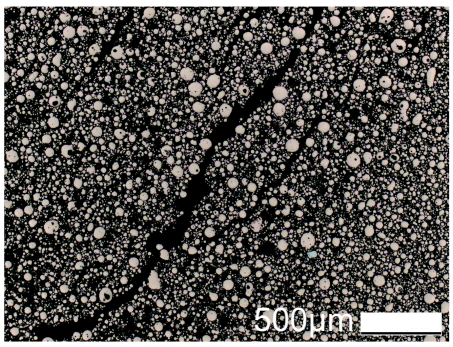

Figure 5.1.6: Optical microscope picture of the cross section of the probe core showing cracks and dark spots as RE damages

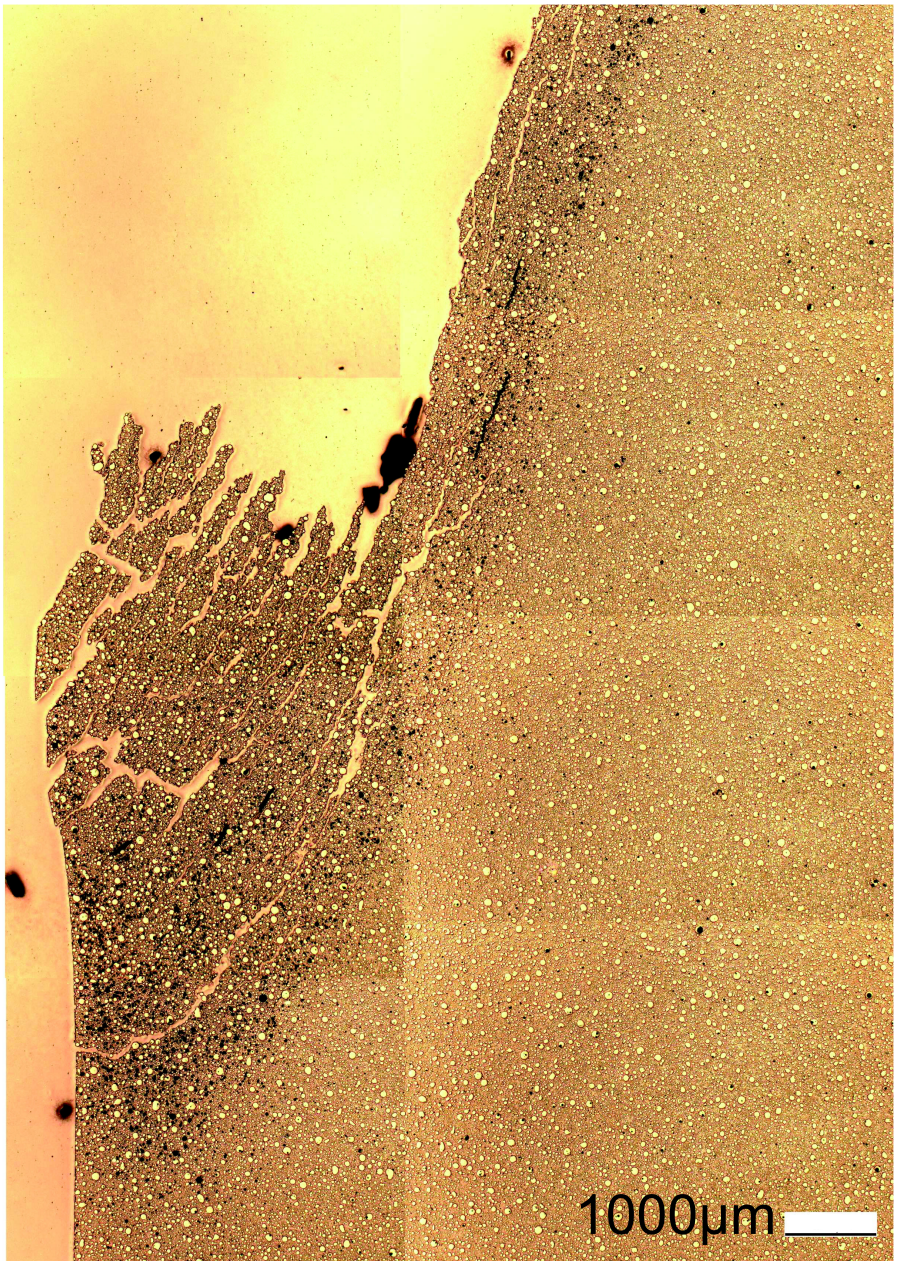

Figure 5.1.7: Optical microscope picture of the cross section of the probe core with a 100 nm thick gold coating showing the cracks and dark spots as the RE damages

figure 5.1.5 two curves were placed on top of the microscope picture, one outlining the remaining probe material and the other curve following the edge of the region which contains the cracks and an enhanced densitiy of the dark spots. Inbetween the two curves nearly all the visible RE damages in the remaining material can be found.

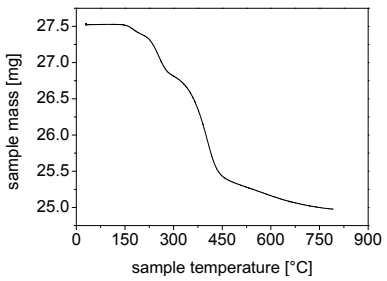

(a) Reduction of the sample mass due to the heating

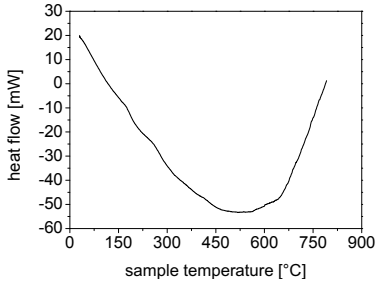

(b) Change of the sample temperature caused by the heat flow into the sample

Figure 5.1.8: Results of the thermogravimetry measurement

5.1.4 Thermogravimetrical Measurements

To allow a comparison of the experimental picture with simulations, it had to be found out how much energy per unit volume is necessary to cause the damages to the probe material. Because the heat capacity of polymeres, like the epoxy resin, changes strongly with their temperature and because of possible chemical reactions of the material components, thermogravimetry was used to determine the amount of energy that goes into the material while it is heated. For the measurement an unused sample of 27.5 mg of the material mixture was examined in a Perkin Elmer STA 6000 simultaneous thermal analyser. The sample was heated from 30° C up to 800° C at a constant rate of 10° C/min. During the heating process the mass of the sample and the heat flow into it were measured. Figure 5.1.8(a) shows that the main loss of the sample mass took place between 300° C and 425° C. Here the epoxy resin was evaporated until only copper was left in the sample. The heat flow, shown in figure 5.1.8(b), going down until about 500° C, means that less and less energy had to be put into the sample to increase the temperature. The reason is the generated heat of reaction. At about the minimum of the curve the epoxy was gone and only copper had to be heated. The heat flow increased again - steeply above the melting point of copper at 660° C. It is remarkable that only the beginning of the curve up to 117.6° C is endothermic, as from this point on the heat flow became negative and there was no more energy necessary to heat the sample further. An integration of the endothermic part of the heat flow over time curve delivers the minimum energy necessary to evoke the damages in the material.

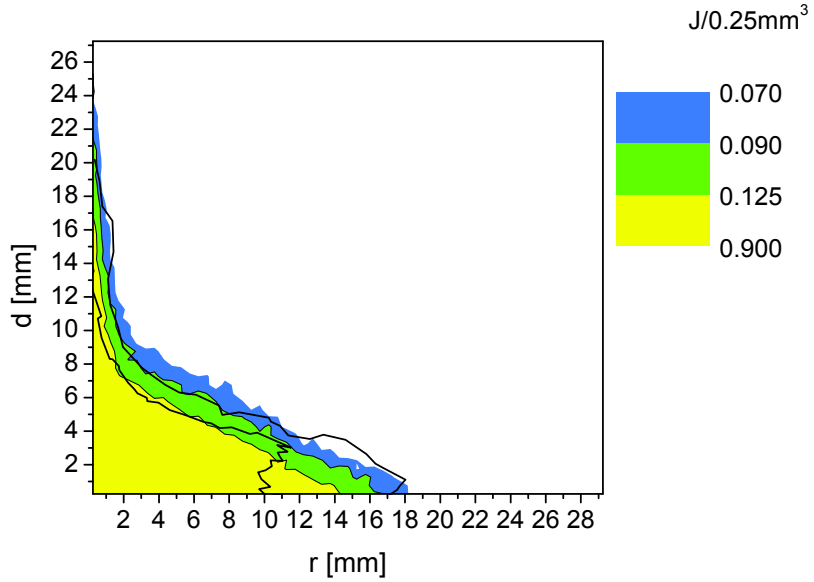

Figure 5.1.9: Comparison of the experimental curves, outlining the RE damages, and the simulation with $n(E) = 0.21\,\mathrm{MeV}^{-1} \cdot \exp(-0.21\,\mathrm{MeV}^{-1} \cdot \mathrm{E})$ and $n(r) = 0.14\,\mathrm{mm}^{-1} \cdot \exp(-0.14\,\mathrm{mm}^{-1} \cdot r)$

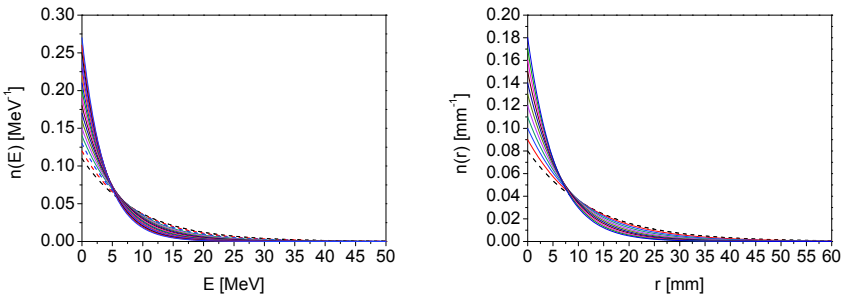

(a) Spectra with $\lambda_E = \{0.11..0.27\}\,\mathrm{MeV}^{-1}$ (b) Radial decay with $\lambda_r = \{0.08..0.18\}\,\mathrm{mm}^{-1}$

Figure 5.1.10: Ranges of distributions

As the temperature of the probe before the RE impact is unknown, the starting point T_0 of the integration is not defined and only unlikely high temperatures can be excluded. Therefore, T_0 is a variable in the comparison of the experiment and the simulations.

5.1.5 GEANT4 Based Monte Carlo Simulations

The simulations of the RE impact onto the probe were carried out with the help of GEANT4. The program includes the three-dimensional probe geometry, the appropriate materials as well as a toroidal magnetic field of 2.4 T. The radial distribution and the energy spectrum of the electron beam incident onto the probe are calculated using random numbers. All so called electromagnetic effects like the photo electric effect, Compton scattering, γ-conversion, bremsstrahlung and ionisation are part of the program. As the input of the simulations an energy spectrum $n(E)$ and a radial distribution $n(r)$ of the electron beam have to be fixed. In the poloidal direction the beam is chosen to be uniformly distributed over the extension of the probe which means the probe gets struck by the full beam. Additionally, it has to be assumed that the energy spectrum of the REs does not depend on the radial position. This assumption will be justified by the measurements in section 5.3. The number of the simulated primary electron beam particles is scaled up to the number of the REs calculated from the RE current to be $2.29 \cdot 10^{16}$. The output of the simulation is a two dimensional matrix of the absolute values of the electron energy deposited per unit volume in the core of the probe. To obtain this, the energy deposition in the core is evaluated on a grid in the radial and toroidal directions with a grid parameter of 0.5 mm. As the experiment shows only a 2D profile of the RE signature, the simulations are integrated over the poloidal direction. This is done only over a 1 mm thick region near the longitudinal cross section of the core cylinder. Consequently, the energy deposition is evaluated for $0.25\,\mathrm{mm}^3$ grid volumes.

An example of a simulation that shows a good agreement with the experiment can be seen in figure 5.1.9. The mean value of five simulations with one million primary electrons each was taken. The figure shows a contour plot of the deposited electron energy per unit volume. The axes, r for the radial direction and d for the toroidal direction or depth in the material, refer only to the probe core without the housing. For comparison with the experimental oberservation the two curves taken from figure 5.1.5 are placed on top. Here the energy spectrum and the radial electron beam distribution are chosen to be exponential, respectively; $n(E) = 0.21\,\mathrm{MeV}^{-1} \cdot \exp(-0.21\,\mathrm{MeV}^{-1} \cdot E)$, $n(r) = 0.14\,\mathrm{mm}^{-1} \cdot \exp(-0.14\,\mathrm{mm}^{-1} \cdot r)$. The energy threshold for the material damages to occur and to give a good correlation of the curves in this example is $0.09\,\mathrm{J}/0.25\,\mathrm{mm}^3$. The corresponding temperature of the probe before the impact is $T_0 = 64°\,\mathrm{C}$.

The input parameters of this example are not exclusively giving a good agreement, rather there is a range of reasonable parameters: $\lambda_E = \{0.11..0.27\}\,\mathrm{MeV}^{-1}$ and $\lambda_r = \{0.08..0.18\}\,\mathrm{mm}^{-1}$. The corresponding e-folding values are $\lambda_E^{-1} =$

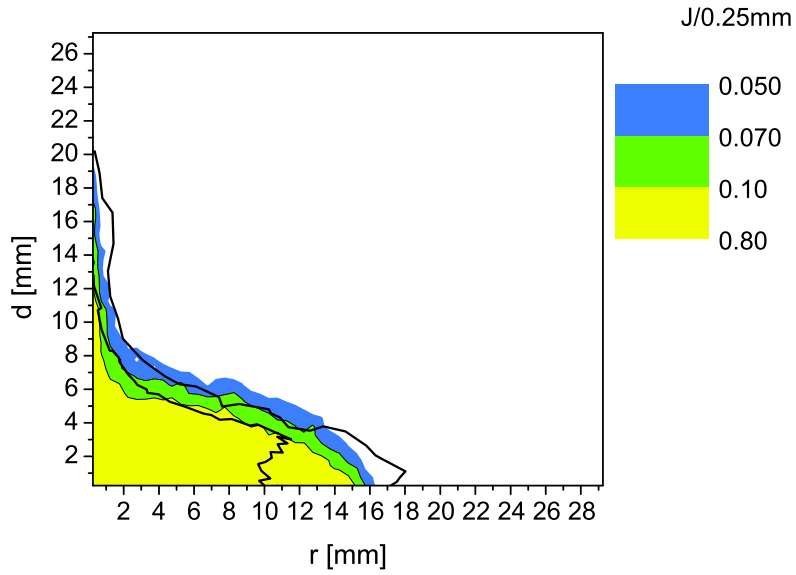

Figure 5.1.11: Comparison of the experimental curves, outlining the RE damages, and the simulation with $n(E) = 0.29\,\mathrm{MeV}^{-1} \cdot \exp(-0.29\,\mathrm{MeV}^{-1} \cdot E)$ and linear radial distribution with root $r_0 = 23\,\mathrm{mm}$

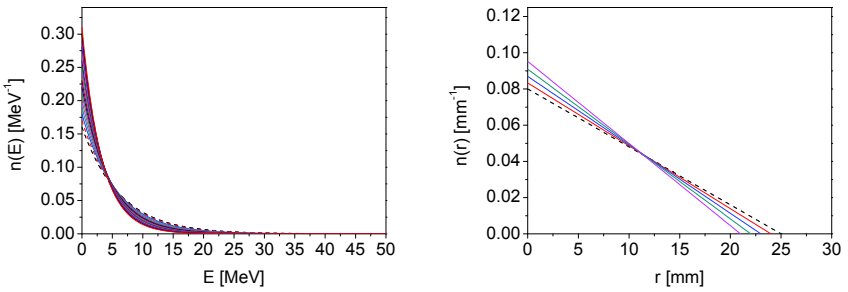

(a) Spectra with $\lambda_E = \{0.16..0.31\}\,\mathrm{MeV}^{-1}$ (b) Radial decay with $r_0 = \{25..21\}\,\mathrm{mm}^{-1}$

Figure 5.1.12: Ranges of distributions

$\{9.1..3.7\}$ MeV and $\lambda_r^{-1} = \{12.5..5.6\}$ mm. The resulting spectra are shown in figure 5.1.10 as well as the radial distributions. The dashed curves denote a still reasonable but worse agreement of the simulation and the experiment. Here the lowest T_0 is 34° C and the results giving $T_0 > 75°$ C are considered as unlikely and are not taken into account. Consequently, the comparison of the simulations and the experiment delivers an upper limit for the choice of the spectrum and hence also for the radial distribution. Going to a lower energy spectrum, the agreement becomes better but T_0 has to increase and too high values have to be left out of the consideration.
A good agreement between the simulation and the experiment can also be achieved by choosing an exponential spectrum and a linear radial electron distribution as figure 5.1.11 proofs. The simulation was done analogously to the previous example. The decay paramter of the spectrum is $\lambda_E = 0.29\,\mathrm{MeV}^{-1}$ and the root of the normalised linear radial distribution is $r_0 = 23$ mm. Furthermore, the probe temperature before the impact has to be $T_0 = 70°$ C.
Again there is a parameter range giving reasonable results: $\lambda_E = \{0.16..0.31\}\,\mathrm{MeV}^{-1}$ (e-foldings at $\lambda_E^{-1} = \{6.25..3.2\}$ MeV) and $r_0 = \{25..21\}$ mm. The distributions are shown in figure 5.1.12. Here the lowest T_0 is 40° C and again results above 75° C are not considered. As in the previous case upper limits and a trend to a better agreement between the experiment and the simulations are observed at the lower energy spectra.
In further studies good results were also obtained for a range of linear energy spectra but they were discarded as unphysical in terms of the RE generation growth rates being exponential [18, 151]. Additionally, former measurements at TEXTOR using the detection of the synchrotron radiation proofed the existence of REs with energies larger than 25 MeV in TEXTOR disruptions [115]. The results of the simulations with linear spectra quickly become negative for roots above 20 MeV.
An additional evaluation of the simulations done so far was carried out by simulating the energy deposition of monoenergetic parts taken from the exponential spectrum. Figure 5.1.13 shows the resulting curves of the deposited energy depending on the depth in the material for the first example from above using $\lambda_E = 0.21\,\mathrm{MeV}^{-1}$ and $\lambda_r = 0.14\,\mathrm{mm}^{-1}$ for the exponential distributions. One million primary electrons were simulated and the deposited energy was integrated over the radial extension of the probe core. Such simulations were also performed for the example with an exponential spectrum and a linear radial distribution shown above. The resulting curves are very similar and thus are not given here. The electrons with energies $E < 4$ MeV are mainly dumped in the graphite housing. The rest is absorbed in the first two millimeters of the core. The electrons with $4\,\mathrm{MeV} \leq E < 8\,\mathrm{MeV}$ are responsible for the damages in the small area of $10\,\mathrm{mm} \leq r \leq 17\,\mathrm{mm}$ and $d < 4$ mm. The spectral part of $8\,\mathrm{MeV} \leq E \leq 16\,\mathrm{MeV}$ is responsible for most of the damages up to 10 mm into the material. Hence, the experimental observation contains mostly information about these electrons. The REs with $E > 16$ MeV have to be few as they would have caused damages deeper in the material which were not observed in the experiment.

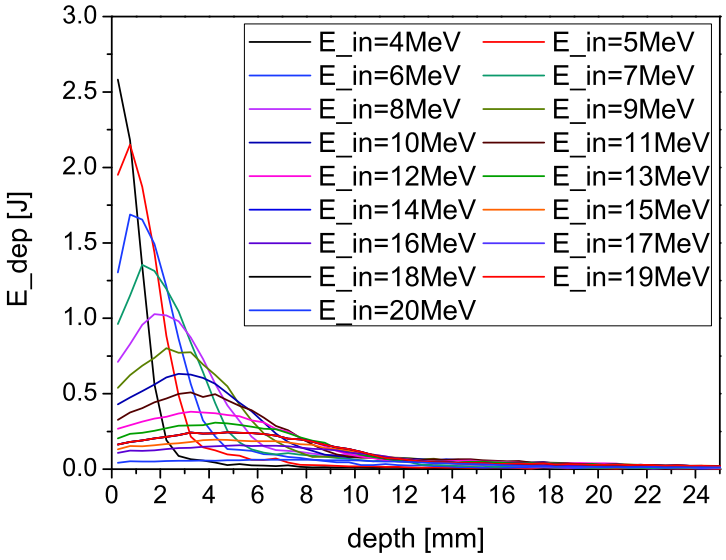

Figure 5.1.13: Results of simulations of the energy deposition by monoenergetic electrons taken from the exponential spectrum $n(E) = 0.21\,\mathrm{MeV}^{-1} \cdot \exp(-0.21\,\mathrm{MeV}^{-1} \cdot E)$ with $n(r) = 0.14\,\mathrm{mm}^{-1} \cdot \exp(-0.14\,\mathrm{mm}^{-1} \cdot r)$

5.1.6 Summary

Using a prototype of a probe at the tokamak plasma edge, it has been shown that in a single shot disruption measurement sufficient RE damages can be obtained to allow the deduction of the energy deposition and the radial decay of the relativistic electrons. The heat load probe exploits the energy deposition of the REs in a material mixture of copper particles embedded in a matrix of epoxy resin. The RE energy causes an observable damage in the probe material. A TEXTOR disruption RE impact was evaluated. To check the RE content of the discharge, neutron and γ−dose detection and the measured time evolution of the plasma current were used. Damages done to the probe this way during a TEXTOR disruption with proven RE content were evaluated. The RE signature was characterised by surface electron and optical microscopy before and after the metallographical preparation of the probe core. The measurement of the spatial extent of the RE signature and thermogravimetry allow a comparison of the results of the experiment with simulations carried out with the GEANT4 code.
A good agreement is found for RE beams with exponential spectra with e-folding energies between about 4 MeV and 9 MeV and the corresponding exponential radial decay with e-folding lengths between 13 mm and 6 mm. Considering RE

beams with exponential spectra and linear radial distributions, the e-folding energies are between 3 MeV and 6 MeV and the roots are between 21 mm and 25 mm, respectively. The simulations with linear energy spectra were discarded as unphysical. Additional simulations were carried out in which monoenergetic parts of the exponential spectrum were used for the RE beam. It was shown that the spectral part with RE energies between 8 MeV and 16 MeV caused most of the observed damages. It has to be remarked that the spectral and radial distributions are attained by a measurement only in the probe core. Electrons with energies less than 4 MeV are absorbed mainly in the graphite housing and the experiment does not describe the radial distribution of the REs in the first 6 mm of the probe housing which faces the plasma. Therefore, it cannot be excluded that the REs have a second decay distribution in these first millimeters. It easily can be stated that 30 mm outside the LCFS there are no or almost no REs to be expected.
In the future versions of the probe different materials should be used. Copper can be substituted by the ITER-relevant tungsten. The epoxy resin has to be substituted by another low atomic number material with a suitable melting point to prevent the buildup of a gas pressure due to the evaporation of the resin and hence the destruction of the probe. It is planned to do several single shot measurements with a set of the probe's final version to be able to analyse different disruptions.
The scintillator probe is especially designed for spectral measurements of the REs. The measurements presented in the next section provide an independent check and a means to refine the spectral results of the heat load experiment.

5.2 Temporal and Spectral Evolution of Runaway Electron Bursts

5.2.1 Introduction

The research for effective ways to suppress the generation of REs [40, 44, 53, 115, 152] is hampered by the lack of a complete understanding of the RE evolution during a disruption. X-ray measurements [22, 153] indicate the loss of REs in disruptions in form of pulses shorter than a ms. In this chapter novel results obtained by measurements with the scintillator probe at the plasma edge of TEXTOR are presented. There is only limited spectral information about REs in disruptions in the literature. It stems for example from synchrotron radiation measurements [152] of REs with energies larger than 25 MeV, from the detection of neutrons [104, 112] produced in photonuclear reactions after the deceleration of electrons with energies larger than 10 MeV and from previous probe measurements [145]. The current study contains the first temporally and spectrally resolved observations of the RE bursts and a discussion of the physical loss mechanism responsible for the bursts. The experimental data enable an estimation of the RE energy content of the disruption and hence a discussion of the conversion efficiency of predisruptive, magnetic plasma energy into RE

energy. From the measured RE spectra a conclusion about the radial decay distribution of the REs can be drawn by a comparison with the studies in section 5.1 and [132].

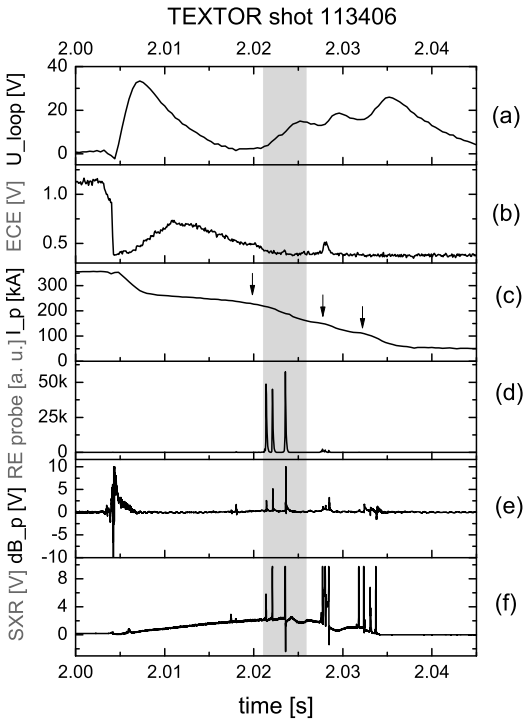

Figure 5.2.1: Temporal evolution of (a) the loop voltage, (b) the ECE, (c) the plasma current with 3 arrows indicating RE plateaus, (d) the probe signal showing REs with energies $> 4\,\mathrm{MeV}$, (e) the signal of a Mirnov coil on the LFS and (f) the soft X-rays for a typical disruption

5.2.2 Experimental Scenario

The disruptions in ohmic discharges with $B_t = 2.4\,\mathrm{T}$, $I_p = 350\,\mathrm{kA}$ and $n_e = 1.5 \cdot 10^{19}\,\mathrm{m}^{-3}$ were induced by the injection of about $0.05\,\mathrm{bar\,L}$ of argon gas which corresponds to about 10^{21} atoms. The DMV-30 was triggered 2 s after the start of the discharge [115]. This procedure guarantees the reliable generation of REs at TEXTOR. The reciprocating mechanism inserted the scintillator probe along the minor radius into the LFS of the machine on a ms timescale. The probe was used to measure the REs directly at the plasma edge. The inner

parts of the probe are shielded against particles and light from the plasma by a 5 mm thick graphite housing. Only REs with energies larger than 4 MeV can propagate through the housing and are detected by the nine scintillating crystals. Due to the energy deposition in the crystals, light is produced which is guided via optical fibres to a set of photomultipliers. Altogether, the diagnostic has a RC loading time of about 30 μs determining the temporal resolution. The crystals are shielded by different thicknesses of stainless steel against the electrons and hence detect different energy ranges giving the probe a spectral resolution as well. In the experimental campaign presented here the probe was inserted 300 ms before the gas injection and it remained at the position until about 250 ms after the injection. The radial position of the measurement was scanned from 48.5 to 47 cm from shot to shot in 5 mm steps. Before the disruptions the LCFS was determined by the toroidal belt limiter, the ALT-II, at the minor radius of 46.3 cm. The exact position of the RE beam during the current quench was not monitored, but the vertical field coils of TEXTOR were used to deflect the beam via feed forward control to the LFS where the probe was inserted.

5.2.3 Measurements of the Runaway Electron Bursts

Figure 5.2.1 displays several temporal signals of a typical disruption of the campaign. The disruption starts with the negative spike in the loop voltage at 2.0044 s, seen in figure 5.2.1(a), followed by a drop of the electron temperature T_e (thermal quench) seen in the ECE in figure 5.2.1(b). The spectrometer measured the emission at frequencies of 133 to 148 GHz which corresponds to a resonance at a major radius of 1.59 m. The signal does not go to zero, rather it drops to about 30 % as the ECE does not provide an absolute measurement of T_e under the given conditions. It gives a measurement of the radiation temperature which is enough to monitor the generation of REs with energies below 3 MeV [115]. The acceleration of plasma electrons into the runaway regime is induced by the steep rise of the loop voltage to almost 40 V. Hence, the ECE shows a gradual increase due to suprathermal synchrotron radiation although the plasma is already cold. After the thermal quench the plasma current starts to decay exponentially (current quench). This is retarded by the practically collisionless REs which form one or more current plateaus. In figure 5.2.1(c) the successive formation of three RE plateaus is indicated by the arrows. When a plateau starts to decay, the REs are expelled from the plasma and seen by the probe at $r = 47.5$ cm as the sharp bursts shown in figure 5.2.1(d). Simultaneously to the RE bursts, the Mirnov coil signal in figure 5.2.1(e) shows a spiked magnetic activity with a temporal resolution of about 5 μs. During the second plateau the ECE shows a peak, which indicates the generation of REs, which are then also detected by the probe. During the third plateau the probe does not measure any RE losses and the ECE is at the level of noise. In contrast, the soft X-ray signal in figure 5.2.1(f) indicates an interaction of REs with the background plasma. Hence, it is not clear if this current is purely thermal or

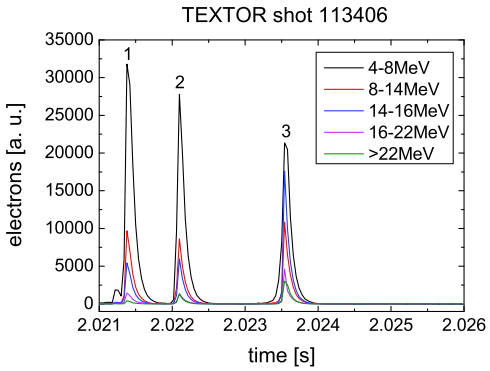

(a) Probe signal over time for different RE energy ranges

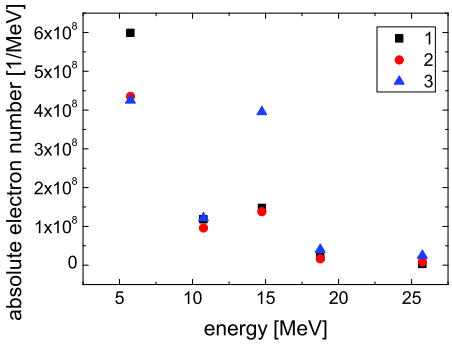

(b) Energy spectra in the 3 bursts

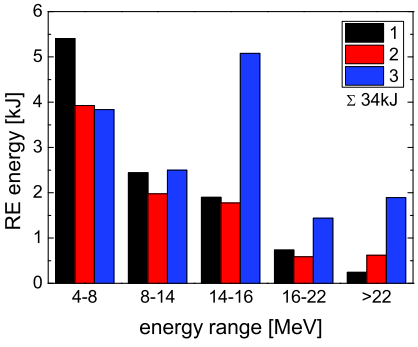

(c) Total RE energy in the 3 bursts

Figure 5.2.2: RE probe measurement at 47.5 cm radius during the same disruption as in figure 5.2.1

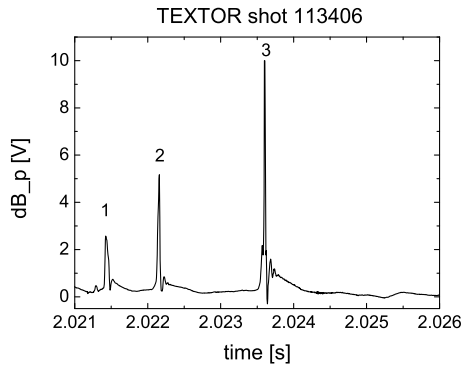

Figure 5.2.3: Poloidal magnetic oscillations measured by a Mirnov coil on the LFS and corresponding to the three RE bursts in figure 5.2.2(a)

also carried by REs. Figure 5.2.2(a) shows the temporal evolution of the RE probe signal in different spectral ranges for the shaded region in figure 5.2.1. Integrating the three peaks of figure 5.2.2(a) respectively and using the absolute calibration of the probe leads to the absolute energy spectra of the measured REs as seen in figure 5.2.2(b). The spectrum of the first peak is exponentially decaying towards higher energies except of an enhancement around 15 MeV. One clearly sees changes of the spectra. From burst 1 to 2 the fraction of REs with energies around 6 MeV decreases and from burst 2 to 3 the fraction around 15 MeV increases. The spectra in figure 5.2.2(b) contain only the number of REs detected by the probe crystals. From the RE current the total number of REs in the disruption and hence a scaling factor for the burst spectra to contain all the REs is calculated. The application of this scaling factor is justified because the spectra are independent of the radial probe position. Thus, if RE bursts strike the probe partly, the undetected parts are assumed to have the same spectra as the detected ones. The spectra of the bursts which completely miss the probe should not differ too much in the contained total energy as the burst to burst changes in the measured spectra indicate. The scaling procedure leads to figure 5.2.2(c). The energy content in kJ is shown for each of the three bursts. Most of the RE energy is contained in the range of particles with 4 to 8 MeV although the energy drops from burst to burst. An increase of the RE energy is seen in the spectral range between 14 and 16 MeV. A substantial part of the energy is carried by these electrons. The RE fraction with energies above 22 MeV contains a few kJ. The total RE energy is about 34 kJ. Figure 5.2.3 shows the poloidal magnetic activity, seen in figure 5.2.1(e), in more detail. The spikes 1 to 3 correspond to the RE bursts 1 to 3 in figure 5.2.2(a). The oscillations grow on a timescale of $\tau_{osc} \approx 40\,\mu$s.

Figure 5.2.4(a) shows the temporal signal of the probe at $r = 47$ cm for another disruption. Before several bursts the buildup of continuous RE losses can be observed in this case. The signal was divided into three parts for which

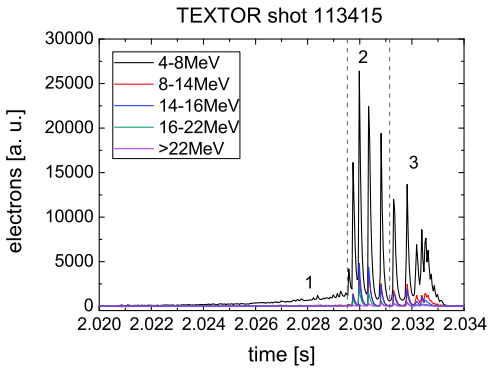

(a) Probe signal over time for different RE energy ranges; the signal is divided into three temporal parts

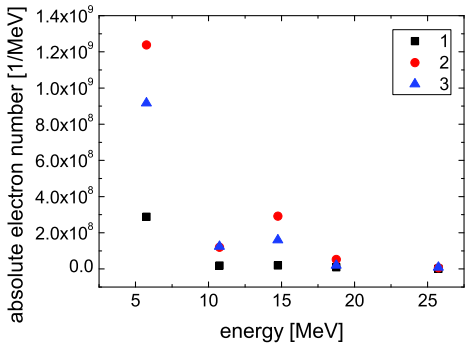

(b) Energy spectra in the three temporal parts

Figure 5.2.4: Results of a RE probe measurement at 47.0 cm radius

the energy spectra of the REs were calculated, respectively. Again the spectra are approximately exponentially decaying with variations in the ranges of 4 to 8 MeV and 14 to 16 MeV. This can be seen in figure 5.2.4(b). In figure 5.2.5 a temporal comparison of the probe signal showing the REs with energies above 4 MeV (b) and the plasma current (a) is presented. From about $t = 2.01$ to 2.03 s the current plateau decreases slowly and continuous electron losses build up. Then a physical mechanism triggers much higher losses leading to a stronger decrease of the RE plateau and the bursts seen in the probe signal. The bursts stop before all the current has decayed. This can be either due to the conversion of the RE current back to a thermal current or the remaining current is carried by REs below the probe's detection threshold of 4 MeV. An arrow in figure 5.2.5(b) indicates a small probe signal during the thermal quench. This is shown enlarged in figure 5.2.5(c). The signal is about 150 times smaller than

the bursts during the current quench and it shows the loss of the REs that were produced prior to the disruption, probably during the startup of the discharge.

Some shots of the campaign were used to apply a resonant magnetic pertur-

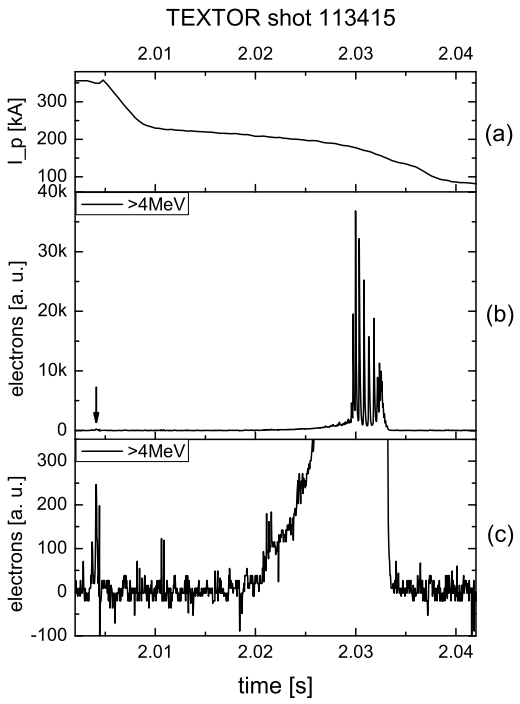

Figure 5.2.5: Temporal evolution of (a) the plasma current, (b) the probe signal for the REs with energies $> 4\,\mathrm{MeV}$ and (c) enlarged, the probe signal during the thermal quench of a disruption; the arrow in (b) marks the small signal of RE losses during the thermal quench

bation to enhance the transport before the buildup of a RE population due to the enhanced loop voltage during the current quench. The DED was used in the 3/1 DC configuration simultaneously to the probe insertion. Figure 5.2.6(a) shows the smooth RE losses induced by a DED current of $2\,\mathrm{kA}$ before the pulsed losses set in. The energy spectra, displayed in figure 5.2.6(b), are similar for both phases. They show the exponential dependence with the enhancement around $15\,\mathrm{MeV}$. A loss mechanism of the REs in the current quench which explains the relatively smooth losses due to the DED, the bursts and also the similar spectra is proposed in the next section.

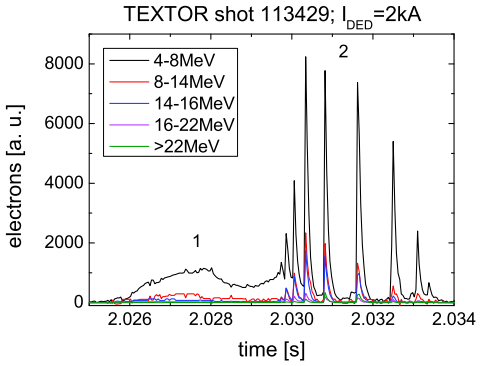

(a) Probe signal over time for different RE energy ranges

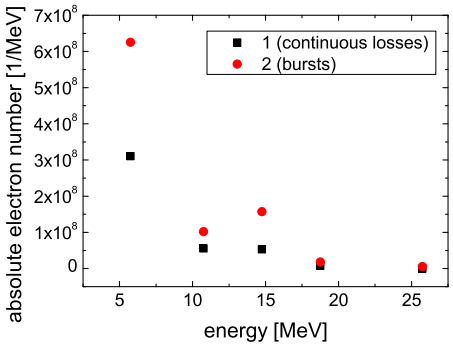

(b) Energy spectra in the regions of continuous RE losses and the bursts

Figure 5.2.6: Results of a RE probe measurement at 47.0 cm radius during a disruption with DED action at $I_{DED} = 2\,\mathrm{kA}$

5.2.4 Physical Discussion of the Results

In the 17 disruptions of the campaign only three to four show a signal in the thermal quench being smaller than the bursts by a factor of 12 to 150. The number of the RE bursts during the current quench ranges from a few distinct bursts like in figure 5.2.1 to numerous bursts on a continuous pedestal like in figure 5.2.4(a). The widths of the bursts are in the range $\tau_{FWHM} = 0.07$ to 0.17 ms. The delays between the bursts are $\tau_d = 0.12$ to 9.3 ms. The whole period of RE losses during the current quench spans a range of $\tau_{loss} = 2$ to 14 ms. The first RE burst is seen 17 to 25 ms after the negative voltage spike. The maximum of the probe signal shows large variations from shot to shot because the RE beam does not always strike the probe fully or even misses it. This indicates a RE beam radius smaller than the predisruptive plasma column which is

in agreement with the increase of the internal inductance in RE plateau plasmas [154]. The figures 5.2.2(b) and 5.2.4(b) show energy spectra and burst to burst changes which are similarly observed throughout the campaign and thus are representative for all the measurements. For comparison, appendix A contains histograms of RE energy spectra measured at four different radial positions. The figures A1(a) to (d) show 46 energy spectra measured during all 17 disruptions of the campaign. In addition, the figures A2 to A5 show supplementary data of the temporal evolution of RE bursts, their energy spectra and the corresponding estimated total RE energies. The typical delay between the RE bursts is 1 ms. A simple estimation of the acceleration of the electrons is done assuming the electrons to travel at the speed of light. The loop voltage is set to 40 V. Accordingly, the REs can gain less than 1 MeV from the electric field between the bursts. Consequently, the burst to burst differences in the spectra cannot be explained by the acceleration of the electrons. No dependence of the RE spectra on the radial probe position is found. The calculated total RE energy ranges from 29 to 46 kJ which agrees very well with the RE calorimeter measurements in section 5.3 and [133]. The predisruptive, magnetic energy can be calculated as $E_{mag} = \frac{1}{2} I_p^2 L_p$ with the inductivity $L_p = \mu_0 R[\ln(8R/a) - 2 + \ell_i/2]$. Using the typical internal inductance $\ell_i = 1.2$ of TEXTOR prior to disruptions, the conversion of magnetic energy into RE energy can be calculated to be between 11 and 17 %. Assuming the energy spectrum in the bursts to be exponential, one obtains an e-folding energy of around 9 MeV. The RE heat load probe experiment in section 5.1 and [132] delivered an exponential radial decay of the RE beam for e-folding energies of 3.7 to 9.1 MeV and a linear radial decay for e-folding energies of 3.2 to 6.25 MeV. Comparing the results of the two experiments provides a strong evidence for an exponential radial distribution of the REs.

Evaluating the temporal properties of the RE bursts and the magnetic oscillations allows a discussion of the physical mechanism which triggers the RE losses. Principally, the magnetic activity, which is measured simultaneously to the RE bursts, can be caused by two kinds of instabilities. Ideal kink instabilities of the RE beam would grow on an Alfvén timescale with $\tau_A = R/(B_t/(\mu_0 n_i m_i)^{1/2}) \approx 1\,\mu$s. This is much faster than the observed half widths of the RE bursts or the growth times τ_{osc} of the magnetic oscillations. The second possiblity, which is theoretically suggested in [82], are resistive tearing modes in the background plasma. Due to the suprathermal nature of the radiation, no temperature measurements are available during the postdisruptive phase. As the main material of TEXTOR is graphite, which radiates strongly during the disruption, one can reasonably assume $T_e \approx 10$ eV during the current quench. Thus, the resistive diffusion time reads $\tau_R = \mu_0 a^2/\eta \approx 2$ ms. This matches well the rearrangement of the current profile during the delay τ_d between the bursts. The growth time of the tearing modes $\gamma^{-1} \approx \tau_R^{3/5} \tau_A^{2/5} \approx 100\,\mu$s is close to τ_{osc} and the half widths of the RE bursts. In a study of the RE transport due to resonant magnetic perturbations in stationary TEXTOR discharges, presented in chapter 6 and [155], similar RE spectra are obtained at the plasma boundary. The presence of

magnetic islands inside the plasma is shown by simulations. Their influence on the transport is found to cause the RE spectra with the bump around 15 MeV at the plasma edge. Because of the lack of a T_e-profile measurement during the current quench, the formation of tearing modes cannot be proven. Thus, tearing and kink modes are the candidates which might trigger the RE bursts.

5.2.5 Summary

In summary, the first temporally and spectrally resolved analysis of the RE bursts in tokamak disruptions was presented. The bursts have temporal widths of 0.07 to 0.17 ms and they follow each other with delays of 0.12 to 9.3 ms. The energy spectra in the bursts are approximately exponentially decaying except of an enhancement at around 15 MeV. The spectra show changes from burst to burst. The radial distribution of the REs is concluded to be exponential. The total RE energy in the disruptions is estimated to be between 29 and 46 kJ leading to a magnetic energy conversion of 11 to 17 %. The total RE energy is studied in more detail using the RE calorimeter probe [133].

5.3 The Energy of Runaway Electrons

5.3.1 Introduction

The field of RE research has both, a long tradition and a great importance. Nevertheless, measurements of the RE energy in tokamak disruptions are rare. Due to the lack of direct measurements, the RE energy content of JET disruptions was inferred from the temperature increase of hot spots [156]. Measurements of the RE energy are mandatory to calculate the conversion effeciency of the magnetic plasma energy into RE energy. This variable often appears as an input parameter for predictive RE models.
Above in section 4.8 the development of a probe designed to withstand tokamak disruptions and to measure the RE energy by calorimetry is presented. The following section contains the description of a measuremental campaign with the RE calorimeter probe at TEXTOR. The experimental results are given and discussed in section 5.3.3. Eventually, in section 5.3.4 the most important achievements are summarised.

5.3.2 Experimental Scenario

The experiments were carried out at the tokamak TEXTOR. The minor radius of 0.46 m was defined by the ALT-II - a toroidal belt limiter which is positioned 45° below the midplane at the LFS. The disruptions were induced by the injection of 0.05 bar L of argon gas into ohmic discharges. Prior to the gas injection the electron density was $2 \cdot 10^{19}\,\mathrm{m}^{-3}$ throughout the campaign.

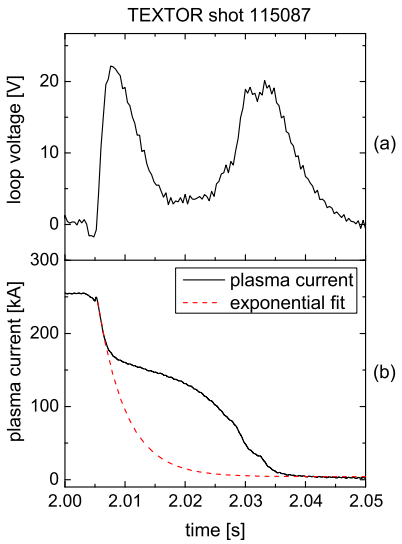

Figure 5.3.1: Temporal evolution of (a) the loop voltage and (b) the plasma current during a typical disruption of the campaign

The DMV-30 was triggered 2 s after the startup [116, 136] of the discharge. The typical temporal evolution of the loop voltage and the plasma current during a disruption of the campaign can be seen in the figures 5.3.1(a) and 5.3.1(b), respectively. The main parameters of this particular discharge are the toroidal magnetic field of $B_t = 2.4\,\mathrm{T}$ and the predisruptive plasma current of about $I_p = 250\,\mathrm{kA}$. The thermal quench of the disruption starts with the negative spike in the loop voltage at about 2.005 s. The following steep increase of the loop voltage enables the acceleration of the plasma electrons into the runaway regime. The almost collisionless REs form a plateau in the plasma current and thus retard the current quench as can be seen in figure 5.3.1(b). The figure also shows an exponentially decaying fit which can be subtracted from the plasma current to calculate the maximum RE current. The injection of argon reliably triggers the generation of REs during the current quench of TEXTOR disruptions [122]. The generation of the RE population was checked by the detection of the suprathermal ECE and neutrons. REs with energies above 10 MeV produce neutrons by photonuclear reactions with the graphite of the PFCs [104, 150]. The vertical field coils of TEXTOR were used to direct the RE beam via feed forward to the LFS of the machine where the probe was inserted radially in the equatorial midplane. The geometry of the setup is shown as a scheme of a poloidal cross section in figure 5.3.2. The radius of the RE beam is assumed to be considerably smaller than the radius of the plasma column prior to the disruption. This assumption is justified by the statistical variations of the RE probe measurements as it is shown in section 5.3.3. About 50 ms prior to

the gas injection the probe was inserted to its measuremental position where it remained for about 200 ms. The radial position of the probe, B_t and the plasma current were separately scanned from shot to shot.

During the disruption shown in figure 5.3.1 the calorimeter probe was inserted

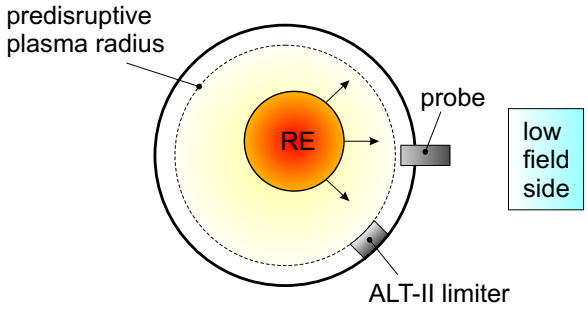

Figure 5.3.2: Scheme of the poloidal cross section of TEXTOR showing the geometry during the probe measurement

to a minor radius of $r_{cal} = 46$ cm. The heating of the isotropic graphite slab of the probe due to the RE impact can be seen in figure 5.3.3(a). The steeply rising temperature curve was measured by the tip of a thermocouple 5 mm below the front surface which faces the plasma. The thermocouples at this position are labeled by 1 in figure 4.8.2. The two slowly rising temperature curves in figure 5.3.3(a) belong to thermocouples radially more outside. They are labeled by 2 in figure 4.8.2. The different curves join after about 60 s at the equilibrium temperature which then can be assumed for the whole slab. Similar results were obtained for the molybdenum slab. Here the equilibrium temperature is reached after about 20 s as shown in figure 5.3.3(b). The dashed lines of best fit in the figures 5.3.3(a) and 5.3.3(b) are used to determine the equilibrium temperature. This procedure compensates for errors due to the heat losses via thermal radiation and heat conduction. In addition, the heat losses are minimised due to the probe's thermal insulation. A side effect of the thermal insulation is a shot to shot increase of the probe temperature. This progressive heating of the probe does not influence the energy deposition of the REs in the materials. Thus, the temperature differences, which are caused by the RE impacts and which determine the estimation of the RE energies, are independent of the absolute probe temperature. The probe materials just have to be kept from reaching their melting temperatures by cool-down phases between the discharges. Figure 5.3.4 shows a photograph of the probe head. It was taken after the experimental campaign. Appendix B contains additional side-view photographs of the probe head taken after the measurements. The isotropic graphite and the CFC which faced the impinging electrons are eroded and the molybdenum is partly molten due to the progressive heating of the probe. These damages are the cause for a difference between the geometrically calculated mass of the materials and the mass measured after the campaign.

This mass difference amounts to about 5 % for the isotropic graphite and to below 1 % for the molybdenum. The significance of these uncertainties can be seen in terms of the error bars in figure 5.3.5(a).
Using the measured temperature differences and the scaling factor, which was calculated in section 4.8, the RE energies in the disruptions are estimated.

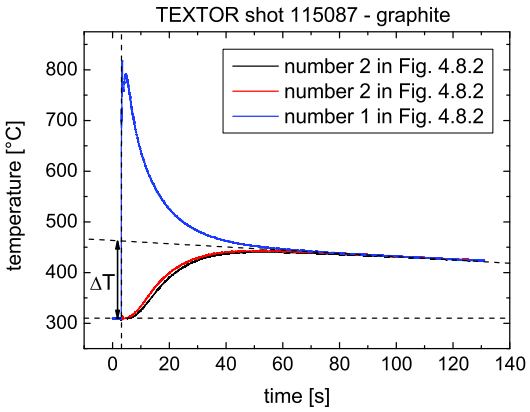

(a) Signals of the thermocouples inside the EK 98 graphite

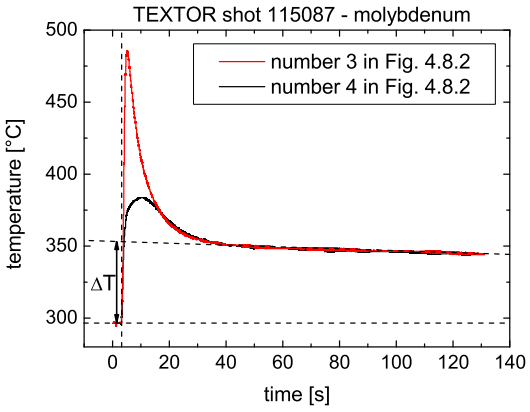

(b) Signals of the thermocouples inside the molybdenum

Figure 5.3.3: Typical calorimetric measurement during a RE impact with added dashed lines used for the estimation of the temperature inrease

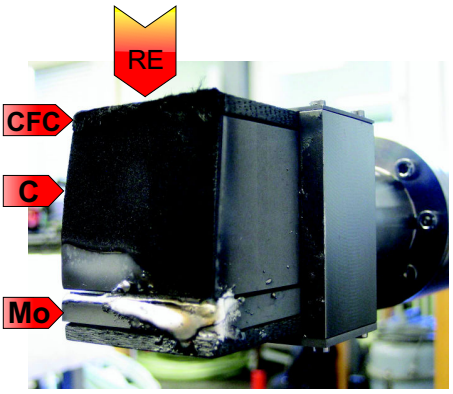

Figure 5.3.4: Photograph of the calorimeter probe after the exposure to a campaign of RE disruptions, the arrows indicate the direction of the REs and the sandwich of materials traversed: a carbon fibre composite (CFC), fine grain graphite (C) and molybdenum (Mo)

5.3.3 Measurements of the Runaway Electron Energy

The experimental results include the RE currents and the RE energies in the disruptions. The RE currents are calculated by subtracting exponentially decaying fits from the RE plateaus. The RE energies are measured by the calorimeter probe. The results of section 5.2 and [149] are used as an independent check of the calorimetry data. The scintillator probe measured RE energy spectra at the plasma edge during TEXTOR disruptions . These disruptions were induced in the same way as described in section 5.3.2. The total numbers of the REs in the disruptions were estimated from the RE currents. The energy spectra were scaled up to contain this number of REs.
There are two ways to evaluate the RE currents and energies. Both should be discussed. The RE currents show large fluctuations from shot to shot as the generation of the REs is sensitive to the exact evolution of the disruption. Most natural disruptions do not show REs at all. At TEXTOR the induced disruptions are used for systematical studies of the physics of the REs. Thus, they favour the generation of REs. Generalising the results, the RE currents should be seen as maximum values. In the following the evaluation according to this interpretation (a) is based on the upper limits of the achieved RE currents. The interpretation (b) applies a statistical standard method. The scatter of the data is reduced by taking the mean of the RE currents for fixed values of the plasma parameters. The RE energies allow an analogue treatment. The large scatter of the calorimetry data points is caused by the RE beam often striking the probe only partially or even missing it. This implies a RE beam which is smaller than the predisruptive plasma column. This assumption is in agreement with the increase of the internal inductance in postdisruptive RE plasmas [154]. The statistical variations cause the calorimeter measurements to underestimate

the RE energy. If the RE beams were fully incident on the probe, they produced data points at an upper limit. The scintillator probe results are independent of this geometrical interpretation (a). Thus, they are less scattered and they are close to the upper limit. In analogy to the RE currents the evaluation (b) reduces the data scatter by taking the mean of the RE energies. This statistical evaluation ignores the geometrical interpretation and leads to different absolute values.

Figure 5.3.5 shows the RE energies which were measured by the calorimeter probe at the radial position $r_{cal} = 46\,\mathrm{cm}$ during disruptions with $B_t = 2.4\,\mathrm{T}$ and $I_p = 300\,\mathrm{kA}$. The RE energies are shown in dependence of the RE currents. The scintillator results are also included. Figure 5.3.5(a) shows the results according to the geometrical interpretation. The upper limit of the RE energies is indicated by the dashed line. The scintillator probe results are close to this line and support the geometrical interpretation. The mean RE energies according to the statistical interpretation can be seen in figure 5.3.5(b). The relative dependence of the RE energy on the RE current is clearer in this figure. The scintillator results are independent of the geometrical fluctuations and thus their mean values are larger than the mean calorimetry data. Both ways of evaluating the data suggest an approximately linear increase of the RE energy for RE currents above 50 kA. The mean RE current of all the disruptions in figure 5.3.5(a) amounts to about 100 kA. According to the geometrical interpretation, a typical TEXTOR disruption includes a RE energy content of 30 to 35 kJ. The mean RE energy of all the disruptions is $20 \pm 12\,\mathrm{kJ}$. These results have been extrapolated to RE currents of 1 MA typical of disruptions at JET. This allows a comparison with the results presented in the literature [156]. The RE energy content of JET disruptions was inferred from the temperature increase of hot spots. This was done for 17 disruptions and the RE energy was found to vary between 0 and 0.5 MJ. The results show an accumulation of four data points around 0.32 MJ in figure 4 of the reference. The according RE currents are not given in the publication. Rather a typical RE current of 1 MA is stated to contain a RE energy of about 0.5 MJ. The extrapolation of the dashed line in figure 5.3.5(a) to a RE current of 1 MA leads to a RE energy of approximately 0.34 MJ. A linear fit of the calorimeter results in figure 5.3.5(b) leads to about 0.21 MJ of RE energy in a current of 1 MA. Consequently, the comparison supports the geometrical interpretation of the TEXTOR results.

The dependence of the RE energy on the radial position of the calorimeter probe is presented in figure 5.3.6 for $B_t = 2.4\,\mathrm{T}$ and $I_p = 300\,\mathrm{kA}$. The geometrical interpretation is shown in figure 5.3.6(a). A dashed line is included to mark the upper limit of the RE energy. Figure 5.3.6(b) shows the mean values of the RE energy at each radial position. The minimum radius of $r_{cal} = 46\,\mathrm{cm}$ corresponds to the position of the toroidal limiter. For probe positions radially more outside than $r_{cal} = 46.5\,\mathrm{cm}$ the energy decreases 5.3.6(a) linearly or 5.3.6(b) less than linearly. Thus, the fraction of the RE beam which is stopped by the probe decreases on the average. Consequently, the probe measurements are most reliable for $r_{cal} \leq 46.5\,\mathrm{cm}$. Going 2.5 cm away from the plasma edge reduces the RE energy load on the PFCs by a factor of 2.

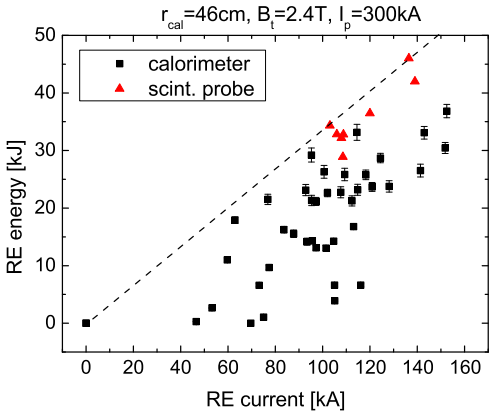

(a) Overview of the measured values and a dashed line which indicates an upper limit according to the geometrical interpretation of the data

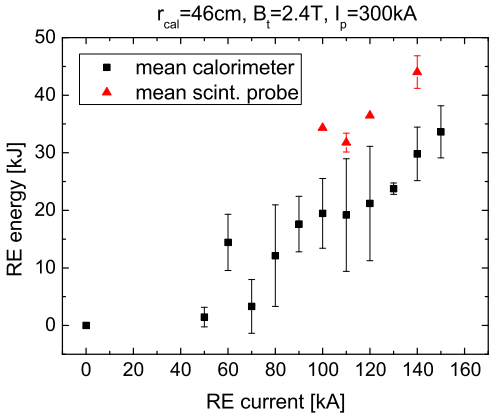

(b) Mean values of the RE energy

Figure 5.3.5: RE energies, measured by the calorimeter probe and resulting from scintillator probe studies, over the RE current

The dependence of the RE current on the toroidal magnetic field is shown in figure 5.3.7 for $I_p = 300\,\mathrm{kA}$. Figure 5.3.7(a) shows all the RE currents. The maximum values are outlined by a dashed line. The mean RE currents are given in figure 5.3.7(b). From both figures it can be concluded that for $B_t \leq 2\,\mathrm{T}$ no REs are produced. Such a RE generation threshold around $B_t \approx 2\,\mathrm{T}$ was observed on several machines. The existence of such a threshold was statistically analysed at JET [157] and a comparison between JET and TEXTOR was drawn [158]. Two physical mechanisms which possibly could cause the treshold were studied theoretically [159]. "The first possible explanation [...] is that the runaway beam excites whistler waves that scatter the electrons in velocity space [...] The second possible explanation is the magnetic field dependence of the criterion for substantial runaway production obtained by calculating how many runaway electrons can be produced before the induced toroidal electric field diffuses out of the plasma" (abstract). Above the threshold the RE current increases approximately linearly with B_t. The slope of the increase is higher in figure 5.3.7(a) than in 5.3.7(b). The RE energies measured for $I_p = 300\,\mathrm{kA}$ at $r_{cal} = 46\,\mathrm{cm}$ are presented over B_t in figure 5.3.8. The geometrical interpretation including an upper limit is given in figure 5.3.8(a) and the mean RE energies are given in figure 5.3.8(b). A similar B_t-dependence as for the RE current applies to the RE energy. This supports the conclusion of a linear dependence of the RE energy on the RE current. Again the slope in figure 5.3.8(a) is steeper than in 5.3.8(b).
The dependence of the RE current on the predisruptive plasma current can be seen in figure 5.3.9 for $B_t = 2.4\,\mathrm{T}$. Again all the RE currents and an upper limit are given in figure 5.3.9(a) and the mean RE currents are given in 5.3.9(b). Deriving from both figures, the RE current increases for $200\,\mathrm{kA} \leq I_p \leq 300\,\mathrm{kA}$. According to figure 5.3.9(b), the RE current seems not to increase above $I_p = 300\,\mathrm{kA}$. Figure 5.3.10 shows the dependence of the RE energy on the predisruptive plasma current. The calorimeter probe measured at $r_{cal} = 46\,\mathrm{cm}$. The scintillator results are included as well. Figure 5.3.10(a) gives the upper limit on the RE energy which results from the geometrical interpretation. Figure 5.3.10(b) shows the mean RE energies. Both figures allow a similar estimate of the I_p-dependence of the RE energy as for the RE current in figure 5.3.9. Taking all the disruptions into account which resulted in a nonzero RE current the mean conversion of the predisruptive plasma current into a RE current is found to be 35 %. The maximum value is 51 %.

The efficiency of the conversion of the predisruptive, magnetic plasma energy into RE energy is calculated. For this the magnetic energy of the plasma prior to the disruption is calculated via $E_{mag} = \frac{1}{2} I_p^2 L_p$. The inductance is $L_p = \mu_0 R(\ln(8R/a) - 2 + \ell_i/2)$. The value of the internal inductance is the only parameter which is not exactly known for the predisruptive plasma but it is typically $\ell_i = 1.2$ at TEXTOR. Deviations from this assumption by ± 1 introduce an error of $\pm 3\,\%$ to the final result. Figure 5.3.9 shows the tendency of the conversion efficiency to decrease with an increasing plasma current for $B_t = 2.4\,\mathrm{T}$. The results according to the geometrical interpretation of the calorimeter probe measurements are given in figure 5.3.11(a). Again the results of the scintillator

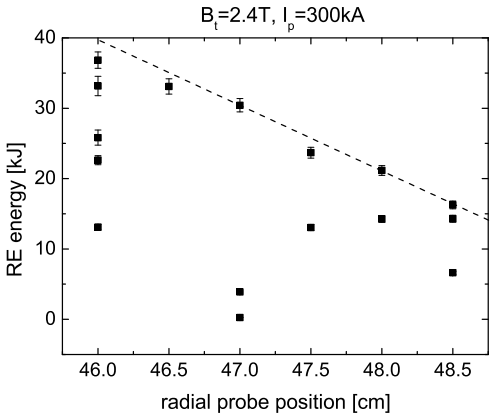

(a) Overview of the measured values and a dashed line which indicates an upper limit according to the geometrical interpretation of the data

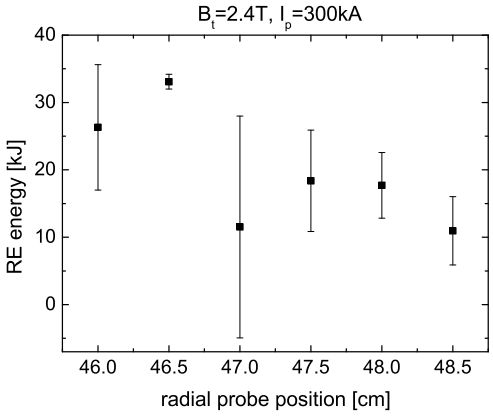

(b) Mean RE energies

Figure 5.3.6: RE energies over the radial position of the calorimeter probe

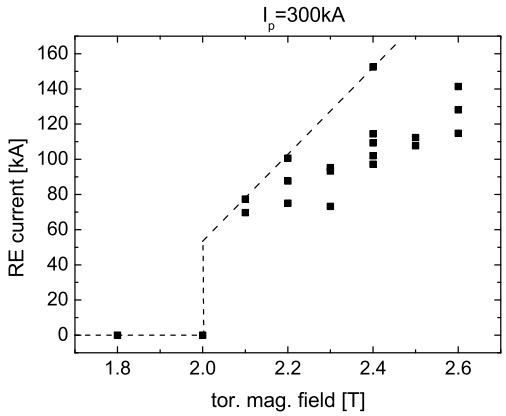

(a) Overview of the measured RE currents and a dashed line which outlines the maximum values

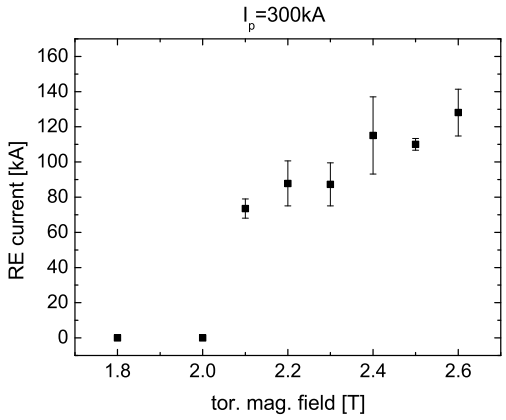

(b) Mean RE currents

Figure 5.3.7: RE currents over the toroidal magnetic field

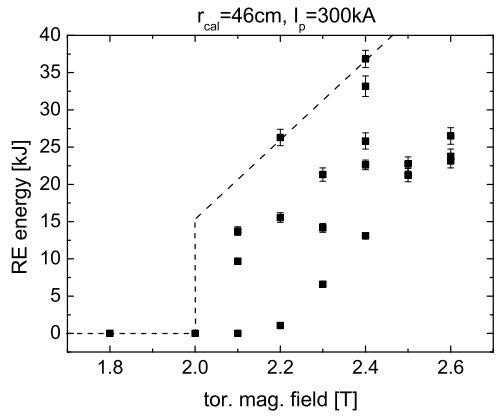

(a) Overview of the measured values and a dashed line which indicates an upper limit according to the geometrical interpretation of the data

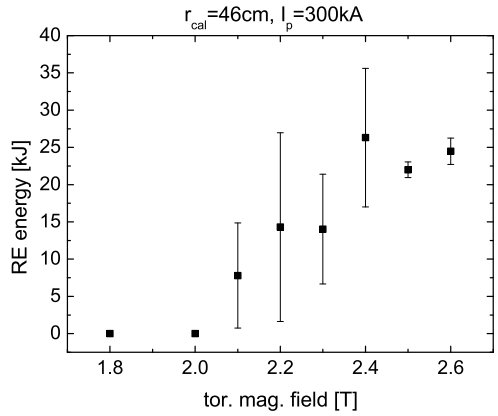

(b) Mean RE energies

Figure 5.3.8: RE energies, measured by the calorimeter probe, over the toroidal magnetic field

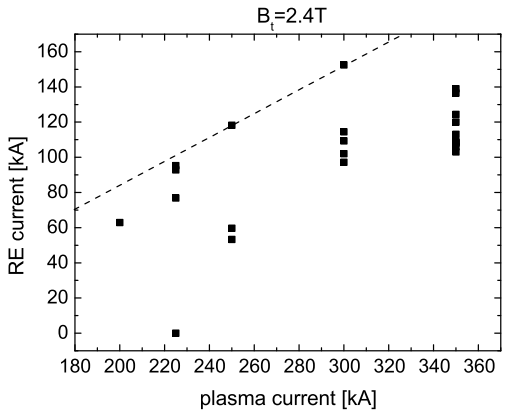

(a) Overview of the measured RE currents and a dashed line which outlines the maximum values

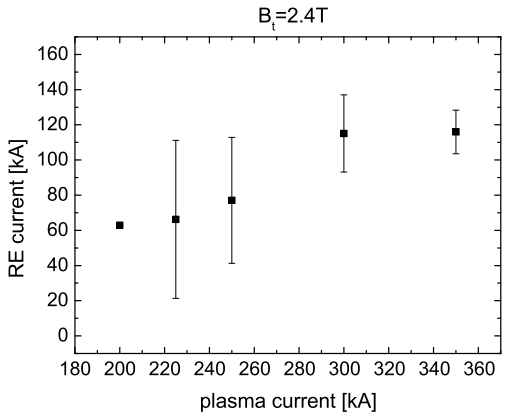

(b) Mean RE currents

Figure 5.3.9: RE currents over the predisruptive plasma current

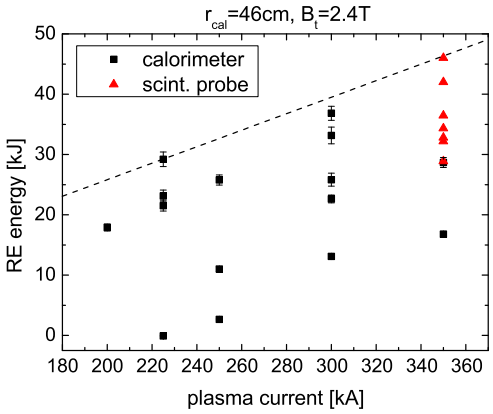

(a) Overview of the measured values and a dashed line which indicates an upper limit according to the geometrical interpretation of the data

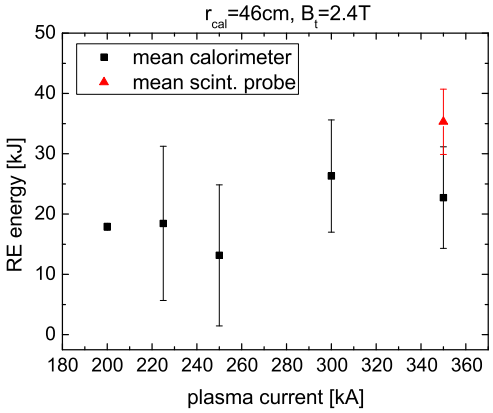

(b) Mean RE energies

Figure 5.3.10: RE energies, measured by the calorimeter probe and estimated from the energy spectra measured by the scintillator probe, over the predisruptive plasma current

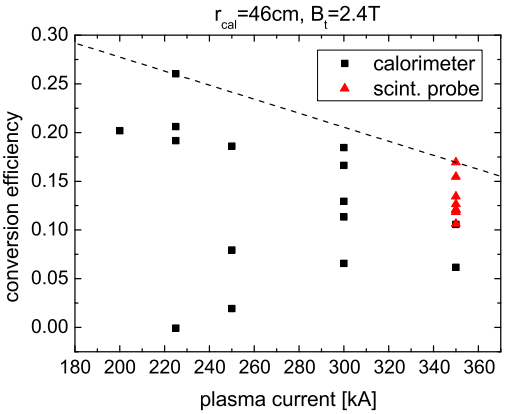

(a) Conversion efficiencies resulting from the measured RE energies and a dashed line which outlines the maximum values

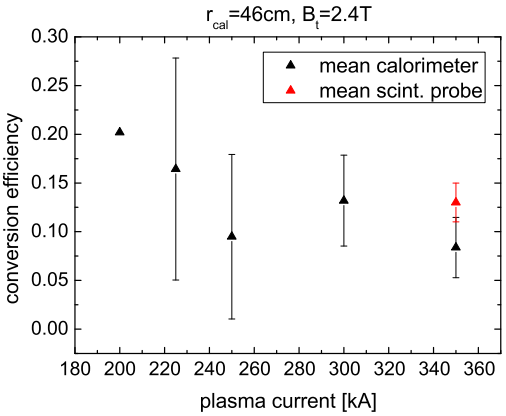

(b) Conversion efficiencies resulting from the mean RE energies

Figure 5.3.11: Conversion efficiencies of the predisruptive, magnetic plasma energy into RE energy over the plasma current for calorimeter and scintillator probe data

probe studies add very well to the new measurements. The maximum energy conversion is found to be 26 %. The conversion efficiencies which result from the mean values of the RE energy are given in figure 5.3.11(b). The I_p-dependence is very similar in both figures although the absolute values are smaller in figure 5.3.11(b).

5.3.4 Summary

The calorimeter probe allowed direct measurements of the total RE energy in tokamak disruptions. A typical RE plateau current of 100 kA was found to contain 30 to 35 kJ of RE energy at TEXTOR. The scaling of the RE energy with the RE current and thus the number of generated REs is approximately linear for RE currents above 50 kA. The RE energy which is deposited in the probe decreases for radial probe positions more than 1.5 cm behind the limiter. The RE energy load onto the PFCs is reduced by a factor of 2 by moving them 2.5 cm radially away from the plasma. The RE current and the RE energy show a RE generation threshold at $B_t \approx 2\,\mathrm{T}$. Above the threshold the RE current increases approximately linearly with B_t. This dependence is reproduced for the RE energy. The variation of the RE current with the plasma current could also be reproduced for the RE energy which strengthens the conclusion of a linear dependence of the RE energy on the RE current. The conversion of the pre-disruptive, magnetic plasma energy into RE energy during the current quench shows a tendency to decrease with increasing plasma currents. The maximum of the conversion was found at 26 %. Thus, the work presented provides additional insights about the RE energy conversion during tokamak disruptions. These results should be taken into account in future simulations of REs.

6 Transport of Runaway Electrons in Turbulent and Resonantly Perturbed Magnetic Topologies

In view of runaway mitigation techniques this chapter reports a study of the radial transport of runaway electrons in tokamak plasmas. The influences of the small-scale magnetic turbulence and externally applied resonant magnetic perturbation fields are studied. Experimental data resulting from measurements using the scintillator probe as well as a model of the runaway transport are described. The asymptotic theory of magnetic field line diffusion was used as the basis of the theoretical studies. With the help of the experimental results the formalism could be utilised to obtain an asymptotic theory of the runaway electron diffusion. This theory is only briefly introduced as it was developed by S.S. Abdullaev. The runaway transport model is described in more detail as it is part of the PhD work. The text and figures of this chapter are based on the paper [155] of the author.

6.1 Introduction

The magnetic topology of a tokamak can effectively be altered by the application of a magnetic perturbation field which is resonant to the helical equlibrium field. Due to their relativistic velocities, REs are not sensitive to electrostatic turbulences. Rather the RE transport towards the plasma edge is determined by the magnetic field. Consequently, REs can be used to study the magnetic structures in tokamak plasmas [160]. Applying a resonant magnetic field, which is connected with an ergodisation of the magnetic topology, is an effective way to enhance the RE transport and to reduce the lifetimes available for the energy gain of the REs substantially. Currently, high energy REs are one of the most serious concerns about disruptions in reactor sized tokamaks like ITER [15–17, 21]. The REs generated there can carry tens of MeV and thus can cause local energy depositions in the wall materials enough for melting or ablation. The penetration depths of tens of cm in beryllium and graphite are especially dangerous for underlying cooling structures [20]. Several RE mitigation techniques are being studied. Besides MGI [40, 116, 121] and pellet injection schemes [52, 53, 152] promising results are obtained by RMP [108, 109, 115, 122]. The underlying physics of the RE transport have been studied theoretically over many years [88, 89, 91, 93, 161–164]. Confirming the theoretical achievements by measurements is often hampered by the limitations of the RE diagnostics.
In this chapter measurements of the enhancement of the RE losses due to a resonant magnetic field are presented. The REs are measured directly at the plasma edge by the reciprocating scintillator probe. The temporal evolution of the RE losses and the dependences on the RE energy and the amplitude of the RMP are studied. Since disruptions are complex and not well reproducible, the measurements are carried out using a simpler plasma state, namely the low

density tokamak discharge of TEXTOR. A well controlled resonant magnetic field is applied externally by means of the DED. The experimental results are used to develop a model, which takes the magnetic turbulence and the external perturbation into account, to describe the radial RE transport by a diffusion process. Following an asymptotic theory, the RE orbits and local transport coefficients of the radial RE diffusion are calculated. Solving the corresponding diffusion equation delivers the RE density in the plasma and the flux of the REs which are expelled from the plasma. The output of the model is directly compared to the measurements to give an understanding of the physics of the RE transport due to the perturbed magnetic topology.
In section 6.2 the experimental setup is described. The results of the RE measurements are presented in section 6.3. Section 6.4 briefly shows how the asymptotic RE theory is used to calculate the RE orbits and the diffusion coefficients. The application of the coefficients in a diffusive RE transport model is presented in section 6.5. The results of the model are given before in section 6.6 they are compared to the measurements. A discussion of the physcial effects is carried out in section 6.7. At the end the most important achievements are summarised in section 6.8.

6.2 Experimental Scenario

The RE measurements were carried out at the middle sized tokamak TEXTOR. During the purely ohmic low density discharges REs of energies up to 30 MeV are produced reliably throughout the discharge [78]. A plasma current of $I_p = 300\,\mathrm{kA}$, a toroidal magnetic field of $B_t = 2.25\,\mathrm{T}$ and an electron density of $n_e = 0.6 \cdot 10^{19}\,\mathrm{m}^{-3}$ were chosen. After 4 s helium gas was injected into the discharge which increased the electron density to about $n_e = 3 \cdot 10^{19}\,\mathrm{m}^{-3}$. This procedure substantially reduces the number of REs striking the wall at the end of the discharge which is approached when the flux swing of the transformer is consumed after about 6 s. Consequently, RE damages to the machine are prevented.

The resonant perturbation of the regular magnetic topology was applied by the DED [109]. The perturbation coil system consists of 16 helical coils wound once around on the inner side of the TEXTOR vessel. Specifying the direction of the current in the coils respectively determines the base mode number and hence the magnetic flux surfaces resonant to the perturbation. In the experiments presented the $m/n = 6/2$ configuration of the DED was used in the DC operation. This base mode provides a radially deep ergodisation of the magnetic topology without introducing distortions due to the excitation of a tearing mode. The amplitude of the RMP was varied by scanning the current in the DED coils between $0.1\,\mathrm{kA} < I_{DED} < 7\,\mathrm{kA}$.
In order to check the RE content of the discharges, the ECE and the production of neutrons by photo-nuclear reactions due to the REs impinging on the PFCs were detected. The emphasis of the experiment lies on the measurements by the scintillator probe. The reciprocating mechanism was used to insert the probe

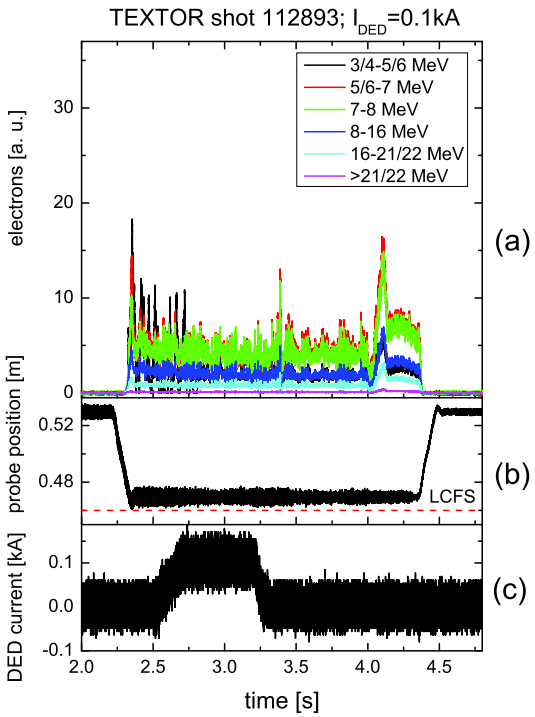

Figure 6.3.1: Temporal evolution of (a) the RE probe signal, (b) the radial position of the probe head and (c) the DED current with a plateau value at 0.1 kA

into the scrape off layer at the outer equatorial midplane on a ms timescale. The probe detects the electrons with energies above 3 to 4 MeV.

6.3 Measurements of the Runaway Electrons

The temporal evolution of a typical discharge of the RE campaign can be overviewed in figure 6.3.1. The probe signal for the different ranges of RE energy, seen in figure 6.3.1(a), starts when the probe is inserted as can be seen by comparison with the radial position of the probe shown in figure 6.3.1(b). The measuremental position of the probe head is at a minor radius of $r = 0.47\,\mathrm{m}$ which is 1 cm outside of the LCFS indicated by the dashed, horizontal line in the figure. Due to the outward shift of the REs, this position is appropriate for their detection. From the lower panel, figure 6.3.1(c), a plateau value of the DED current of $I_{DED} = 0.1\,\mathrm{kA}$ can be read. Comparing the DED current and the probe position confirms that the probe was at the measuremental position whenever the DED was activated. In the case of $I_{DED} = 0.1\,\mathrm{kA}$ no effect of

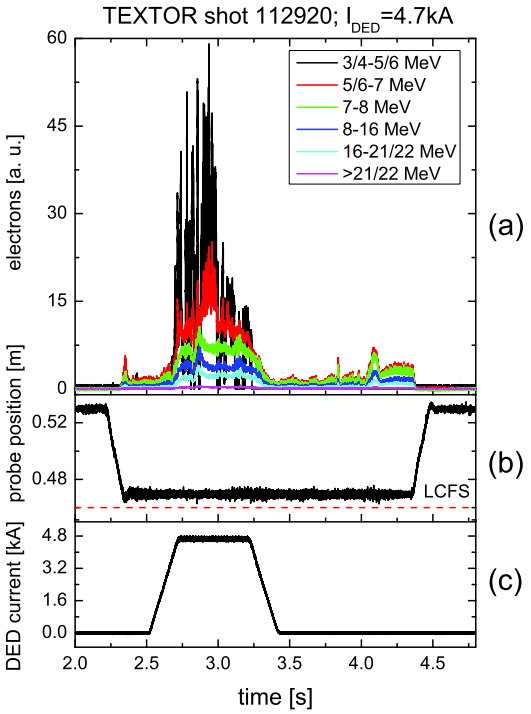

Figure 6.3.2: Temporal evolution of (a) the RE probe signal, (b) the radial position of the probe head and (c) the DED current with a plateau value at 4.7 kA

the RMP on the RE losses is observed as the amplitude of the perturbation is too low. The RE peak at about 3.4 s stems from the reversal of the flux in the transformer of TEXTOR. This has an effect on the elongation of the plasma and causes the observed RE losses. At about 4.1 s another peak of REs is caused by the injection of helium into the vessel which starts the end of the discharge and prevents the REs from damaging the machine. Analogue to the previous one figure 6.3.2 shows the case of $I_{DED} = 4.7\,\mathrm{kA}$. In the upper panel, 6.3.2(a), clearly an enhancement of the RE losses during the DED activation, seen in 6.3.2(c), can be observed. The effect is strong for the REs with energies between 3 and 5 MeV and it decreases for higher energies. This tendency becomes more obvious by looking at figure 6.3.3 which shows the case of a high amplitude RMP at $I_{DED} = 6\,\mathrm{kA}$. The reason for the energy dependence of the effect of the RMP is the shift of the REs from the resonant magnetic flux surfaces. This shift is larger for REs with higher energies and thus the perturbation appears to be more effectively shielded from them. The reason for the RE losses not being continuous but showing a spiked structure cannot be clarified from the

measurement.

For a quantitative analysis of the enhancement of the RE losses by the RMP,

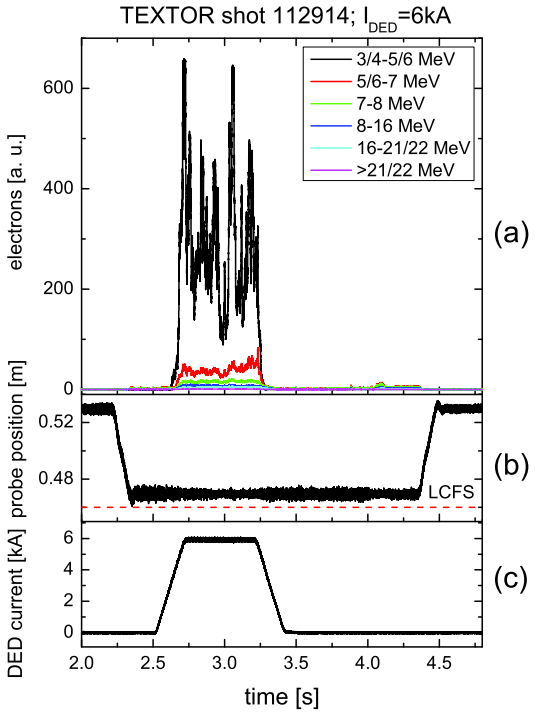

Figure 6.3.3: Temporal evolution of (a) the RE probe signal, (b) the radial position of the probe head and (c) the DED current with a plateau value at 6 kA

the ratio of the probe signal during the DED plateau phase and before the ramp-up of the DED current is calculated. The resulting factor is presented in figure 6.3.4 over the DED plateau current for the different spectral ranges. The error bars are calculated from the fluctuations of the factor between two shots with the same conditions. The dashed lines are included to improve the readability of the figure. The reason for the two outliers at 2 and 3 kA is not clear. Ignoring them, the factor increases nonlinearly with the DED current while the increase is the steepest around 4.7 kA. At this level of perturbation the losses of the REs with 3 to 5 MeV are enhanced by a factor of around 100. The factor increases to more than 1000 for $I_{DED} = 6$ kA and seems to come close to saturation at $I_{DED} = 7$ kA. The losses of the REs with energies above 21 MeV are enhanced by a factor of around 10 at $I_{DED} = 4.7$ kA which is already the saturation value.

The energy dependent influence of the RMP on the RE transport also shows an impact on the spectra of the REs expelled from the plasma as can be seen in

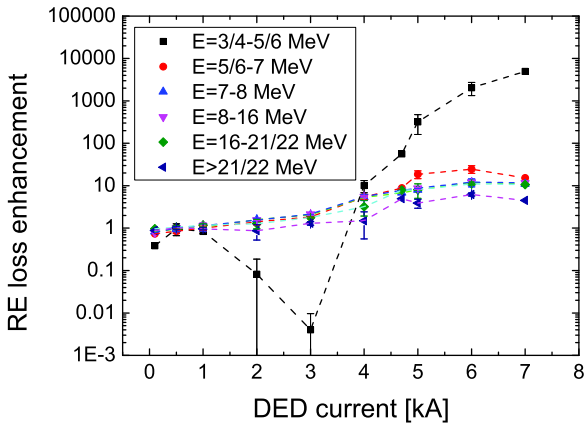

Figure 6.3.4: The factor of RE loss enhancement in dependence of the amplitude of the RMP for different RE energies; dashed lines added for readability

figure 6.3.5. As proven by figure 6.3.5(a), at a low DED current the REs have an energy spectrum which is peaked around 8 to 9 MeV. Increasing the DED current to 4.7 kA, which is done in figure 6.3.5(b), moves the peak to a lower energy of 6 to 7 MeV. For $I_{DED} = 6$ kA the RE spectrum detected by the probe is exponentially decaying as can be concluded from figure 6.3.5(c). It has to be mentioned that the detection threshold of the probe at 3 to 4 MeV may clip a peak in the spectrum at a lower energy.

6.4 Asymptotic Theory of Runaway Electron Diffusion

The theoretical analysis of the RE transport along the minor radius of the tokamak has to take the magnetic background turbulence and the application of the RMP into account. The latter causes a significant enhancement of the RE transport as it was observed in the measurements presented above. In order to describe the RE transport by a diffusive ansatz, the corresponding transport coefficients have to be calculated. Two theories are utilised for this, the asymptotic theory of the RE transport in a toroidal plasma caused by the small-scale magnetic turbulence [165] and the dynamics of the REs in the RMP field [123, 166]. Both theories are based on relativistic Hamiltonian guiding center equations for REs in toroidal plasmas. With the help of the experimental results presented above the theory of the influence of the RMP on the magnetic field lines of the tokamak configuration could be developed further to describe the influence of the RMP on the trajectories of the REs. This section does not contain a detailed derivation of the theory as this is the work of S.S. Abdullaev. Rather it provides the information which is mandatory for the presentation of the RE transport model in section 6.5.

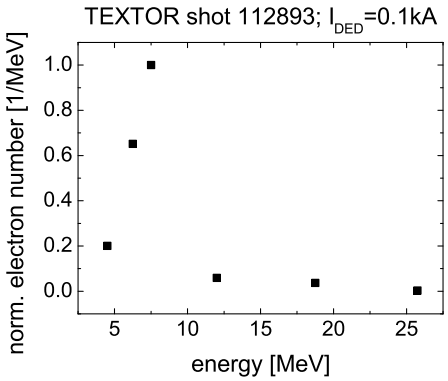

(a) RMP by a DED current of 0.1 kA

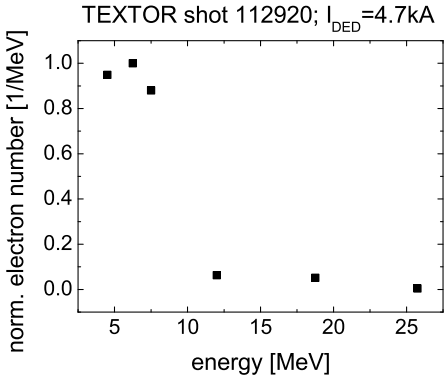

(b) RMP by a DED current of 4.7 kA

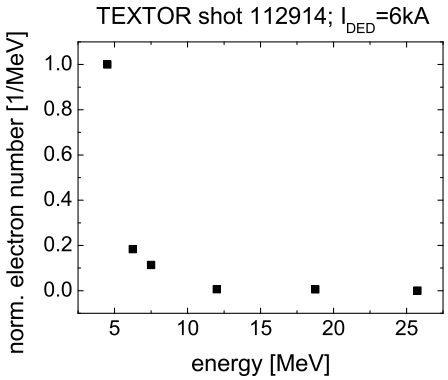

(c) RMP by a DED current of 6 kA

Figure 6.3.5: Energy spectra of the REs expelled from the plasma and detected by the probe for different amplitudes of the RMP

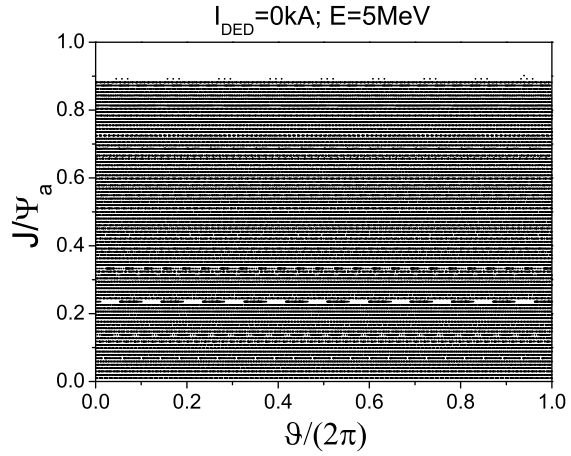

(a) Without external perturbation

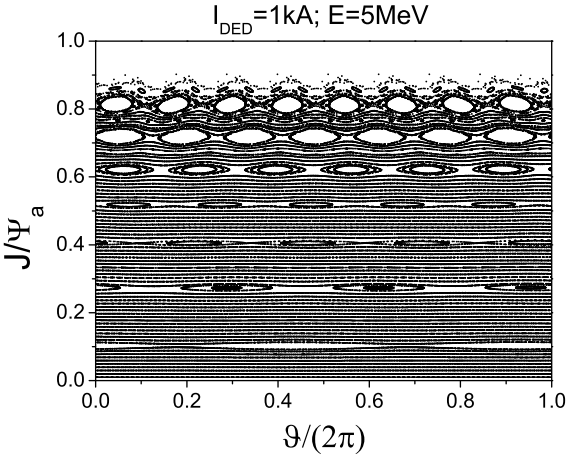

(b) RMP by a DED current of 1 kA

Figure 6.4.1: Poincaré sections of the orbits of the REs with 5 MeV for different amplitudes of the RMP and for an amplitude of the magnetic turbulence of $\epsilon = 1.41 \cdot 10^{-5}$ (continued on the next page)

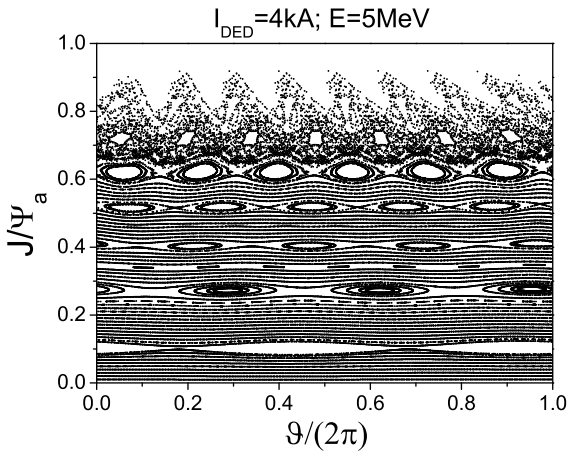

(c) RMP by a DED current of 4 kA

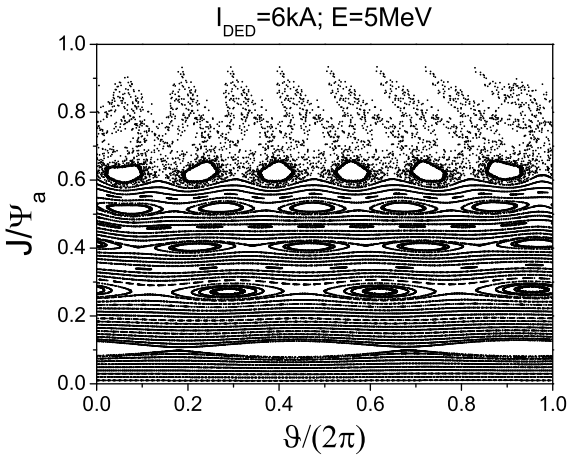

(d) RMP by a DED current of 6 kA

Figure 6.4.1: Poincaré sections of the orbits of the REs with 5 MeV for different amplitudes of the RMP and for an amplitude of the magnetic turbulence of $\epsilon = 1.41 \cdot 10^{-5}$

It is convenient to describe the relativistic guiding center equations of the electrons in the Hamiltonian presentation using the action angle variables (J, ϑ) [123, 165, 166]. These variables are introduced for the equilibrium plasma in which the guiding center orbits of the RE lie on nested drift surfaces similar to the magnetic ones. The action variable J is similar to the toroidal magnetic flux ψ and labels the drift surfaces. The angle ϑ determines the position of the guiding center along the poloidal direction. The guiding center orbit is completely determined by the canonically conjugated variables $(\vartheta, \varphi, J, p_\varphi)$ where φ and p_φ are the toroidal angle and the corresponding canonical momentum, respectively.
Magnetic fluctuations cause the radial transport of the REs across the drift surfaces. The rate of this stochastic transport can be described by a diffusion coefficient defined as the second moment of the radial displacement $D = \langle(\Delta\rho)^2\rangle/2t$ where ρ is the radial coordinate perpendicular to the drift surface J =const and $\Delta\rho = \rho(t) - \rho(0)$ is the displacement of the radial coordinate from the drift surface during a time interval t. $\langle(\dots)\rangle$ stands for the averaging over an ensemble of turbulent magnetic fields.
The simultaneous theoretical study of the RE dynamics in a magnetic field which is turbulent and resonantly perturbed encounters a difficulty in huge computational times. To overcome this problem, the RE motion in the perturbed magnetic field is studied taking the effect of the magnetic turbulence into account as random kicks on the radial coordinate. The diffusion coefficients corresponding to these random kicks are precalculated using asymptotical formulas based on the given quasilinear approximation [165]. The dimensionless level of the magnetic fluctuations is introduced as $\epsilon = b_0/B_t$ where $b_0 \sim \max|\delta B|$ cannot be measured directly. Typically, it is estimated from measurements of the radial diffusion coefficients of the REs. According to [57, 160, 167], the parameter ϵ takes values between 5×10^{-6} and 1×10^{-5} in ohmic plasmas. The dependence of ϵ on the toroidal magnetic field B_t is estimated in [168]. It is shown that at $B_t = 2.7\,\mathrm{T}$ ϵ varies between $0.65 \cdot 10^{-5}$ and $0.7 \cdot 10^{-5}$ and at $B_t = 2.0\,\mathrm{T}$ between $1.75 \cdot 10^{-5}$ and 1.9×10^{-5}. Interpolating leads to $\epsilon = 1.41 \cdot 10^{-5}$ at $B_t = 2.25\,\mathrm{T}$ which is the level of turbulence relevant for the simulation of the experiments presented above. The perturbation fields created by the DED are modeled as shown in [128]. The model reproduces the features of the heat deposition patterns experimentally observed in the TEXTOR DED [128, 169] very well.

Poincaré sections of the guiding center orbits in the $(\vartheta, J/\psi_a)$-plane are shown in the figures 6.4.1(a) to 6.4.1(d) for the REs carrying 5 MeV energy and for different amplitudes of the RMP generated by the 6/2 DED configuration. ψ_a is the toroidal magnetic flux through the last closed magnetic surface. At $I_{DED} = 0\,\mathrm{kA}$ the RE orbits form regular closed surfaces as can be seen in figure 6.4.1(a). Figure 6.4.1(b) marks the formation of orbit islands mainly in the edge region at a DED current of 1 kA. Increasing the current to 4 kA, shown in figure 6.4.1(c), the edge becomes stochastic. In addition, these stochastic trajectories form an open chaotic system because they are connected to the wall. As the REs have relativistic velocities and a very low collisionality, after entering the stochastic edge region they strike the wall on a timescale very short compared

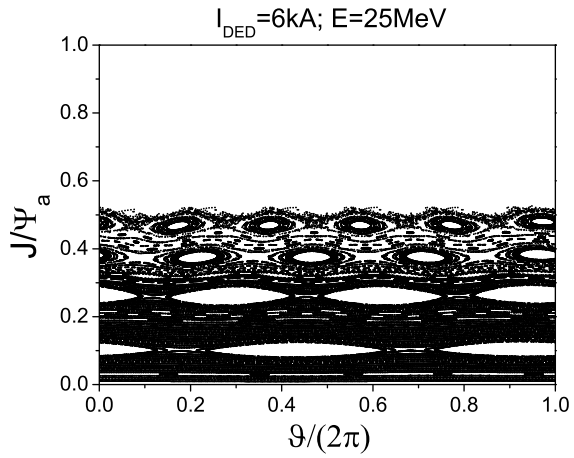

Figure 6.4.2: Poincaré section of the orbits of REs with 25 MeV for a RMP by $I_{DED} = 6\,\mathrm{kA}$ and for an amplitude of the magnetic turbulence of $\epsilon = 1.41 \cdot 10^{-5}$

to the other transport effects. Inside the plasma four island chains are formed. At the higher current of $I_{DED} = 6\,\mathrm{kA}$ the sizes of the inner island chains are increased and the edge region becomes more ergodic and more trajectories are opened up to intersect the wall. Due to the larger shift from the resonant magnetic flux surfaces, the orbits of the REs with higher energies are less perturbed as can be seen in figure 6.4.2 for 25 MeV electrons and $I_{DED} = 6\,\mathrm{kA}$. The ergodic edge region is smaller and the whole structure appears shifted along the normalised radial coordinate due to the larger orbit displacement.
The radial displacement Δr of the REs is computed following the calculated orbits from a starting position and assuming the turbulence level $\epsilon = 1.41 \times 10^{-5}$ as mentioned above. After an initial ballistic phase the second moment of Δr can be assumed to behave linearly in time. Thus, the diffusion coefficients are calculated according to $D(r, E) \propto d\left\langle (\Delta r)^2 \right\rangle / (dt)$. The angled brackets denote an averaging over the magnetic surfaces. E is the RE energy for which in 5 MeV steps the values from 5 to 30 MeV are considered. Throughout the model the three cases $I_{DED} = 0\,\mathrm{kA}$, 4.7 kA and 6 kA are treated. Figure 6.4.3 shows the diffusion coefficients of the three cases as three-dimensional plots. The left axis, going into the paper plane, shows the RE energy from 5 to 30 MeV in 5 MeV steps with linearly interpolated values in between. The right axis scales the minor radius of the plasma and the vertical axis gives the diffusion coefficient. Please notice that for a better clarity the scale of the vertical axis changes from figure 6.4.3(a) to 6.4.3(b) and 6.4.3(c) by an order of magnitude and hence the large coefficients at the edge are clipped in the figures 6.4.3(b) and 6.4.3(c). Furthermore, the RE energy axis reverses from figure 6.4.3(a) to 6.4.3(b) and 6.4.3(c). Figure 6.4.3(a) shows $D(r, E)$ defined by the magnetic turbulence only ($I_{DED} = 0\,\mathrm{kA}$) which means a reproduction of the results in [168]. Clearly, the

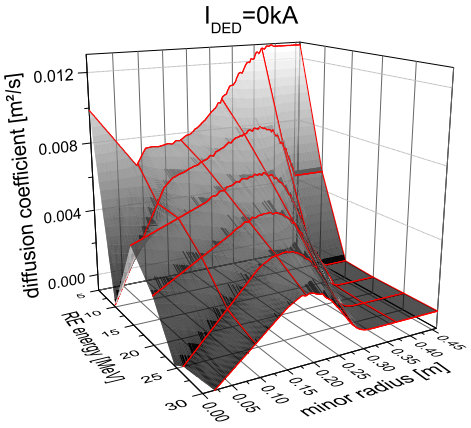

(a) Without external perturbation

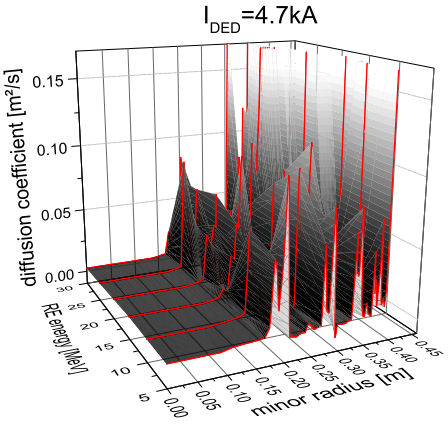

(b) RMP by a DED current of 4.7 kA

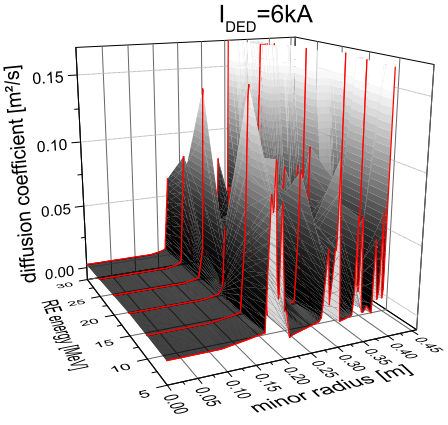

(c) RMP by a DED current of 6 kA

Figure 6.4.3: Calculated local diffusion coefficients of the REs depending on the minor radius and the RE energy for different amplitudes of the RMP and for an amplitude of the magnetic turbulence of $\epsilon = 1.41 \cdot 10^{-5}$

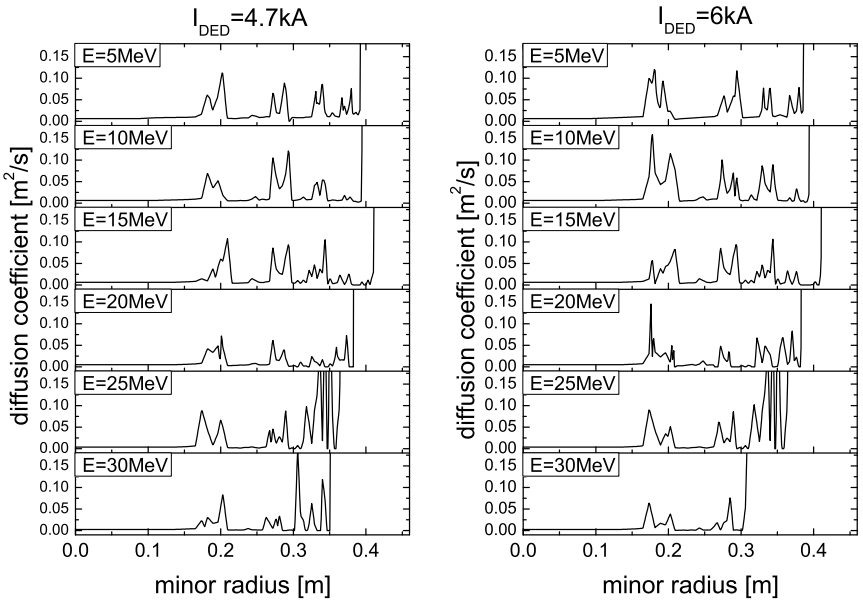

(a) RMP by a DED current of 4.7 kA (b) RMP by a DED current of 6 kA

Figure 6.4.4: Calculated local diffusion coefficients of the REs depending on the minor radius for the RE energies considered and for different amplitudes of the RMP and for an amplitude of the magnetic turbulence of $\epsilon = 1.41 \cdot 10^{-5}$

coefficient decreases going to the higher RE energies. At $I_{DED} = 4.7\,\mathrm{kA}$ and $I_{DED} = 6\,\mathrm{kA}$, shown in the figures 6.4.3(b) and 6.4.3(c) respectively, the diffusion coefficients have a pedestal value determined by the magnetic turbulence in the regions of the regular RE flux surfaces. In addition, four double peaks can be identified in the radial dependence. The peaks in $D(r)$ are a consequence of the four large island chains observed in figure 6.4.1. The maxima correspond to the inner and outer edges of the islands where the transport is enhanced and the minima in between correspond to the centres of the islands where the REs are relatively well confined. Along the open trajectories at the plasma edge the transport is not diffusive and thus no coefficients can be calculated. Instead, to include this region in the model as well, very high values of $D = 10\,\mathrm{m}^2/\mathrm{s}$ are assumed to mimic the instantaneous loss of the REs to the wall. The figures 6.4.4(a) and 6.4.4(b) clarify the radial structure of the diffusion coefficients better as they show the radial dependence for the calculated energy values only. The case of a DED current of 4.7 kA can be seen in figure 6.4.4(a) and 6 kA in figure 6.4.4(b).

6.5 Runaway Electron Transport Model

The diffusion coefficients $D(r, E, t)$, calculated for the RE transport due to the magnetic turbulence and the RMP by means of the asymptotic theory, are used in the cylindrically symmetric diffusion equation

$$\frac{\partial n(r,t,E)}{\partial t} = \frac{1}{r}\frac{\partial}{\partial r}\left[rD\frac{\partial n}{\partial r}\right] - \frac{c}{2\pi R}U_{loop}\frac{\partial n}{\partial E}. \tag{6.5.1}$$

Here n is the RE density in $\mathrm{MeV}^{-1}\mathrm{m}^{-3}$ and E is the RE energy in MeV. The last term on the right hand side takes the acceleration of the electrons by the loop voltage $U_{loop} = 1\,\mathrm{V}$ into account. The boundary conditions are for the edge $n(r = a, t, E) = 0$ and for the plasma centre $\partial n(r = 0, t, E)/(\partial r) = 0$. The secondary generation of the REs is implemented by

$$\frac{\partial n(r,t,E = 4\,\mathrm{MeV})}{\partial t} = \beta n_{e0} F(r) \int_{E_{min}}^{E_{max}} n(r,t,E)dE. \tag{6.5.2}$$

The form function herein is

$$F(r) = \left[1 - (r/a)^2\right]^{\nu},\ \nu = 2. \tag{6.5.3}$$

The limits of the integral are $E_{min} = 5\,\mathrm{MeV}$ and $E_{max} = 15\,\mathrm{MeV}$. The secondary REs are generated at $E = 4\,\mathrm{MeV}$ which should be a realistc value according to the theory of the avalanching predicting the generation at $E \leq 4\,\mathrm{MeV}$. Most of the momentum of the REs generated as secondaries is perpendicular to the toroidal direction. Because of their high energy, also these particles can be considered as collisionless. Thus, they are accelerated in the toroidal direction while they keep their perpendicular momentum. After about 0.033 s these particles reach an energy of 5 MeV. From this energy on the simulation of the diffusion is started. In the model the primary generation of the REs (Dreicer effect) is neglected because it is important only during the startup phase when the loop voltage is high. The increase of the RE population due to the secondary generation is taylored by setting $\beta n_{e0} = 0.38\,(\mathrm{MeV}\cdot\mathrm{s})^{-1}$ where $n_{e0} = 5 \cdot 10^{18}\,\mathrm{m}^{-3}$ is the central thermal electron density. By varying β the slope of the increase of the RE density throughout the discharge can be fitted to the experimental observations. Choosing n_{e0} determines the absolute level of the generated RE density. As the initial condition $n(r, t = 0; E) = n_0 F(r) \exp(-E/E_0)$ is chosen with the central RE density $n_0 = 5 \cdot 10^{11}\,\mathrm{m}^{-3}$ and the e-folding energy $E_0 = 10\,\mathrm{MeV}$. During the first 2 s of the simulation no magnetic perturbation is applied which means the diffusion coefficient is constant in time and the one in figure 6.4.3(a). After the RE density $n(r, E, t)$ reaches an equilibrium the DED current is gradually ramped up to its plateau value at 4.7 kA or 6 kA between $2\,\mathrm{s} < t \leq 2.2\,\mathrm{s}$. Until the end of the simulation at $t = 3\,\mathrm{s}$ the DED current is kept constant. Using the reference case $I_{DED} = 0\,\mathrm{kA}$ for $0\,\mathrm{s} \leq t \leq 3\,\mathrm{s}$, the fitting parameter β is chosen to reproduce the unperturbed case measured in [78]. In order to solve the diffusion equation, the partial differential equation

solver PDE2D [170] is utilised with the help of its developer G. Sewell. The output of the model are the RE flux at the plasma edge

$$\Gamma(r=a,t,E) = D\frac{\partial n(r=a)}{\partial r}4\pi^2 aR \tag{6.5.4}$$

and the number of the REs in the plasma volume

$$N_{RE}(t,E) = 4\pi^2 R\int_0^a rn(r,t,E)dr. \tag{6.5.5}$$

Figure 6.5.1 shows the RE flux $\Gamma(r=a,t)$ through the plasma edge for dif-

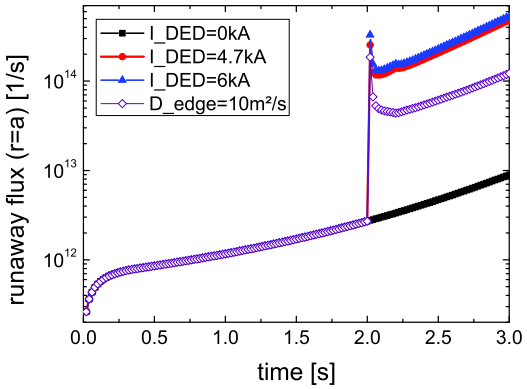

Figure 6.5.1: Simulated RE flux at the plasma edge integrated over the electron energy for different RMP amplitudes

ferent DED currents integrated over the RE energy. For $I_{DED} = 0\,\mathrm{kA}$ the increase is determined by the exponential growth of the RE population due to the avalanching. At $t = 2\,\mathrm{s}$ a step in the flux is observed when the DED current is ramped up to 4.7 kA. The depletion of the REs from the resonantly perturbed regions causes an initial overshoot of the flux. Afterwards, a new equilibrium of the losses and the generation of the REs is established and the slope of $\Gamma(r=a,t)$ is the same as without RMP. Increasing the amplitude of the RMP to $I_{DED} = 6\,\mathrm{kA}$, the step at $t = 2\,\mathrm{s}$ is only slightly higher than in the previous case. This observation is in agreement with the Poincaré sections for the two cases which differ only by the amount of stochastisation of the edge orbits. For the fourth case shown in figure 6.5.1 the DED current is set to 0 kA, but at the edge the diffusion coefficient is $D = 10\,\mathrm{m}^2/\mathrm{s}$ like in the cases with RMP causing the RE trajectories at the edge to be open. The RE flux is much smaller than for the two cases with RMP which enables a clear distinction between the effects of the open trajectories at the edge and the formation of the

magnetic islands within the plasma. Thus, the enhancement of the RE transport by the DED is not only due to the edge effect but also due to the change of the magnetic topology inside the plasma.

Figure 6.5.2 displays the RE density over time for the different RE energies

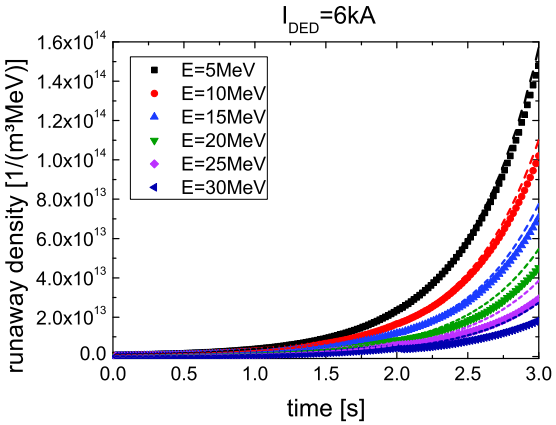

Figure 6.5.2: Temporal evolution of the density of the REs in the plasma, carrying different amounts of energy, for the cases of a DED current of 6 kA (data markers) and without RMP (dashed lines)

resulting from the fluxes. The data markers represent the case of $I_{DED} = 6\,\mathrm{kA}$ while the dashed lines give a comparison to the evolution of the density without RMP. At $t = 2\,\mathrm{s}$ the RE density drops due to the activation of the DED. Afterwards, the RE density continues to grow with a slightly shallower slope than without perturbation. The effect of the DED on the RE density is clearly larger for the higher RE energies which shows that the lifetimes of the REs become too short for the acceleration to the highest energies.

Figure 6.5.3 shows the spectra of the RE flux $\Gamma(E)$ through (a) the toroidal surface with a minor radius of $r = 0.1\,\mathrm{m}$ and (b) through the plasma boundary at $r = 0.46\,\mathrm{m}$ taken at $t = 3\,\mathrm{s}$. No RMP is applied in this case. The spectrum within the plasma is monotonically decreasing from the lowest energy $E = 4\,\mathrm{MeV}$ on. The spectrum at the plasma edge is qualitatively different as it is characterised by a peak at about 8 MeV. Figure 6.5.4 shows the corresponding spectra under the influence of a perturbation field generated by a DED current of $I_{DED} = 6\,\mathrm{kA}$. The flux spectrum within the plasma, shown in figure 6.5.4(a), is in its shape and absolute values similar to the unperturbed case. The spectrum at the boundary shows a completely different picture as can be seen in figure 6.5.4(b). The flux is more than an order of magnitude higher than in the unperturbed case. Starting at $E = 4\,\mathrm{MeV}$ and going to higher energies, the spectrum decreases steeply and the behaviour seems to be noisy. At 15 MeV a pronounced peak can be identified. This peak remains the same when the grid size or the number of time steps used by PDE2D are changed. Instead, flatten-

ing the profile of the diffusion coefficient leads to a reduction of the "noise" and the peak which suggests that both are real physical effects rather than artifacts of the model. The discussion of this result in comparison with the measurements will provide insights into the physics of the RE transport.

For this discussion the radial dependence of the secondary RE generation rate,

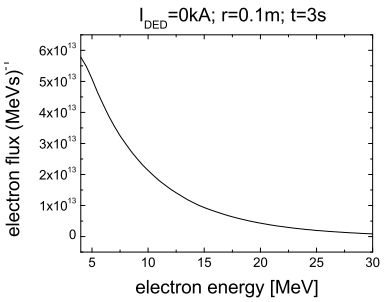

(a) RE flux through the toroidal surface with the minor radius $r = 0.1\,\mathrm{m}$

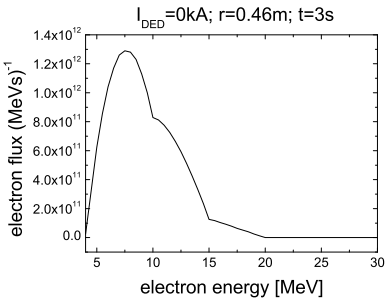

(b) RE flux through the plasma boundary at the minor radius $r = 0.46\,\mathrm{m}$

Figure 6.5.3: RE flux spectra taken at the end of the simulations for $I_{DED} = 0\,\mathrm{kA}$

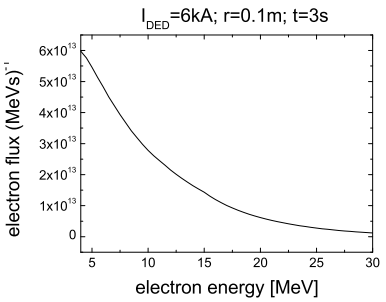

(a) RE flux through the toroidal surface with the minor radius $r = 0.1\,\mathrm{m}$

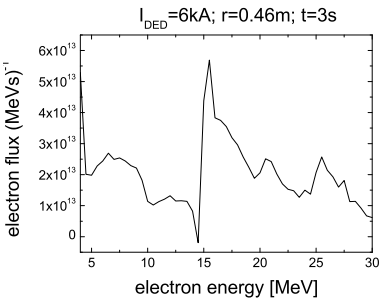

(b) RE flux through the plasma boundary at the minor radius $r = 0.46\,\mathrm{m}$

Figure 6.5.4: RE flux spectra taken at the end of the simulations for $I_{DED} = 6\,\mathrm{kA}$

presented in figure 6.5.5, will be useful. Figure 6.5.5(a) shows the RE birth rate over the minor radius at different times during the simulation without RMP. The generation of the secondary REs depends on the radial profile of the RE density. Thus, the birth of the secondary REs is peaked in the plasma centre and it decreases gradually going outwards. While more and more REs are accumulated in the plasma the birth rate grows in time until an equilibrium profile is established. Figure 6.5.5(b) shows the RE generation rate in a simulation

with a perturbation current of $I_{DED} = 6\,\mathrm{kA}$. The picture is very similar to the unperturbed one showing again a centrally peaked RE generation at the same absolute values. In difference to the previous case two small plateaus at $r \approx 0.2\,\mathrm{m}$ and at $r \approx 0.3\,\mathrm{m}$ are observed in the radial profile after the DED is switched on.

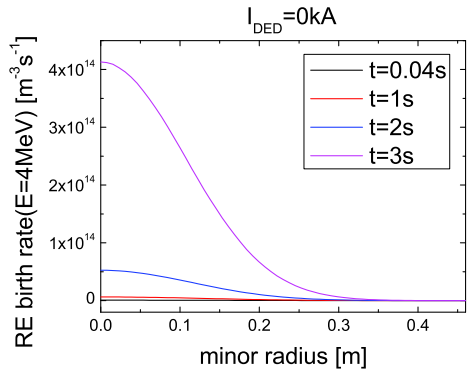

(a) Without external perturbation

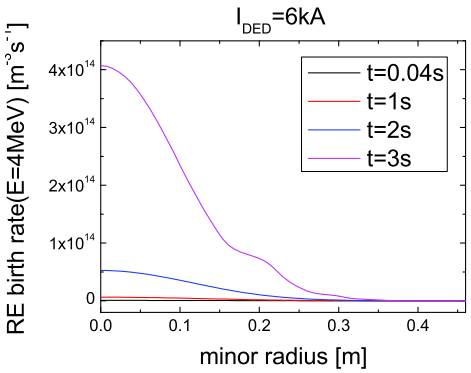

(b) RMP by $I_{DED} = 6\,\mathrm{kA}$

Figure 6.5.5: RE generation rate over the minor radius at different times during the simulation

6.6 Comparison of the Experimental and Simulated Results

In order to analyse the enhancement of the RE transport due to the RMP, the figures 6.3.4 and 6.5.1 are compared. At a DED current of 4.7 kA the experiment shows an increase of the losses of the REs carrying 3 to 5 MeV by a

factor of about 100 and by a factor of about 10 for the higher energies. In good agreement the simulated energy integrated RE flux increases by a factor of the order of 100. For $I_{DED} = 6\,\mathrm{kA}$ the measured RE losses are about 1000 times higher than without perturbation for the REs with energies between 3 to 5 MeV. The losses of the high energy REs are again only about 10 times increased. The simulated energy integrated RE flux in figure 6.5.1 for $I_{DED} = 6\,\mathrm{kA}$ again increases by two orders of magnitude. It has to be kept in mind that the integrated flux of the model contains only the REs with $E \geq 4\,\mathrm{MeV}$ which might cause a tendency to a lower enhancement factor.
The RE energy spectra measured by the scintillator probe and shown in figure 6.3.5 can be compared to the calculated flux spectra shown in the figures 6.5.3(b) and 6.5.4(b). In the unperturbed case the measurement and the model agree in showing a peaked spectrum with a maximum at about 8 MeV. For a magnetic perturbation by $I_{DED} = 4.7\,\mathrm{kA}$ the measured energy spectrum is peaked while the simulation gives a spectrum similar to the case of $I_{DED} = 6\,\mathrm{kA}$. The latter, shown in figure 6.5.4(b), is steeply decreasing from 4 MeV to higher energies and it has a peak at 15 MeV. The measured spectrum (figure 6.3.5(c)) also decreases steeply coming from 3 to 4 MeV. The peak at 15 MeV cannot be resolved by the measurement as the signal is averaged over the range of 8 to 16 MeV and so the peak is cancelled out. It has to be mentioned that the measurements in section 5.2 and [149] show an exponential RE energy spectrum with a peak around 15 MeV during the current quench phase of TEXTOR disruptions. The loss mechanism of the REs during the disruption is believed to be connected to the formation of tearing modes. In both cases, the RMP and the tearing modes, the ergodisation of the magnetic field causes the loss of the REs.
Eventually, a good agreement between the probe measurements and the transport model is achieved for discharges without RMP and with high amplitudes of the RMP. In the next step a physical explanation of the observations is given.

6.7 Physical Discussion of the Results

The case of a high RMP amplitude is treated first. As can be seen in figure 6.4.1(d), the effective plasma radius for the REs is obtained by excluding the region of the open field lines at the edge. This leads to $r_{eff} \leq 0.6 \cdot 0.46\,\mathrm{m} = 0.28\,\mathrm{m}$. The RE spectrum which is observed at the plasma boundary is steeply decreasing coming from 4 MeV and going to higher energies. This part of the spectrum is established right after the DED is switched on. In contrast, the peak at 15 MeV gradually grows in time. The birth rate of the REs is centrally peaked and it shows a half width at half maximum (HWHM) of about 0.1 m. In addition, small plateaus of the birth rate can be seen at $r \approx 0.2\,\mathrm{m}$ and at $r \approx 0.3\,\mathrm{m}$. These plateaus appear after the DED is switched on.
They can be explained by REs being confined in the centres of orbit islands and causing the generation of secondary REs there. The corresponding island chains can be found in the Poincaré sections and as double peaks in the radial profile

of the diffusion coefficient in figure 6.4.4(b). The secondary REs generated at $r \approx 0.2\,\mathrm{m}$ and at $r \approx 0.3\,\mathrm{m}$ are very quickly expelled from the plasma because the effective plasma radius is only $r_{eff} \leq 0.28\,\mathrm{m}$. Thus, these REs cannot be accelerated to energies significantly above 4 MeV and so they form the low energy part of the observed spectrum.
In order to populate the spectral peak at 15 MeV, the secondary REs born at 4 MeV have to gain 11 MeV by the acceleration due to the loop voltage of 1 V. In a simple nonrelativistic estimation the REs need about $\Delta t = 0.4\,\mathrm{s}$ for the acceleration. This duration is large on the timescale of the simulation between $2\,\mathrm{s} \leq t \leq 3\,\mathrm{s}$ and it explains the gradual increase of the 15 MeV peak in the spectrum. The radial distance which the REs have to diffuse from the centre to the effective boundary is $\Delta r = 0.28\,\mathrm{m}$. The REs which start at the HWHM of the radial birth rate profile have to diffuse $\Delta r = 0.18\,\mathrm{m}$. Estimating the diffusion coefficient from these assumptions yields $D = (\Delta r)^2/\Delta t = 0.08$ to $0.19\,\mathrm{m}^2/\mathrm{s}$. This is consistent with the diffusion coefficient calculated in section 6.4 and shown in figure 6.4.3(c) which is of the order of $0.1\,\mathrm{m}^2/\mathrm{s}$. Consequently, the RMP triggers the loss of the REs even from the centre of the plasma before they can be accelerated to the highest energies. This result emphasises the potential of the RMP for the mitigation of REs in tokamak disruptions.
The case without RMP shows a RE spectrum at the plasma boundary which is characterised by a peak at 8 MeV as can be seen in the figures 6.3.5(a) and 6.5.3(b). In the simulation this peak comes from lower energies and moves on the energy axis in time. In order to form the 8 MeV peak, the REs born with 4 MeV have to gain another 4 MeV due to their acceleration. This needs only about 0.13 s. Using a rough approximation of the diffusion coefficient calculated in section 6.4 and shown in figure 6.4.3(a) of $D \approx 0.01\,\mathrm{m}^2/\mathrm{s}$, the time needed for the REs to diffuse from the centre to the edge, which means $\Delta r = 0.46\,\mathrm{m}$, can be estimated to be $\Delta t = 21.2\,\mathrm{s}$. During this long time span in the plasma the REs can gain energies much larger than 8 MeV but as they are confined in the plasma for such a long time, these REs are not seen at the plasma edge during the time of observation. In consequence, the flux at the plasma edge, shown in figure 6.5.3(b), is more than an order of magnitude smaller than the flux in the perturbed case shown in figure 6.5.4(b). The REs which form the 8 MeV peak in the spectrum have been accelerated for only 0.13 s. Taking into account $D \approx 0.01\,\mathrm{m}^2/\mathrm{s}$, the radial distance passed is only $\Delta r = 3.6\,\mathrm{cm}$. Thus, during the time of observation only REs generated a few cm away from the plasma boundary can be seen there. This far outside the secondary generation rate is already quite low which explains the small RE flux observed. During the simulation the peak in the spectrum moves to higher energies in time because more and more REs from deeper inside the plasma have enough time to reach the edge. The other REs stay in the plasma and they are not seen at the edge, neither in the measurement nor in the simulation.
The physical analysis of the RE transport given emphasises the dominating role of the secondary RE generation mechanism in ohmic RE discharges. As already mentioned, the secondary RE generated by collisions of thermal electrons with a RE seed population have a velocity vector with a large perpendicular contri-

bution [74]. For the simulations presented above the ratio of the perpendicular momentum to the parallel momentum was assumed to be 0.1. In [78, 111] the detection of the synchrotron radiation of REs in low density TEXTOR discharges was utilised to study the perpendicular momentum of the REs inside the plasma. The perpendicular momentum was determined by a detailed analysis of the shape of the synchrotron image. For a given energy of the REs the synchrotron radiation is emitted in a very narrow angle in the foreward direction of the instantaneous electron velocity. The actual image is about an order of magnitude larger than the natural opening angle. This results from a gyration of the REs around their guiding center orbits. From the measured ratio of the vertical to the horizontal extent of the image it was deduced that the perpendicular momentum amounts to about 0.1 times the longitudinal one. This high perpendicular momentum was explained by the interaction of the REs with plasma waves. This explanation might no longer be necessary as the secondary REs which dominate the discharge are already born with a high perpendicular momentum.

6.8 Summary

The enhancement of the RE losses due to the application of a RMP was measured temporally and spectrally resolved during ohmic TEXTOR discharges. In agreement with [108] the enhancement of the losses increases nonlinearly with the amplitude of the RMP. Taking into account the magnetic turbulences and the perturbation field, the RE orbits and transport coefficients were calculated by means of an asymptotic theory. The description of the enhanced RE transport by a diffusive model is in agreement with the results of the measurement. In unperturbed plasmas the RE transport is found to be determined mainly by the magnetic turbulence and the RE energy due to the orbit displacement. Including the RMP changes the magnetic field structures at the edge and inside the plasma significantly which has a major influence on the RE transport. As the magnetic islands inside the plasma verifiable enhance the RE transport, a screening of the RMP by plasma currents can be excluded for TEXTOR. For the maximum effective RMP the high energy RE losses are enhanced by a factor of 10. For the REs carrying energies between 3 and 5 MeV the maximum loss enhancement is about 1000 times. The impact of the perturbation on the volume integrated density is more effective for the high energy REs which is in agreement with the suppression of the REs with energies above 25 MeV in TEXTOR disruptions [115]. This can be understood in terms of the reduction of the time which is available to accelerate the low energy REs due to their enhanced transport. This result strengthens the relevance of the presented study for the application of RMP fields for the mitigation of the REs in disruptions. The energy spectrum of the REs at the plasma edge resulting from the model is in agreement with the experiment for the case without RMP. Including the perturbation field, the model shows a peak in the energy spectrum which cannot be resolved by the measurement. Because the peak typically showed up in disrup-

tion measurements, common physics of the RE transport due to the perturbed magnetic topologies in the current quench of disruptions and due to the RMP are suggested. The RE energy spectra found inside the plasma show qualitative differences to the edge spectra. Both are explained by the competition between the RE generation rate and the radial diffusion. During the stationary phase of the ohmic discharges the secondary generation is found to be the dominant RE production channel.
Treating unperturbed magnetic topologies and RE discharges to which a high amplitude RMP is applied, a self consistend picture of the RE transport is drawn. This implies the loss of the REs due to the RMP from the whole plasma volume before the electrons can be accelerated to the highest energies. Thus, a prospect which shows how RMP fields can work for the mitigation of the REs in tokamak disruptions is pointed out.

7 Summary

The operation of future, reactor sized tokamaks will decide about the feasibility of using nuclear fusion as a source of energy. In view of disruptions in tokamaks like ITER REs are one of the main concerns regarding the integrity of the fusion machines. If a tokamak plasma disrupts, the confinement is destroyed and the thermal energy of the plasma is expelled to the wall as well as preexisting REs. Due to the sudden cooling of the plasma, its resistivity rises and large electric fields can occur. These fields enable the acceleration of the electrons into the runaway regime. The REs can carry about 70 % of the plasma current at energies of tens of MeV. Eventually, in the course of the current quench the REs are expelled from the plasma in form of very short, repetitive events which were measured previously via the detection of X-rays [22]. The exact temporal characteristics of these bursts of RE losses could not be resolved as the resolution of the former measurements was not sufficient. Besides the details of the temporal evolution of the RE bursts numerous other important questions about the physics of the REs in tokamak disruptions have remained open. The energy spectra corresponding to the RE bursts and the physical mechanism which triggers the formation of the bursts are unknown. The total energy carried by the REs in disruptions, the conversion factor of magnetic plasma energy into RE energy and the radial decay of a RE beam which is limited by an obstacle at the plasma edge are also not known. Moreover, techniques to mitigate the formation of high energy RE populations are urgently needed. These desires have been addressed in this thesis. Novel results of measurements of the REs in disruptions at the tokamak TEXTOR as well as a study of the RE transport have been presented.

The four experimental campaigns made use of three different, specialised probes which detected the REs at the plasma edge of TEXTOR. The scintillator probe enables measurements of the temporal evolution of the RE losses as well as the corresponding RE energy spectra. The calorimeter probe was designed and developed in the course of the PhD work to allow the first measurements of the total RE energy in tokamak disruptions. Using another probe, which was also designed and developed for this work, it has been shown that in a single disruption sufficient RE damages can be obtained to allow the deduction of the energy deposition and the radial decay of the REs. This heat load probe exploits the energy deposition of the REs in a material mixture of copper particles in a high temperature resistent epoxy resin. The energy of the REs from a TEXTOR disruption caused an observable damage in the probe material which was evaluated. The RE content of the discharge was independently verified by the detection of the neutrons, the $\gamma-$dose and by means of the temporal evolution of the plasma current. The RE signature in the probe material was characterised by surface electron and optical microscopy before and after the metallographical preparation of the probe core. The measurement of the spatial extent of the RE signature and thermogravimetry allowed a comparison of the results of the experiment with simulations carried out using the GEANT4 code.

A good agreement was found for a RE beam with an exponential spectrum with an e-folding energy between about 4 MeV and 9 MeV and the corresponding exponential radial decay with an e-folding length between 13 mm and 6 mm. The Larmor radius of the REs, which was previously measured during steady state discharges at TEXTOR, amounts to about 5 mm which makes a radial decay length in this regime reasonable. The option of a RE beam with an exponential spectrum and a linear radial distribution has been excluded due to a comparison with the scintillator probe measurements. Additional simulations were carried out in which energetic parts of the exponential spectrum were assigned to the RE beam. It has been shown that the spectral part of the RE energies between 8 MeV and 16 MeV caused most of the observed damages. The spectral and radial distributions were attained by a measurement only in the probe core. Electrons with energies less than 4 MeV were absorbed mainly in the graphite housing of the probe and the experiment does not describe the radial distribution of the REs in the first 6 mm of the probe housing which faced the plasma. Therefore, a second decay distribution in these first millimeters could not be excluded.

The calorimeter probe allowed direct measurements of the total RE energy in TEXTOR disruptions. A typical RE plateau current of 100 kA was found to contain 30 to 35 kJ of RE energy. The scaling of the RE energy with the RE current and thus the number of generated REs is approximately linear for RE currents above 50 kA. The RE energy which is deposited in the probe decreases for radial probe positions more than 1.5 cm behind the limiter. The RE energy load onto the PFCs is reduced by a factor of 2 by moving them 2.5 cm radially away from the plasma. The corresponding current and the energy show a RE generation threshold at $B_t \approx 2\,\mathrm{T}$. Above this threshold the RE current increases approximately linearly with B_t. This dependence was reproduced for the RE energy. The variation of the RE current with the plasma current could also be reproduced for the RE energy, which strengthens the conclusion of a linear dependence of the RE energy on the RE current. The conversion of the predisruptive, magnetic plasma energy into RE energy during the current quench shows a tendency to decrease with increasing plasma currents. The maximum of the conversion was found at 26 %. Measurements applying the scintillator probe were used as an independent check for the results. They are in good agreement and support the interpretation of the data.

The scintillator measurements allowed the first temporally and spectrally resolved analysis of the RE bursts in tokamak disruptions. The bursts have temporal widths of 0.07 to 0.17 ms and they follow each other with delays of 0.12 to 9.3 ms. The energy spectra of the bursts are approximately exponentially decaying except of an enhancement at around 15 MeV. The spectra show variations from burst to burst. Deriving from the temporal characteristics of the RE bursts and from measurements of the magnetic activity during the current quench of the disruptions, two possible instabilities which could trigger the formation of the RE bursts have been suggested: kink instabilities of the RE beam and resistive tearing modes in the postdisruptive background plasma. The temporal properties of the bursts and the similarity of the energy spectra to the ones

measured during ohmic steady state RE discharges with resonantly perturbed magnetic topologies seem to favour the second option.
The application of a RMP enhanced the RE losses which were measured temporally and spectrally resolved using the scintillator probe. The measurements showed the enhancement of the losses by a factor of 100 to 1000 for RE with energies between 3 and 5 MeV and by a factor of 10 for higher RE energies due to the perturbation. The RE energy spectrum was observed to be peaked without RMP. The perturbation fields caused a shift of the peak to lower energies. The RE transport was modelled by a diffusive process showing a good agreement with the experimental results. In unperturbed plasmas the transport is mainly determined by the RE energy (due to the orbit shift) and by the magnetic turbulence. Applying the RMP, the created field structures influence the transport greatly. Not only the open field lines at the plasma edge contribute to the RE losses but also the ergodic structures inside the plasma. Sometimes it is assumed that the RMP is shielded by plasma currents. For TEXTOR this shielding is of minor influence but in hotter H-mode plasmas it could play a more important role. The suppression of the REs above 25 MeV, shown in [115], can be understood by the reduced lifetimes of the low energy REs. Less time being available for the acceleration of the low energy REs reduces the density of the higher energy REs inside the plasma. In the model the REs are generated by the secondary process only which is concluded to be the dominant RE generation mechanism. Treating unperturbed magnetic topologies and RE discharges to which a high amplitude RMP is applied, a self consistend picture of the RE transport has been drawn.
The physical picture of the postdisruptive tokamak plasma has to be extended by the occurrence of either kink instabilities or resistive tearing modes. Some effort should be put into identifying these instabilities in future measurements. The design of future fusion devices will be influenced by the results in this thesis as the energy spectra, the total energy of the REs in disruptions and their radial decay determine the possible wall damages. The large tokamaks of the future will necessarily have actively cooled wall components and preventing RE damages to the cooling tubes presents a mandatory safety issue for the machines. Besides such instantly visible damages the energy of the REs can determine the lifetimes of the PFCs by progressive melting and ablation. Knowing the energy spectrum of the REs and their total energy makes it possible to determine these lifetimes and thus to avoid a critical operation beyond them. Moreover, the spectra of the REs determine the influence of magnetic turbulences and of the magnetic topology on the RE transport. This is an aspect which is important not only for the application of resonant magnetic perturbations as a RE mitigation technique. Picking up a proposal in [40], a next step of the RE studies at TEXTOR will be the fast injection of moderate amounts of gas as a means to mitigate the generation of high energy REs during disruptions by increasing the RE transport due to induced magnetic turbulences.

8 Thesis-Related Publications of the Author

8.1 Peer Reviewed Journals

- M. Forster, K.H. Finken, M. Lehnen, J. Linke, B. Schweer, C. Thomser, O. Willi, Y. Xu and the TEXTOR team, *Energy deposition and radial decay of runaway electrons in a disruption at TEXTOR*, Nucl. Fusion **51**, 043003 (8pp) (2011)

- M. Forster, K.H. Finken, M. Lehnen, O. Willi, Y. Xu and the TEXTOR team, *Measurements of the Runaway Electron Energy during Disruptions in the Tokamak TEXTOR*, Phys. Plasmas **19**, 052506 (2012)

- S.S. Abdullaev, K.H. Finken, M. Forster, *New mechanism of runaway electron diffusion due to microturbulence in tokamaks*, Phys. Plasmas **19**, 072502 (2012)

- M. Forster, S.S. Abdullaev, K.H. Finken, T. Kudyakov, M. Lehnen, G. Sewell, O. Willi, Y. Xu and the TEXTOR team, *Runaway Electron Transport in Turbulent and Resonantly Perturbed Magnetic Topologies of TEXTOR*, Nucl. Fusion **52**, 083016 (13pp) (2012)

- M. Forster, K.H. Finken, T. Kudyakov, M. Lehnen, O. Willi, Y. Xu, L. Zeng and the TEXTOR team, *Temporal and Spectral Evolution of Runaway Electron Bursts in TEXTOR Disruptions*, Phys. Plasmas **19**, 092513 (2012)

8.2 Conference Proceedings

- M. Forster, K.H. Finken, M. Lehnen, J. Linke, B. Schweer, C. Thomser, O. Willi and Y. Xu, *Spectrum and Radial Decay of Runaway Electrons in a Disruption at TEXTOR*, DPG-Frühjahrstagung 2011, Kiel, Germany (2011)

- M. Forster, S.S. Abdullaev, K.H. Finken, T. Kudyakov, M. Lehnen, B. Schweer, O. Willi, Y. Xu and the TEXTOR team, *Spectral Measurements of the Influence of Resonant Magnetic Perturbation on Runaway Electron Loss*, 5th International Workshop on Stochasticity in Fusion Plasmas, Jülich, Germany (2011)

- M. Forster, K.H. Finken, M. Lehnen, J. Linke, B. Schweer, C. Thomser, O. Willi, Y. Xu and the TEXTOR team, *Spectral and Radial Distributions of Runaway Electrons in a Disruption at TEXTOR*, European Physical Society 38th Conference on Plasma Physics, Strasbourg France (2011)

8.3 Invited Talks

- M. Forster, S.S. Abdullaev, K.H. Finken, T. Kudyakov, M. Lehnen, J. Linke, B. Schweer, G. Sewell, C. Thomser, O. Willi, Y. Xu and the TEXTOR Team, *Runaway Electron Probe Measurements at TEXTOR*, JET, Culham Science Centre, Culham, Great Britain (12/2011)

- M. Forster, S.S. Abdullaev, K.H. Finken, T. Kudyakov, M. Lehnen, J. Linke, B. Schweer, G. Sewell, C. Thomser, O. Willi, Y. Xu and the TEXTOR Team, *Runaway Electron Probe Measurements at TEXTOR*, Max-Planck-Institut für Plasmaphysik, Greifswald, Germany (03/2012)

Appendices

A Supplementary Data of Runaway Bursts

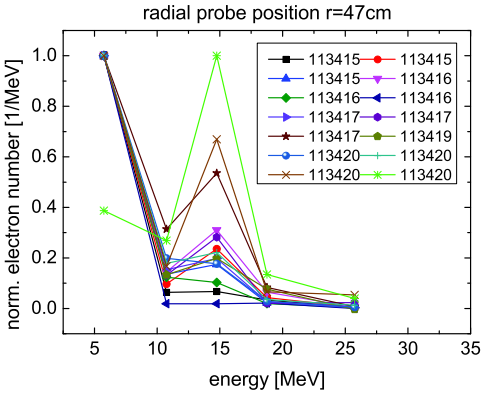

(a)

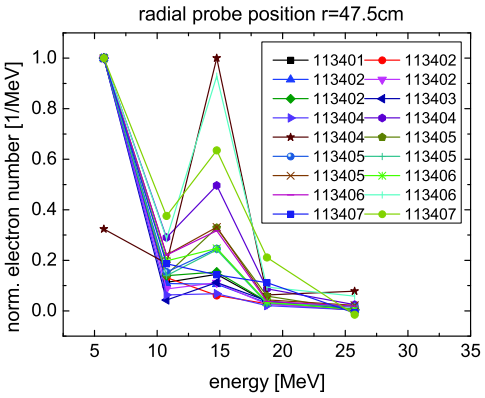

(b)

Figure A1: Histograms of energy spectra of RE bursts measured by the scintillator probe at four different radial positions; the subfigures (a) to (d) show 46 energy spectra measured during all 17 disruptions of the campaign (continued on the next page)

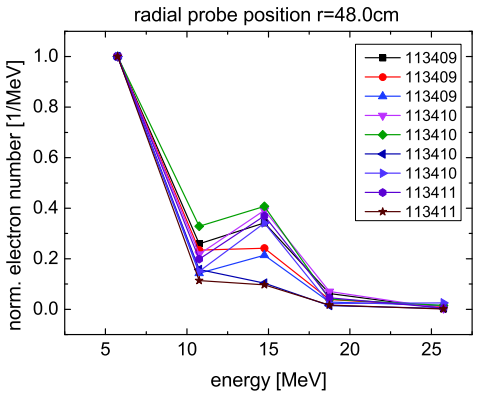

(c)

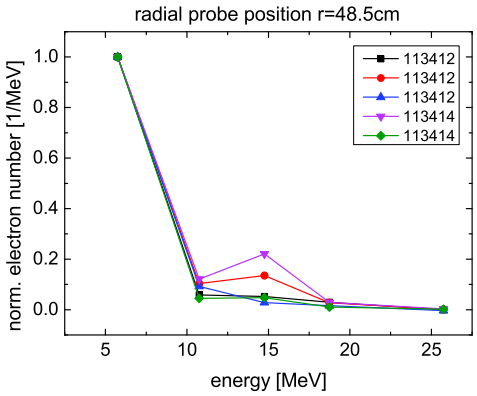

(d)

Figure A1: Histograms of energy spectra of RE bursts measured by the scintillator probe at four different radial positions; the subfigures (a) to (d) show 46 energy spectra measured during all 17 disruptions of the campaign (continued from the page before)

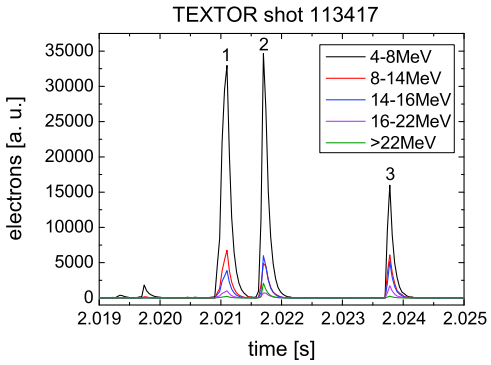

(a) Probe signal over time for different RE energy ranges; τ_{FWHM} of the bursts: 1 - 0.15 ms, 2 - 0.10 ms and 3 - 0.10 ms

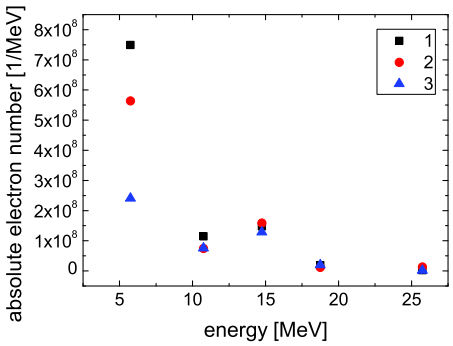

(b) Energy spectra in the 3 bursts

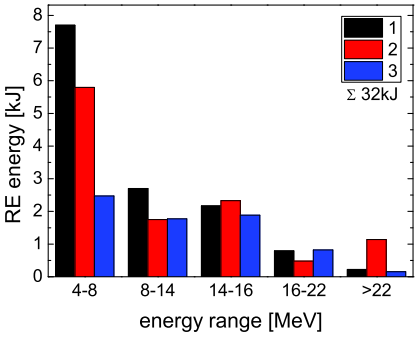

(c) Total RE energy in the 3 bursts

Figure A2: Results of a scintillator probe measurement at 47.0 cm minor radius

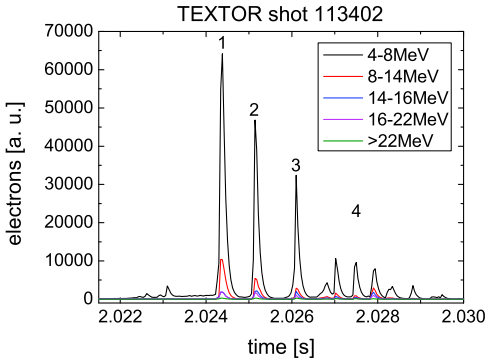

(a) Probe signal over time for different RE energy ranges; τ_{FWHM} of the bursts: 1 - 0.13 ms, 2 - 0.11 ms and 3 - 0.08 ms

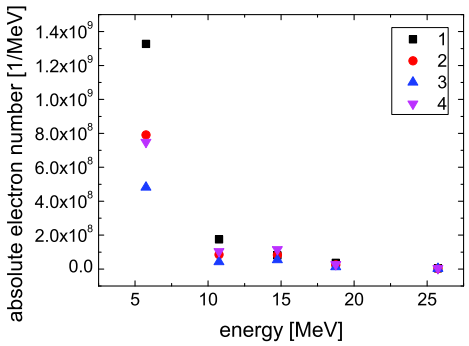

(b) Energy spectra in the 3 bursts and in region 4

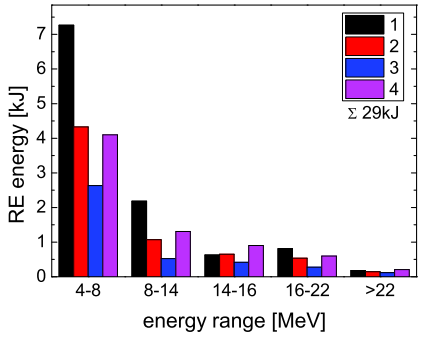

(c) Total RE energy in the 3 bursts and in region 4

Figure A3: Results of a scintillator probe measurement at 47.5 cm minor radius

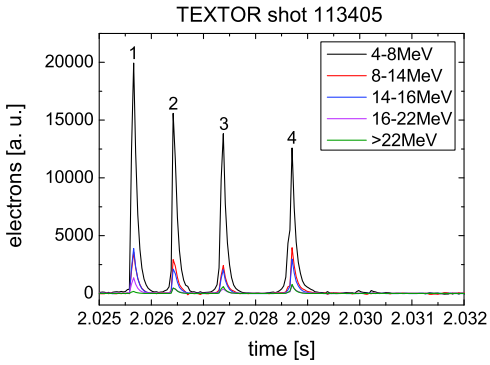

(a) Probe signal over time for different RE energy ranges; τ_{FWHM} of the bursts: 1 - 0.11 ms, 2 - 0.10 ms, 3 - 0.10 ms and 4 - 0.09 ms

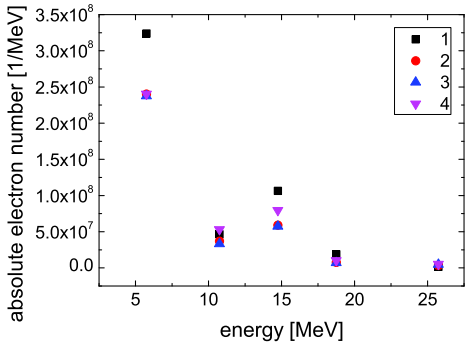

(b) Energy spectra in the 4 bursts

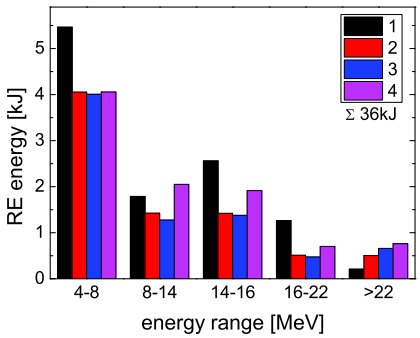

(c) Total RE energy in the 4 bursts

Figure A4: Results of a scintillator probe measurement at 47.5 cm minor radius

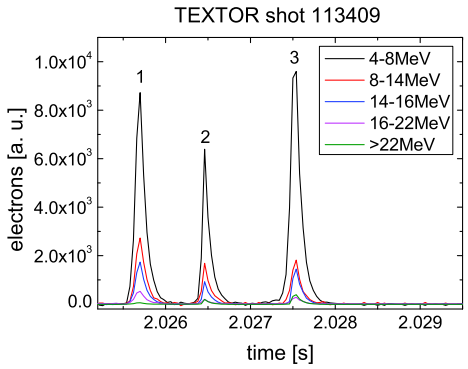

(a) Probe signal over time for different RE energy ranges; τ_{FWHM} of the bursts: 1 - 0.12 ms, 2 - 0.08 ms and 3 - 0.12 ms

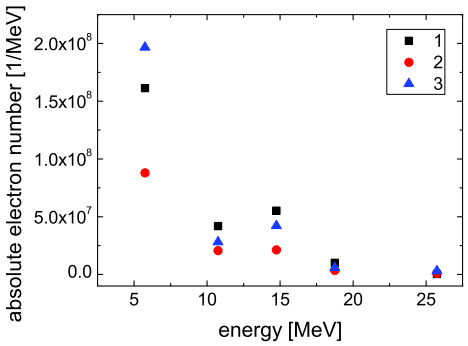

(b) Energy spectra in the 3 bursts

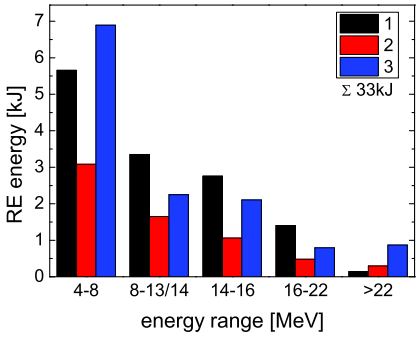

(c) Total RE energy in the 3 bursts

Figure A5: Results of a scintillator probe measurement at 48.0 cm minor radius

B Calorimeter Probe Photographs

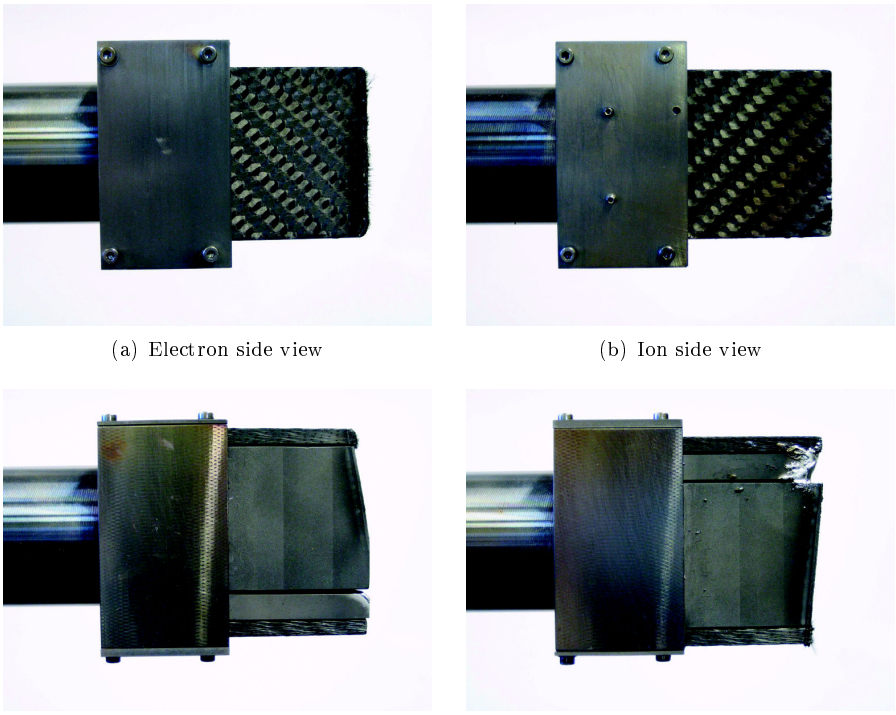

(a) Electron side view

(b) Ion side view

(c) Top view

(d) Bottom view

Figure B1: Photographs of the calorimeter probe taken after the measurements and showing it from four sides

C List of Abbreviations

ALT-II Advanced Limiter Test-II

CFC carbon fibre composite

DMV Disruption Mitigation Valve

DED Dynamic Ergodic Divertor

ECE electron cyclotron emission

ECRH electron cyclotron resonance heating

FWHM full width at half maximum

HWHM half width at half maximum

HFS high field side

ICRH ion cyclotron resonance heating

LCFS last closed flux surface

LFS low field side

MGI massive gas injection

MHD magnetohydrodynamics

NBI neutral beam injection

PFCs plasma facing components

REs runaway electrons

RMP resonant magnetic perturbation

VDE vertical displacement event

References

[1] Department of Economic and Social Affairs Population Division. *World Population in 2300 Highlights.* United Nations, 2003.

[2] N. Nakicenovic, A. Grübler, and A. McDonald. *Global Energy Perspectives.* IIASA and World Energy Council, Cambridge University Press, 1998.

[3] Eine Studie der Deutschen Physikalischen Gesellschaft e.V. *Elektrizität: Schlüssel zu einem nachhaltigen und klimaverträglichen Energiesystem.* Deutsche Physikalische Gesellschaft, 2010.

[4] C. Bond Hatfield. *Nature*, 387:121, 1997.

[5] R.A. Kerr. *Science*, 322:1178–1179, 2008.

[6] F. Joos. *Europhysics News*, 27:213–218, 1996.

[7] D. Maisonnier, P. Sardain, R. Andreani, L. Di Pace, R. Forrest, L. Giancarli, S. Hermsmeyer, P. Norajitra, N. Taylor, and D. Ward. *A Conceptual Study of a Commercial Fusion Power Plant EFDA-RP-RE-5.0.* EFDA European Fusion Development Agreement, 2005.

[8] D.J. Ward, I. Cook, Y. Lechon, and R. Saez. *J. Fusion Engineering and Design*, 75-79:1221–1227, 2005.

[9] F.F. Chen. *Introduction to Plasma Physics and Controlled Fusion Volume 1.* Springer, 1984.

[10] J. Wesson. *Tokamaks.* Oxford Engeneering Science Series 48, Clarendon Press Oxford, 1997.

[11] R.K. Evans. An abundance of lithium. *www.worldlithium.com*, 2008.

[12] R.K. Evans. *Energy*, 3:379–385, 1978.

[13] JET team. *Nucl. Fusion*, 32:187, 1992.

[14] M. Keilhacker, A. Gibson, C. Gormezano, P.J. Lomas, P.R. Thomas, M.L. Watkins, P. Andrew, B. Balet, D. Borba, C.D. Challis, I. Coffey, G.A. Cottrell, H.P.L. De Esch, N. Deliyanakis, A. Fasoli, C.W. Gowers, H.Y. Guo, G.T.A. Huysmans, T.T.C. Jones, W. Kerner, R.W.T. König, M.J. Loughlin, A. Maas, F.B. Marcus, M.F.F. Nave, F.G. Rimini, G.J. Sadler, S.E. Sharapov, G. Sips, P. Smeulders, F.X. Söldner, A. Taroni, B.J.D. Tubbing, M.G. von Hellermann, D.J. Ward, and JET Team. *Nucl. Fusion*, 39:209, 1999.

[15] M. Shimada, D.J. Campbell, V. Mukhovatov, M. Fujiwara, N. Kirneva, K. Lackner, M. Nagami, V.D. Pustovitov, N. Uckan, J. Wesley, N. Asakura, A.E. Costley, A.J.H. Donné, E.J. Doyle, A. Fasoli, C. Gormezano, Y. Gribov, O. Gruber, T.C. Hender, W. Houlberg, S. Ide, Y. Kamada, A. Leonard, B. Lipschultz, A. Loarte, K. Miyamoto, V. Mukhovatov, T.H. Osborne, A. Polevoi, and A.C.C. Sips. *Nucl. Fusion*, 47:S1, 2007.

[16] Plasma Control ITER Physics Expert Group on Disruptions, MHD, and ITER Physics Basis Editors. *Nucl. Fusion*, 39:2251, 1999.

[17] S. Putvinski, P. Barabaschi, N. Fujisawa, N. Putvinskaya, M.N. Rosenbluth, and J. Wesley. *Plasma Phys. Control. Fusion*, 39:B157–B171, 1997.

[18] P. Helander, L.-G. Eriksson, and F. Andersson. *Plasma Phys. Control. Fusion*, 44:B247–B262, 2002.

[19] H.-W. Bartels. *Fusion Eng. Des.*, 23:323–328, 1993.

[20] R. Nygren, T. Lutz, D. Walsh, G. Martin, M. Chatelier, T. Loarer, and D. Guilhem. *J. Nucl. Mater.*, 241-243:522–527, 1997.

[21] T.C. Hender, J.C Wesley, J. Bialek, A. Bondeson, A.H. Boozer, R.J. Buttery, A. Garofalo, T.P Goodman, R.S. Granetz, Y. Gribov, O. Gruber, M. Gryaznevich, G. Giruzzi, S. Günter, N. Hayashi, P. Helander, C.C. Hegna, D.F. Howell, D.A. Humphreys, G.T.A. Huysmans, A.W. Hyatt, A. Isayama, S.C. Jardin, Y. Kawano, A. Kellman, C. Kessel, H.R. Koslowski, R.J. La Haye, E. Lazzaro, Y.Q. Liu, V. Lukash, J. Manickam, S. Medvedev, V. Mertens, S.V. Mirnov, Y. Nakamura, G. Navratil, M. Okabayashi, T. Ozeki, R. Paccagnella, G. Pautasso, F. Porcelli, V.D. Pustovitov, V. Riccardo, M. Sato, O. Sauter, M.J. Schaffer, M. Shimada, P. Sonato, E.J. Strait, M. Sugihara, M. Takechi, A.D. Turnbull, E. Westerhof, D.G. Whyte, R. Yoshino, and H. Zohm and the ITPA MHD, Disruption and Magnetic Control Topical Group. *Nucl. Fusion*, 47:S128, 2007.

[22] R.D. Gill. *Nucl. Fusion*, 33:1613–1625, 1993.

[23] W.M. Stacey. *Fusion Plasma Physics*. WILEY-VCH Verlag GmbH & Co.KGaA, Weinheim, 2005.

[24] H.J. de Blank. Guiding center motion. 10th Carolus Magnus Summer School on Plasma and Fusion Energy Physics, Weert, the Netherlands, 2011.

[25] P. Helander. Classical and neoclassical transport in tokamaks. 10th Carolus Magnus Summer School on Plasma and Fusion Energy Physics, Weert, the Netherlands, 2011.

[26] H.R. Koslowski. Operational limits and limiting instabilities in tokamak machines. 10th Carolus Magnus Summer School on Plasma and Fusion Energy Physics, Weert, the Netherlands, 2011.

[27] W. Bahm, I. Milch, and R.P. Schorn. *Kernfusion.* Helmholtz-Gemeinschaft, 2006.

[28] L.A. Artsimovich. *Nucl. Fusion*, 12:215–252, 1972.

[29] M. Hazewinkel. *Encyclopaedia of Mathematics.* Springer, 2001.

[30] R.J. Buttery, S. Günter, G. Giruzzi, T.C. Hender, D. Howell, G. Huysmans, R.J. La Haye, M. Maraschek, H. Reimerdes, O. Sauter, C.D. Warrick, H.R. Wilson, and H. Zohm. *Plasma Phys. Control. Fusion*, 42 (Suppl. 12B):B61–B73, 2000.

[31] F.C. Schüller. *Plasma Phys. Control. Fusion*, 37:A135–Al62, 1995.

[32] M. Greenwald, J.L. Terry, S.M. Wolfe, S. Ejima, M.G. Bell, S.M. Kaye, and G.H. Neilson. *Nucl. Fusion*, 28:2199–2207, 1988.

[33] F. Troyon, R. Gruber, H. Saurenmann, S. Semenzato, and S. Succi. *Plasma Phys. Control. Fusion*, 26:209–215, 1984.

[34] D.A. Kislov, V.V. Alikaev, Yu.V. Esipchuk, A.M. Kakurtn, A.Ya. Kislov, D.A. Martynov, G.E. Notkin, K.A. Razumova, A.V. Sushkov, and V.V. Volkov. *Nucl. Fusion*, 37:339–350, 1997.

[35] D. Wroblewski, G.L. Jahns, and J.A. Leuer. *Nucl. Fusion*, 37:725–741, 1997.

[36] G. Pautasso, S. Egorov, J.C. Fuchs Ch. Tichmann, A. Herrmann, M. Maraschek, F. Mast, V. Mertens, I. Perchermeier, C.G. Windsor, T. Zehetbauer, and ASDEX Upgrade Team. *J. Nucl. Mater.*, 290 - 293:1045–1051, 2001.

[37] G. Pautasso, C. Tichmann, S. Egorov, T. Zehetbauer, O. Gruber, M. Maraschek, K.-F. Mast, V. Mertens, I. Perchermeierand G. Raupp, W. Treutterer, C.G. Windsor, and ASDEX Upgrade Team. *Nucl. Fusion*, 42:100–108, 2002.

[38] G. Raupp, O. Gruber, A. Kallenbach, V. Mertens, G. Neu, B. Streibl, W. Treutterer, Th. Zehetbauer, D. Zasche, and the ASDEX Upgrade Team. *Fusion Technol.*, 32:444–458, 1997.

[39] A.W. Morris, T.C. Hender, J. Hugill, P.S. Haynes, P.C. Johnson, B. Lloyd, D.C. Robinson, C. Silvester, S. Arshad, and G.M. Fishpool. *Phys. Rev. Lett.*, 64:1254–1257, 1990.

[40] K.H. Finken, G. Mank, A. Krämer-Flecken, and R. Jaspers. *Nucl. Fusion*, 41:1651–1661, 2001.

[41] M. Lehnen, A. Alonso, G. Arnoux, N. Baumgarten, S.A. Bozhenkov, S. Brezinsek, M. Brix, T. Eich, S.N. Gerasimov, A. Huber, S. Jachmich, U. Kruezi, P.D. Morgan, V.V. Plyusnin, C. Reux, V. Riccardo, G. Sergienko, M.F. Stamp, and JET EFDA contributors. *Nucl. Fusion*, 51:123010 (12pp), 2011.

[42] G. Pautasso, D. Coster, T. Eich, J.C. Fuchs, O. Gruber, A. Gude, A. Herrmann, V. Igochine, C. Konz, B. Kurzan, K. Lackner, T. Lunt, M. Maraschеck, A. Mlynek, B. Reiter, V. Rohde, Y. Zhang, X. Bonnin, M. Beck, G. Prausner, and the ASDEX Upgrade Team. *Plasma Phys. Control. Fusion*, 51:124056 (11pp), 2009.

[43] K.H. Finken, R. Jaspers, A. Krämer-Flecken, A. Savtchkov, M. Lehnen, and G. Waidmann. *Fusion Sci. Technol.*, 47:266–273, 2005.

[44] D.G. Whyte, T.C. Jernigan, D.A. Humphreys, A.W. Hyatt, C.J. Lasnier, P.B. Parks, T.E. Evans, M.N. Rosenbluth, P.L. Taylor, A.G. Kellman, D.S. Gray, E.M. Hollmann, and S.K. Combs. *Phys. Rev. Lett.*, 89:055001–1–055001–4, 2002.

[45] E.M. Hollmann, T.C. Jernigan, M. Groth, D.G. Whyte, D.S. Gray, M.E. Austin, B.D. Bray, D.P. Brennan, N.H. Brooks, T.E. Evans, D.A. Humphreys, C.J. Lasnier, R.A. Moyer, A.G. McLean, P.B. Parks, V. Rozhansky, D.L. Rudakov, E.J. Strait, and W.P. West. *Nucl. Fusion*, 45:1046–1055, 2005.

[46] M. Bakhtiari, H. Tamai, Y. Kawano, G.J. Kramer, A. Isayama, T. Nakano, Y. Kamiya, R. Yoshino, Y. Miura, Y. Kusama, and Y. Nishida. *Nucl. Fusion*, 45:318–325, 2005.

[47] R. Granetz, D.G. Whyte, V.A. Izzo, T. Biewer, M.L. Reinke, J. Terry, A. Bader, M. Bakhtiari, T. Jernigan, and G. Wurden. *Nucl. Fusion*, 46:1001–1008, 2006.

[48] R.S. Granetz, E.M. Hollmann, D.G. Whyte, V.A. Izzo, G.Y. Antar, A. Bader, M. Bakhtiari, T. Biewerand J.A. Boedo, T.E. Evans, I.H. Hutchinson, T.C. Jernigan, D.S. Gray, M. Groth, D.A. Humphreys, C.J. Lasnier, R.A. Moyer, P.B. Parks, M.L. Reinke, D.L. Rudakov, E.J. Strait, J.L. Terry, J. Wesley, W.P. West, G. Wurden, and J. Yu. *Nucl. Fusion*, 47:1086–1091, 2007.

[49] E.M. Hollmann, T.C. Jernigan, P.B. Parks, J.A. Boedo, T.E. Evans, M. Groth, D.A. Humphreys, A.N. James, M.J. Lanctot, D. Nishijima, D.L. Rudakov, H.A. Scott, E.J. Strait, M.A. Van Zeeland, J.C. Wesley, W.P. West, W. Wu, and J.H. Yu. *Nucl. Fusion*, 48:115007, 2008.

[50] M. Lehnen, A. Alonso, G. Arnoux, S.A. Bozhenkov, S. Brezinsek, T. Eich, K.H. Finken, A. Huber, S. Jachmich, U. Kruezi, P. D. Morgan, V.V. Plyusnin, C. Reux, V. Riccardo, G. Sergienko, M. F. Stamp, and JET EFDA

contributors. First experiments on massive gas injection at jet - consequences for disruption mitigation in jet and iter. 36th EPS Conference on Plasma Phys. Sofia, June 29 - July 3, 2009 ECA Vol.33E, O-2.001 (2009) http://epsppd.epfl.ch/Sofia/pdf/O2 001.pdf.

[51] R. Yoshino, T. Kondoh, Y. Neyatani, K. Itami, Y. Kawano, and N. Isei. *Plasma Phys. Control. Fusion*, 39:313–332, 1997.

[52] N. Commaux, L.R. Baylor, T.C. Jernigan, E.M. Hollmann, P.B. Parks, D.A. Humphreys, J.C. Wesley, and J.H. Yu. *Nucl. Fusion*, 50:112001 (4pp), 2010.

[53] S.C. Jardin, G.L. Schmidt, E.D. Fredrickson, K.W. Hill, J. Hyun, B.J. Merrill, and R. Sayer. *Nucl. Fusion*, 40:923–933, 2000.

[54] H. Knoepfel and D.A. Spong. *Nucl. Fusion*, 19:785–829, 1979.

[55] V.V. Parail and O.P. Pogutse (ed. M.A. Leontovich). *Runaway Electrons in a Tokamak (in Review of Plasma Physics Vol. 11)*. Consultans Bureau, New York, 1986.

[56] R. Jaspers. *Relativistic Runaway Electrons in Tokamak Plasmas*. CIP-DATA Koninklijke Bibliotheek, Den Haag, ISBN 90-386-0474-2 (PhD thesis, Eindhoven University of Technology, The Netherlands), 1995.

[57] I. Entrop. *Confinement of Relativistic Runaway Electrons in Tokamak Plasmas*. CIP-DATA Library Eindhoven University of Technology, ISBN 90-386-0947-7 (PhD thesis, Eindhoven University of Technology, The Netherlands), 1999.

[58] H.P. Furth and P.H. Rutherford. *Phys. Rev. Lett.*, 28:545–548, 1972.

[59] F. Hoyle. *Some Recent Research in Solar Physics*. Cambridge University Press, Cambridge, 1926.

[60] S. Baidyaroy, M.A. Lampert, B. Zee, and R.U. Martinelli. *J. Appl. Phys.*, 47:2103, 1976.

[61] S. Baidyaroy, M.A. Lampert, B. Zee, and R.U. Martinelli. *J. Appl. Phys.*, 48:1272, 1977.

[62] E.P. Gorbunov, G.G. Dolgov-Savel'ev, V.S. Mukhovatov, V.S. Strelkov, and N.A. Yavlinskii. *Sov. Phys.-Tech. Phys.*, 5:1089, 1961.

[63] V.V. Matveev and A.D. Sokol'ov. *Sov. Phys.-Tech. Phys.*, 5:1084, 1961.

[64] V.V. Matveev, A.D. Sokol'ov, and L.A. Suchkova. *Sov. Phys.-Tech. Phys.*, 8:530, 1963.

[65] G. Fussmann. *Nucl. Fusion*, 19:327, 1979.

[66] H. Dreicer. *Phys. Rev.*, 115:238–249, 1959.

[67] C.T.R. Wilson. *Proc. Roy. Soc.*, 37:32D, 1925.

[68] R.G. Giovanelli. *Philos. Mag.*, 40:206, 1946.

[69] A.V. Gurevich. *Sov. Phys. JETP*, 12:904, 1961.

[70] M.D. Kruskal and I.B. Bernstein. *PPPL Report*, MATT-Q-20:174, 1962.

[71] R.H. Cohen. *Phys. Fluids*, 19:239–244, 1976.

[72] J.W. Connor and R.J. Hastie. *Nucl. Fusion*, 15:415, 1975.

[73] Y.A. Sokolov. *JETP Lett.*, 29:218, 1979.

[74] N.T. Besedin and I.M. Pankratov. *Nucl. Fusion*, 26:807, 1986.

[75] R. Jayakumar, H.H. Fleischmann, and S.J. Zweben. *Phys. Lett. A*, 26172:447, 1993.

[76] M.N. Rosenbluth and S.V. Putvinski. *Nucl. Fusion*, 37:1355, 1997.

[77] S.C. Chiu, M.N. Rosenbluth, R.W. Harvey, and V.S. Chan. *Nucl. Fusion*, 38:1711, 1998.

[78] R. Jaspers, K.H. Finken, G. Mank, F. Hoenen, J.A. Boedo, N.J. Lopes Cardozo, and F.C. Schuller. *Nucl. Fusion*, 33:1775–1785, 1993.

[79] R. Jaspers, N.J. Lopes Cardozo, F.C. Schüller, K.H. Finken, T. Grewe, and G. Mank. *Nucl. Fusion*, 36:367–373, 1996.

[80] H. Smith, P. Helander, L.-G. Eriksson, D. Anderson, M. Lisak, , and F. Andersson. *Phys. Plasmas*, 13:102502 (13pp), 2006.

[81] H. Smith, P. Helander, L.-G. Eriksson, and T. Fülöp. *Phys. Plasmas*, 12:122505 (9pp), 2005.

[82] H.M. Smith, T. Fehér, T. Fülöp, K. Gál, and E. Verwichte. *Plasma Phys. Control. Fusion*, 51:124008 (8pp), 2009.

[83] P. Helander and D.J. Sigmar. *Collisional Transport in Magnetized Plasmas*. Cambridge University Press, Cambridge, 2002.

[84] R.W. Harvey, V.S. Chan, S.C. Chiu, T.E. Evans, M.N. Rosenbluth, and D.G. Whyte. *Phys. Plasmas*, 7:4590, 2000.

[85] P. Helander, H. Smith, T. Fülöp, and L.G. Eriksson. *Phys. Plasmas*, 11:5704, 2004.

[86] H. Smith and E. Verwichte. *Phys. Plasmas*, 15:072502, 2008.

[87] P.L. Taylor, A.G. Kellman, T.E. Evans, D.S. Gray, D.A. Humphreys, A.W. Hyatt, T.C. Jernigan, R.L. Lee, J.A. Leuer, S.C. Luckhardt, P.B. Parks, M.J. Schaffer, D.G. Whyte, and J. Zhang. *Phys. Plasmas*, 6:1872, 1999.

[88] M. de Rover, N.J. Lopes Cardozo, and A. Montvai. *Phys. Plasmas*, 3:4468–4477, 1996.

[89] M. de Rover, N.J. Lopes Cardozo, and A. Montvai. *Phys. Plasmas*, 3:4478–4488, 1996.

[90] A.B. Rechester and M.N. Rosenbluth. *Phys. Rev. Lett*, 40:38–41, 1978.

[91] M. de Rover, A.M. Schilham, A. Montvai, and N.J. Lopes Cardozo. *Phys. Plasmas*, 6:2443, 1999.

[92] J.R. Myra and P.J. Catto. *Phys. Fluids B*, 4:176–186, 1992.

[93] H.E. Mynick and J.D. Strachan. *Phys. Fluids*, 24:695–702, 1981.

[94] C.C. Hegna and J.D. Callen. *Phys. Fluids B*, 5:1804–1808, 1993.

[95] F. Andersson, P. Helander, and L.-G. Eriksson. *Phys. Plasmas*, 8:5221–5229, 2001.

[96] J.R. Martin-Solís, J.D. Alvarez, and R. Sánchez. *Phys. Plasmas*, 5:2370–2377, 1998.

[97] A.J. Russo. *Nucl. Fusion*, 31:117, 1991.

[98] A.J. Russo. *Nucl. Fusion*, 31:117, 1991.

[99] A.G. Elfimov and R.M.O. Galvão. *Plasma Phys. Control. Fusion*, 45:L63–L70, 2003.

[100] T. Fülöp, G. Pokol, P. Helander, and M. Lisak. *Phys. Plasmas*, 13:062506, 2006.

[101] T. Fülöp, G. Pokol, and M. Lisak. *Plasma Phys. Control. Fusion*, 50:045003 (13pp), 2008.

[102] V.V. Parail and O.P. Pogutse. *Nucl. Fusion*, 18:303, 1978.

[103] Equipe TFR. *Nucl. Fusion*, 18:647–731, 1978.

[104] B. Esposito, J.R. Martín-Solís, F.M. Poli, J.A. Mier, R. Sánchez, and L. Panaccione. *Phys. Plasmas*, 10:2350/11, 2003.

[105] P.V. Savrukhin. *Phys. Rev. Lett.*, 86:3036(4), 2001.

[106] B. Esposito, R.M. Solis, P. van Belle, O.N. Jarvis, F.B. Marcus, G. Sadler, R. Sanchez, B. Fischer, P. Froissard, J.M. Adams, E. Cecil, and N. Watkins. *Plas. Phys. Contr. Fusion*, 38:2035–2049, 1996.

[107] M.A. Leontovich. *Plasma Physics and the Problem of Controlled Thermonuclear Reactions, V.S. Strelkov: Study of radiation from an electrodeless discharge in deuterium.* Pergamon Press, New York, 1960.

[108] K.H. Finken, S.S. Abdullaev, M.W. Jakubowski, R. Jaspers, M. Lehnen, R. Schlickeiser, K.H. Spatschek, A. Wingen, R. Wolf, and the TEXTOR team. *Nucl. Fusion*, 47:91–102, 2007.

[109] K.H. Finken, B. Unterberg, Y. Xu, S.S. Abdullaev, M. Jakubowski, M. Lehnen, M.F.M. de Bock, S. Bozhenkov, S. Brezinsek, C. Busch, I.G.J. Classen, J.W. Coenen, D. Harting, M. von Hellermann, S. Jachmich, R.J.E. Jaspers, Y. Kikuchi, A. Krämer-Flecken, Y. Liang, M. Mitri, P. Peleman, A. Pospieszczyk, D. Reiser, D. Reiter, U. Samm, D. Schega, O. Schmitz, S. Soldatov, M. Van Schoor, M. Vergote, R.R. Weynants, R. Wolf, O. Zimmermann, and the TEXTOR Team. *Nucl. Fusion*, 47:522–534, 2007.

[110] R. Jaspers, N.J. Lopes Cardozo, A.J.H. Donnè, H.L.M. Widdershoven, and K.H. Finken. *Rev. Scient. Instrum.*, 72:466, 2001.

[111] K.H. Finken, J.G. Watkins, D. Rusbüldt, W.J. Corbett, K.H. Dippel, D.M. Goebel, and R.A. Moyer. *Nucl. Fusion*, 30:859–870, 1990.

[112] T. Kawamura, H. Obayashi, and A. Miyahara. *Fusion Eng. Des.*, 9:45–48, 1989.

[113] D. Harder, R. Mehling, and A.C. England. *Phys. Lett. B*, 32:610–612, 1970.

[114] S. Putvinski, N. Fujisawa, D. Post, N. Putvinskaya, M.N. Rosenbluth, and J. Wesley. *J.of Nucl. Mater.*, 241-243:316 – 321, 1997.

[115] M. Lehnen, S.A. Bozhenkov, S.S. Abdullaev, and M.W. Jakubowski (TEXTOR Team). *Phys. Rev Lett.*, 100:255003, 2008.

[116] S.A. Bozhenkov, M. Lehnen, K.H. Finken, M.W. Jakubowski, R.C. Wolf, R. Jaspers, M. Kantor, O.V. Marchuk, E. Uzgel, G. VanWassenhove, O. Zimmermann, D. Reiter, and the TEXTOR team. *Plasma Phys. Control. Fusion*, 50:105007 (18pp), 2008.

[117] S.A. Bozhenkov, M. Lehnen, K.H. Finken, G. Bertschinger, H.R. Koslowski, D. Reiter, R.C. Wolf, and TEXTOR team. *Nucl. Fusion*, 51:083033 (10pp), 2011.

[118] K.H. Finken, A. Kraemer-Flecken, M. Lehnen, and A. Savtchkov. *J. Nucl. Mater.*, 313-316:1247, 2003.

[119] M.N. Rosenbluth, S.V. Putvinskij, and P.B. Parks. *Nucl. Fusion*, 37:955–966, 1997.

[120] N. Commaux, L.R. Baylor, S.K. Combs, N.W. Eidietis, T.E. Evans, C.R. Foust, E.M. Hollmann, D.A. Humphreys, V.A. Izzo, A.N. James, T.C. Jernigan, S.J. Meitner, P.B. Parks, J.C. Wesley, and J.H. Yu. *Nucl. Fusion*, 51:103001 (9pp), 2011.

[121] F. Saint-Laurent, J. Bucalossi, C. Reux, S. Bremond, D. Douai, C. Gil, and P. Moreau. Control of runaway electron beam heat loads on tore supra. 38th EPS Conference on Plasma Physics, Strasbourg, France, 2011.

[122] G. Papp, M. Drevlak, T. Fülöp, and P. Helander. *Nucl. Fusion*, 51:043004 (11pp), 2011.

[123] A. Wingen, S.S. Abdullaev, K.H. Finken, M. Jakubowski, and K.H. Spatschek. *Nucl. Fusion*, 46:941–952, 2006.

[124] R. Yoshino and S. Tokuda. *Nucl. Fusion*, 40:1293–1309, 2000.

[125] E.M. Hollmann, P.B. Parks, D.A. Humphreys, N.H. Brooks, N. Commaux, N. Eidietis, T.E. Evans, R. Isler, A.N. James, T.C. Jernigan, J. Munoz, E.J. Strait, C. Tsui, J. Wesley, and J.H. Yu. *Nucl. Fusion*, 51:103026 (8pp), 2011.

[126] O. Neubauer, G. Czymek, B. Giesen, P.W. Hüttemann, M. Sauer, W. Schalt, and J. Schruff. *Fusion Sci. Technol.*, 47:76–86, 2005.

[127] S.A. Bozhenkov, K.H. Finken, M. Lehnen, and R.C. Wolf. *Rev. Sci. Instrum.*, 78:033503, 2007.

[128] K.H. Finken, S.S. Abdullaev, M. Jakubowski, M. Lehnen, A. Nicolai, and K.H. Spatschek. *The structure of magnetic field in the TEXTOR-DED*, volume 45 of *Energy Technology*. Forschungszentrum Jülich, Jülich, Germany, 2005.

[129] S. Agostinelli, J. Allison, K. Amako, J. Apostolakis, H. Araujo, P. Arce, M. Asai, D. Axen, S. Banerjee, G. Barrand, F. Behner, L. Bellagamba, J. Boudreau, L. Broglia, A. Brunengo, H. Burkhardt, S. Chauvie, J. Chuma, R. Chytracek, G. Cooperman, G. Cosmo, P. Degtyarenko, A. Dell'Acqua, G. Depaola, D. Dietrich, R. Enami, A. Feliciello, C. Ferguson, H. Fesefeldt, G. Folger, F. Foppiano, A. Forti, S. Garelli, S. Giani, R. Giannitrapani, D. Gibin, J.J. Gómez Cadenas, I. González, G. Gracia Abril, G. Greeniaus, W. Greiner, V. Grichine, A. Grossheim, S. Guatelli, P. Gumplinger, R. Hamatsu, K. Hashimoto, H. Hasui, A. Heikkinen, A. Howard, V. Ivanchenko, A. Johnson, F.W. Jones, J. Kallenbach, N. Kanaya, M. Kawabata, Y. Kawabata, M. Kawaguti, S. Kelner, P. Kent, A. Kimura, T. Kodama, R. Kokoulin, M. Kossov, H. Kurashige, E. Lamanna, T. Lampén, V. Lara, V. Lefebure, F. Lei, M. Liendl, W. Lockman, F. Longo, S. Magni, M. Maire, E. Medernach, K. Minamimoto, P. Mora de Freitas, Y. Morita, K. Murakami, M. Nagamatu, R. Nartallo, P. Nieminen, T. Nishimura, K. Ohtsubo, M. Okamura, S. O'Neale,

Y. Oohata, K. Paech, J. Perl, A. Pfeiffer, M.G. Pia, F. Ranjard, A. Rybin, S. Sadilov, E. Di Salvo, G. Santin, T. Sasaki, N. Savvas, Y. Sawada, S. Scherer, S. Sei, V. Sirotenko, D. Smith, N. Starkov, H. Stoecker, J. Sulkimo, M. Takahata, S. Tanaka, E. Tcherniaev, E. Safai Tehrani, M. Tropeano, P. Truscott, H. Uno, L. Urban, P. Urban, M. Verderi, A. Walkden, W. Wander, H. Weber, J.P. Wellisch, T. Wenaus, D.C. Williams, D. Wright, T. Yamada, H. Yoshida, and D. Zschiesche. *Nucl. Instrum. Meth. A*, 506:250–303, 2003.

[130] J. Allison, K. Amako, J. Apostolakis, H. Araujo, P. Arce Dubois, M. Asai, G. Barrand, R. Capra, S. Chauvie, R. Chytracek, G.A.P. Cirrone, G. Cooperman, G. Cosmo, G. Cuttone, G. G. Daquino, M. Donszelmann, M. Dressel, G. Folger, F. Foppiano, J. Generowicz, V. Grichine, S. Guatelli, P. Gumplinger, A. Heikkinen, I. Hrivnacova, A. Howard, S. Incerti, V. Ivanchenko, T. Johnson, F. Jones, T. Koi, R. Kokoulin, M. Kossov, H. Kurashige, V. Lara, S. Larsson, F. Lei, O. Link, F. Longo, M. Maire, A. Mantero, B. Mascialino, I. McLaren, P. Mendez Lorenzo, K. Minamimoto, K. Murakami, P. Nieminen, L. Pandola, S. Parlati, L. Peralta, J. Perl, A. Pfeiffer, M.G. Pia, A. Ribon, P. Rodrigues, G. Russo, S. Sadilov, G. Santin, T. Sasaki, D. Smith, N. Starkov, S. Tanaka, E. Tcherniaev, B. Tomé, A. Trindade, P. Truscott, L. Urban, M. Verderi, A. Walkden, J.P. Wellisch, D.C. Williams, D. Wright, , and H. Yoshida. *IEEE Trans. Nucl. Sci.*, 53:270–278, 2006.

[131] T. Kudyakov. *Spectral measurements of runaway electrons in the TEXTOR tokamak.* (PhD thesis, Heinrich-Heine-Universität Düsseldorf, Germany), 2009.

[132] M. Forster, K.H. Finken, M. Lehnen, J. Linke, B. Schweer, C. Thomser, O. Willi, Y. Xu, and the TEXTOR team. *Nucl. Fusion*, 51:043003 (8pp), 2011.

[133] M. Forster, K.H. Finken, M. Lehnen, O. Willi, Y. Xu, and the TEXTOR team. Measurements of the Runaway Electron Energy during Disruptions in the Tokamak TEXTOR. *Phys. Plasmas*, 19:052506, 2012.

[134] A. Savtchkov andK. H. Finken and G. Mank. *Rev. Sci. Instrum.*, 73:3490–3493, 2002.

[135] K.H. Finken, M. Lehnen, and S.A. Bozhenkov. *Nucl. Fusion*, 48:115001 (10pp), 2008.

[136] K.H. Finken, M. Lehnen, and S.A. Bozhenkov. *Nucl. Fusion*, 51:033007 (12pp), 2011.

[137] K.H. Finken, S.S. Abdullaev, A. Kaleck, and G.H. Wolf. *Nucl. Fusion*, 39:637–662, 1999.

[138] K.H. Finken, T. Eich, and A. Kaleck. *Nucl. Fusion*, 38:515–529, 1998.

[139] S.S. Abdullaev, K.H. Finken, M.W. Jakubowski, S.V. Kasilov, M. Kobayashi, D. Reiser, D. Reiter, A.M. Runov, and R. Wolf. *Nucl. Fusion*, 43:299–313, 2003.

[140] M.W. Jakubowski, S.S. Abdullaev, K.H. Finken, and the TEXTOR Team. *Nucl. Fusion*, 44:S1–S11, 2004.

[141] V.P. Zhukov and K.H. Finken. *Nucl. Fusion*, 44:S44–S54, 2004.

[142] R.C.Wolf, W. Biel, M.F.M. de Bock, K.H. Finken amd S. Günter, G.M.D. Hogeweij, S. Jachmich, M.W. Jakubowski, R.J.E. Jaspers, A. Krämer-Flecken, H.R. Koslowski, M. Lehnen, Y. Liang, B. Unterberg, S.K. Varshney, M. von Hellermann, Q. Yu, O. Zimmermann, S.S. Abdullaev, A.J.H. Donné, U. Samm, B. Schweer, M. Tokar, E. Westerhof, and the TEXTOR Team. *Nucl. Fusion*, 45:1700–1707, 2005.

[143] K.H. Finken amd S.S. Abdullaev, T. Eich, D.W. Faulconer, M. Kobayashi, R. Koch, G. Mank, and A. Rogister. *Nucl. Fusion*, 41:503–511, 2001.

[144] GEANT4 website. *http://www.geant4.org/geant4/*.

[145] T. Kudyakov, K.H. Finken, M.W. Jakubowski, M. Lehnen, Y. Xu, B. Schweer, T. Toncian, G. van Wassenhove, O. Willi, and the TEXTOR team. *Nucl. Fusion*, 48:122002, 2008.

[146] T. Kudyakov, K. H. Finken, M. Jakubowski, M. Lehnen, Y. Xu, and O. Willi. *Rev. Sci. Instrum.*, 79:10F126, 2008.

[147] T. Kudyakov, A. Jochmann, K. Zeil, S. Kraft, K. H. Finken, U. Schramm, and O. Willi. *Rev. Sci. Instrum.*, 80:076106, 2009.

[148] M.J. Berger, J.S. Coursey, M.A. Zucker, and J. Chang. Estar database. *http://www.nist.gov/pml/data/star/index.cfm*, online 1998.

[149] M. Forster, K.H. Finken, T. Kudyakov, M. Lehnen, O. Willi, Y.Xu, L. Zeng, and the TEXTOR team. Temporal and Spectral Evolution of Runaway Electron Bursts in TEXTOR Disruptions. *Phys. Plasmas*, 19:092513, 2012.

[150] T. Kawamura, H. Obayashi, and A. Miyahara. *Fusion Eng. Des.*, 9:45–48, 1989.

[151] R. Jayakumar, H.H. Fleischmann, and S.J. Zweben. *Physics Letters A*, 172:447–451, 1993.

[152] R. Jaspers, N.J. Lopes Cardozo, K.H. Finken, B.C. Schokker, G. Mank, G. Fuchs, and F.C. Schüller. *Phys. Rev. Lett.*, 72:4093–4097, 1993.

[153] V.V. Plyusnin, V. Riccardo, R. Jaspers, B. Alper, V.G. Kiptily, J. Mlynar, S. Popovichev, E. de La Luna, F. Andersson, and JET EFDA contributors. *Nucl. Fusion*, 46:277–284, 2006.

[154] A. Loarte, V. Riccardo, J.R. Martin-Solis, J. Paley, A. Huber, M. Lehnen, and JET EFDA Contributors. *Nucl. Fusion*, 51:073004 (20pp), 2011.

[155] M. Forster, S.S. Abdullaev, K.H. Finken, T. Kudyakov, M. Lehnen, G. Sewell, O. Willi, Y. Xu, and the TEXTOR team. Runaway Electron Transport in Turbulent and Resonantly Perturbed Magnetic Topologies of TEXTOR. *Nucl. Fusion*, 52:083016 (13pp), 2012.

[156] V. Riccardo, G. Arnoux, P. Cahyna, T.C. Hender, A. Huber, S. Jachmich, V. Kiptily, R. Koslowski, L. Krlin, M. Lehnen, A. Loarte, E. Nardon, R. Paprok, D. Tskhakaya (Sr), and JET-EFDA contributors. *Plasma Phys. Control. Fusion*, 52:124018 (12pp), 2010.

[157] R.D. Gill, B. Alper, M. de Baar, T.C. Hender, M.F. Johnson, V. Riccardo, and contributors to the EFDA-JET Workprogramme. *Nucl. Fusion*, 42:1039–1044, 2002.

[158] M. Lehnen, S.S. Abdullaev, G. Arnoux, S.A. Bozhenkov, M.W. Jakubowski, R. Jaspers, V.V. Plyusnin, V. Riccardo, U. Samm, JET EFDA Contributors, and The TEXTOR Team. *J. Nucl. Mater.*, 390-391:740–746, 2009.

[159] T. Fülöp, H.M. Smith, and G. Pokol. *Phys. Plasmas*, 16:022502, 2009.

[160] I. Entrop, N.J. Lopes Cardozo, R. Jaspers, and K.H. Finken. *Phys. Rev. Lett.*, 84:3606–3609, 2000.

[161] J.R. Myra, P.J. Catto, A.J. Wootton, R.D. Bengston, and P.W. Wang. *Phys. Fluids B*, 4:2092, 1992.

[162] J.R. Myra, P.J. Catto, H.E. Mynick, and R.E. Duvall. *Phys. Fluids B*, 5:1160, 1993.

[163] J.R. Martín-Solís, R. Sánchez, and B. Esposito. *Phys. Plasmas*, 6:3925, 1999.

[164] T. Hauff and F. Jenko. *Phys. Plasmas*, 16:102308, 2009.

[165] S.S. Abdullaev, K.H. Finken, T. Kudyakov, and M. Lehnen. *Contrib. Plasma Phys.*, 50(10):929–941, 2010.

[166] S.S. Abdullaev, A. Wingen, and K.H. Spatschek. *Phys. Plasmas*, 13(4):042509, 2006.

[167] I. Entrop, R. Jaspers, N.J. Lopes Cardozo, and K.H. Finken. *Phys. Plasmas*, 1999.

[168] T. Kudyakov, S.S. Abdullaev, S.A. Bozhenkov, K.H. Finken, M.W. Jakubowski, M. Lehnen, G. Sewell, O. Willi, Y. Xu, and the TEXTOR team. *Nucl. Fusion*, 52:023025, 2012.

[169] M.W. Jakubowski, O. Schmitz, S.S. Abdullaev, S. Brezinsek, K.H. Finken, A. Krämer-Flecken, M. Lehnen, U. Samm, K.H. Spatschek, B. Unterberg, R.C. Wolf, and the TEXTOR team. *Phys. Rev. Lett.*, 96:035004, 2006.

[170] G. Sewell. *Adv. Engng. Softw.*, 41:748–753, 2010.

Acknowledgement

I thank Prof. Dr. Oswald Willi and Prof. Dr. Ulrich Samm for offering me the possibility to work in the exciting field of fusion research and for giving me all the support which was necessary to make this work successful. Additional gratitude goes to Prof. Dr. Willi for being a dedicated and promoting supervisor.

Furthermore, I would like to thank Prof. Dr. Thomas Klinger for writing the external report.

I greatly acknowledge the support of Dr. Michael Lehnen, Dr. Yuhong Xu and the TEXTOR team who did essential work which helped to make the experiments successful.

Dr. Sadrilla Abdullaev and Prof. Dr. Granville Sewell rendered help regarding the theoretical part of the work and provided essential simulations. I thank them both very much.

Fruitful discussions and the help of experts are mandatory for good scientific work. I send many thanks to Dr. Jochen Linke, Dr. Corinna Thomser, Dr. Egbert Vessel, Volker Gutzeit, Dr. L. Zeng and the Institut für organische und makromolekulare Chemie of the Heinrich-Heine-Universität Düsseldorf.

I thank Stefan Manderla and especially Albert Hiller a lot for their competent and motivated technical support.

I am thankful to everyone at the Institut für Laser- und Plasmaphysik and at the Forschunsgzentrum Jülich who provided help and made the time of my PhD work pleasant.

A very special word of thanks goes to Dr. Karl Heinz Finken for being a dedicated, ambitious, fair and taking mentor.

This work was supported by the Graduiertenkolleg 1203 "Dynamics of hot plasmas - Dynamik heißer Plasmen" of the DFG, an F&E contract between the Heinrich-Heine-Universität Düsseldorf and the Forschungszentrum Jülich GmbH and by the Trilateral Euregio Cluster (TEC) of EURATOM Associations.

Declaration of Academic Honesty (Eidesstattliche Versicherung)

Ich versichere an Eides Statt, dass die Dissertation von mir selbständig und ohne unzulässige fremde Hilfe unter Beachtung der "Grundsätze zur Sicherung guter wissenschaftlicher Praxis an der Heinrich-Heine-Universität Düsseldorf" erstellt worden ist.

Die Dissertation wurde in der vorgelegten oder in ähnlicher Form noch bei keiner anderen Institution eingereicht. Ich habe bisher keine erfolglosen Promotionsversuche unternommen.

Düsseldorf,

Michael Forster